2009

Characterization of conductive polycarbonate films

Selma Hokenek
University of South Florida

Characterization of Conductive Polycarbonate Films

by

Selma Hokenek

A thesis submitted in partial fulfillment
of the requirements for the degree of
Master of Science in Biomedical Engineering
Department of Chemical and Biomedical Engineering
College of Engineering
University of South Florida

Major Professor: Norma A. Alcantar, Ph.D.
Julianne P. Harmon, Ph.D.
John Wolan, Ph.D.

Date of Approval:
March 30, 2009

Keywords: thin films, organic dye, transparent, BEDO-TTF dye, iodine doping

Dedication

I would like to dedicate this work to my wonderful supporting family, who have helped me through all the stressful moments, to my wonderful co-workers, who helped me out when I hit a roadblock, and to those students who take up the thread of this research after me, may their roads be smooth.

Acknowledgments

I would like to thank Dr. Alcantar for giving me this opportunity, Parul Jain and Dr. Harmon, our co-workers in Chemistry, for their tireless efforts and help in so many different aspects of this project, and the National Science Foundation CBET grant 0808053 for supporting this research. I would also like to acknowledge Dr. Saddow and his research group for being so endlessly patient in letting me borrow their lab equipment at random intervals. Last, but certainly not least, I would like to thank all of the other members of my own research group for everything they have done to help me get through the process of putting together this document.

Table of Contents

List of Figures

Characterization of Conductive Polycarbonate Films

Selma Hokenek

ABSTRACT

Transparency and conductivity are highly desirable qualities in materials for modern gas sensors. Polymer gas sensors have been developed in which the polymer acts as a solid electrolyte. However, these types of sensors are opaque, which limits their potential for integration with dichromatic materials. The development of a sensor integrating conductive polymer films and dichromatic materials requires the implementation of a transparent conductive polymer film. The potential of iodine-doped bisphenol-a polycarbonate films containing bis(ethylenedioxy)-tetrathiafulvalene (BEDO-TTF) dye for sensor applications will be tested through characterization of the films at various stages of their fabrication using Atomic Force Microscopy (AFM), Transmission Electron Microscopy (TEM), transmission Fourier Transform Infrared Spectroscopy (FTIR), Optical Microscopy (OM), and Four Point Probe conductivity measurements (FPP). FTIR results show that there is an interaction between the polycarbonate matrix and the dye-iodine complex. Measured resistivities of the iodine doped films range from 148 Ω-cm to 2.82 kΩ-cm depending on the concentration of the iodine and exposure time. The imaging techniques used show a significant difference in the structure and the surface of the iodine doped-PC-BEDO-TTF films with respect to the bare polycarbonate films or the films mixed with the organic dye. It is also clear that the

surface roughness of the prepared conductive films increases with iodine loading. These films have the potential to be used in sensor or photovoltaic applications.

Chapter One: Introduction

The aim in the development of sensors is to design a device which will minimize or even eliminate the time lapse between sample preparation and measurement that is inherent in traditional laboratory methods, and be of a configuration that is ready for field studies. This miniaturization is necessary in order to provide an easily portable device. Additional improvements are needed to ensure continuous quantitative or qualitative analysis, while maintaining the precision and accuracy of traditional laboratory methods.

In the past, a variety of approaches have been used in the attempt to develop a good solution to this problem. One of the big successes has been in the development of microchips and integrated processors. The advantage of having microchips and integrated processors is their ability to conduct current. Conductivity is a quality that is highly desirable in modern sensors. The application of polymer materials has also been proposed for a number of different applications in the field of sensors. Polymer sensors have been developed to measure a vast number of different reactions and even cell types, ranging from the quantification of CD4+ lymphocytes [1], to piezoelectric sensors [2], and the sensing of nitrites [3].

There are also a number of different applications of polymers in the field of gas sensing, such as vapor-detection of organic compounds [4]. Many of these polymer gas sensors generally rely on the conductive properties of the polymer itself, as a solid electrolyte [5]. There are no known organic superconductors, but a number of organic superconducting charge-transfer complexes are known [6].

Certain organic compounds, such as polymers, can be transformed to be conducting if they are exposed to iodine vapors. These include polyacetylene [7], whose improved electrical properties were discovered in the late 1970s, and nanocomposites such as bisphenol-a polycarbonate and bis(ethylenedioxy)-tetrathiafulvalene (BEDO-TTF) which were developed later [8]. The increase in the conductivity of polyacetylene was marked, as shown by Shirakawa *et al* in 1997, and Chiang *et al* in 1978. The conductivity of the polyacetylene rose by a factor of about 11 orders of magnitude [9, 10]. At a doping of roughly 2%, using the iodine vapor treatment, the charge carriers are free to move along the polymer chains resulting in metallic behavior. Subsequently, in 1989, Suzuki et al. succeeded in making bis(ethylenedioxy)-tetrathiafulvalene (BEDO-TTF) [11]. A schematic of the structure of the dye used in this project to induce electron movement is shown in Figure 1. This compound, mixed with polymer, has been shown to increase electron mobility after being doped with iodine because the dye/iodine combination acts as a charge carrier, resulting in metallic behavior [8].

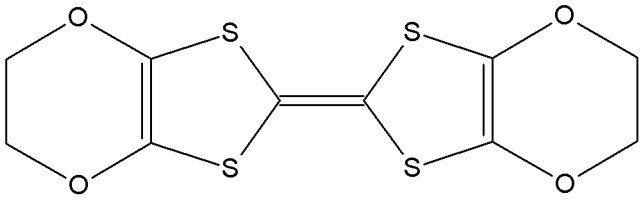

Figure 1: Structure of Bis(ethylenedioxy)-tetrathiafulvalene (BEDO-TTF).

Tetrathiafulvalene and related molecules, such as the BEDO-TTF shown in Figure 1, can function as electron donors since they have short S-S contacts between molecules within their volume which provide the added dimensionality that must exist for superconducting coherence [6]. Work has been presented by Elsenbaumer et al. [6] that

describes in detail the conceptual design and methods of making conductive polymer films out of tetrathiafulvalene derivatives.

The strong tendency of BEDO-TTF toward self-aggregation leads to the low energetic cost of the formation of two-dimensional organic layers [12]. This, together with a low adiabatic ionization potential of 6.12 eV [13], is what allows BEDO-TTF to form conductive complexes with a wide variety of organic acceptors and various anions [14].

Others use the approach of embedding conductive nanomaterials within an insulating polymer matrix[15-17]. The polymer matrix is used to stabilize the particles in the form of a nanocomposite, which in turn is used for the fabrication of devices [18, 19].

The research that will be presented in Chapters Five and Six focuses on the characterization of thin polycarbonate films that have been exposed to different concentrations of BEDO-TTF and iodine vapors. The long term goal of the project is the eventual development of a polycarbonate transparent and conductive thin film sensor for the detection of explosives, specifically nitroamines and peroxides, as will be shown in Figure 3. The baseline conductivity after the addition of the BEDO-TTF dye, iodine, and gold nanoparticles is expected to reach levels high enough to enable the easy use of a voltimetric or amperometric approach to create a sensor which will warn of any vapors that it comes into contact with, using, for example, a dichromatic substrate which will change color based on the voltage or current across the film. This would have a wide variety of applications in areas such as defense against chemical attacks or attacks that rely on improvised explosive devices (IEDs).

The polycarbonate film itself is not expected to have a very good electrical conductivity, due to the nature of the polymer itself. Instead, polycarbonate has a reasonable resistance to changes in temperature, good dimensional stability, and low creep. However, it has only a limited chemical resistance and tends to undergo environmental stress cracking [20]. Polycarbonate has the additional advantages of being transparent, allowing it to be used in conjunction with dichromatic materials, and being very easily available. The low cost and wide availability are very desirable from a manufacturing standpoint, since they dramatically lower the cost of production. The structure of the polycarbonate used in this study is shown in Figure 2.

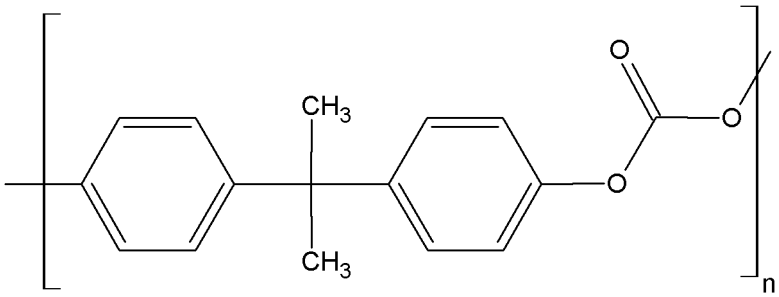

Figure 2: Structure of Bisphenol-a Polycarbonate.

Once the dye has been added to the polycarbonate film and doping with iodine has taken place, a transformation which renders the film conductive is expected to take place due to the formation of a complex between the iodine and the dye. Gold nanoparticles will be added to improve the conductivity of the films, but their preparation and characterization is out of the scope of this thesis.

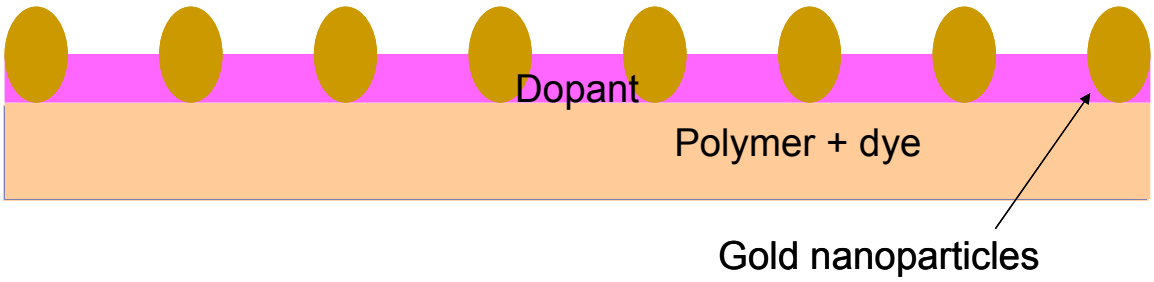

Figure 3: Schematic of the Structure Planned for the Explosives Sensor Proposed. The sensor consists of three main components: the polymer matrix containing the dye, the dopant, and the gold nanoparticles that will allow for the creation of surface active sites in future.

Chapter Two: Overview of Sensors

Generally speaking, the aim in developing sensors is to minimize or eliminate the time lapse between sampling and analysis where possible, thus providing continuous quantitative or qualitative analysis, while also maintaining the precision and accuracy of traditional laboratory methods of analysis [21]. Transparent polymers such as polycarbonate and gold nanoparticles have been used in a variety of sensors in the past, including biosensors, as can be seen by the number of papers published that relate to the use of polycarbonate or gold for biosensors; for instance, nanoparticles and other nano-scale materials have been tested for applications in biosensors for analytical chemistry [22], biomolecular interaction analysis [23], and the fabrication of enzyme-based biosensors [24-26], among others.

Some of the most important applications for sensors include how to detect explosives. For example, a sensor was developed by Doroshkin *et al* using cymantrene in a polystyrene matrix for the detection of explosives on surfaces [27]. The use of cymantrene is attractive in this application because it turns a brilliant blue after coming into contact with the explosives and being exposed to UV light for a short time [28]. Similarly, sensors based on gold nanoparticles have been devised and their effectiveness has been probed by several groups [22, 29-33]. However, they generally tend to be very expensive or difficult to interpret. Zeolites [34] and metallocene-doped conjugated polymers [27, 28, 35, 36] have also been used in similar applications.

2.1. Polycarbonate Sensors and Metal Particles

Polycarbonate has been used for a number of applications in the development of sensors. For example, as reported by Nanto et al., polycarbonate was incorporated into a device used to monitor for the presence of harmful gases [37]. Conductive polycarbonate composites have also been fabricated for the detection of dichloromethane (DCM) and toluene [38]. This type of sensing is based on diffusion forces; the composite contains conducting pathways within its volume whose connections are broken when the solvent molecules that the composite is sensitive to diffuse through the composite [38].

It is expected that polycarbonate films containing a nearly even distribution of BEDO-TTF throughout its volume will form conducting pathways when doped with iodine. Most of these pathways will be near the surface of the film, due to the tendency of the iodine to deposit on the film surface and form crystals. Polycarbonate has also been used as a matrix for the development of a process to precipitate nanoparticles *in situ* [39]. This precipitation process could potentially have applications in the refinement of the fabrication of our films, as regards the incorporation of the gold nanoparticles. Additionally, De and Kundu [29] have reported on a gold nanocluster doped organic-inorganic hybrid coating that was applied to polycarbonate substrates, where it acted as an abrasion resistant protective layer. This suggests that perhaps our films can be made abrasion resistant, as well, in turn making them more stable and robust as sensors.

Chapter Three: General Characterization Techniques

3.1. Fourier Transform Infrared Spectroscopy (FTIR)

In principle, Fourier Transform Infrared Spectroscopy is a reliable and relatively simple analytical technique. A beam of light with a known frequency in the infrared range is passed through a sample, and the amount of light absorbed by the sample is measured by comparing the beam passing through the sample with a reference beam. This is repeated for wavelengths in the IR region. Another measurement commonly used in FTIR spectroscopy is called the wavenumber. It is easier to refer to the wavenumber at which a peak appears because wavenumbers correlate to energy directly. This is not the case when using wavelengths, which have a more complicated relationship with the energy they correlate to [40]. Wavenumbers are related to wavelength by the relationship:

$$wavenumber(cm^{-1}) = \frac{10000}{wavelength(\mu m)} \qquad \text{eq. 1}$$

FTIR spectroscopy works by exploiting the very nature of the interatomic bond. All pairs of covalently bonded atoms have a characteristic frequency at which they will vibrate or rotate. These characteristic frequencies are determined by the discrete energy levels, or vibrational modes, at which a given covalent bond can resonate. This is determined by a number of factors, including the masses of the atoms, and the presence of a dipole moment. A molecule is IR active if there is a permanent dipole moment,

which is free to resonate when energy is added in the form of IR light [40]. As a result, the characteristic frequencies of the vibrations can be associated with a particular bond type.

In the case of a simple diatomic molecule, there is only a single bond, which may stretch when energy is added, for example, in the form of infrared light. In more complex molecules, there are many bonds, and vibrations can be conjugated. This leads to the absorption of infrared light at characteristic frequencies that correspond to chemical groups. For example, the atoms that comprise a CH_2 group have six different, distinct, modes of vibration: symmetrical and asymmetrical stretching, twisting, rocking, scissoring, and wagging.

According to the convention that has grown around the use of spectroscopy, the wavelengths used in infrared spectroscopy have been classified into three broad categories: far-, mid-, and near-infrared. In far-infrared (FIR) spectroscopy, the wavenumbers examined range from 400 to 10 cm^{-1}. FIR spectroscopy is useful mainly for the examination of the quantum vibrational states of gases [41]. In the mid-infrared range lie wavenumbers of 4000 to 400 cm^{-1}, and in the near-infrared (NIR) 14000 to 4000 cm^{-1}. Those wavelengths in the mid-infrared are usually used to study fundamental intramolecular vibrations, and the near-infrared can be used to excite overtone or harmonic vibrations in molecules.

When a beam of IR light is generated, it is split into two separate beams using a half-silvered mirror. One of them is passed through the sample, and the other through a reference. When working with liquid samples, the reference used is usually the substance's solvent. Then, both beams are directed back towards a splitter, which is used

to quickly alternate which of the two beams reaches the detector. The two signals are compared, and a plot of the absorbance is generated.

The IR spectrum of a sample is collected by shining a monochromatic beam at the sample which changes wavelength over time, or by using a Fourier transform instrument which allows you to measure all wavelengths at once. Once this has been completed, the information is generally sent to a computer to be decoded using a program devoted to the task. After the transmittance at each wavelength has been calculated by the program, the spectrum of the sample is then displayed. The analysis of this signal yields much information about the molecular structure of the specimen of interest. Samples with only a few IR active bonds and high levels of purity will generate simple spectra. The more complex the molecular structure, the more peaks in the spectrum, and in some instances, the peaks need to be deconvoluted to extract all the information present in the spectrum.

The use of the reference prevents fluctuations in the output of the source from affecting the data, and allows the signal of the solvent to be subtracted from the signal of the sample being analyzed, leaving only the signal of the sample we wish to see.

3.1.1. Attenuated Total Reflection Fourier Transform Infrared Spectroscopy (ATR-FTIR)

Attenuated Total Reflection (ATR), is a spectroscopic technique that has the sensitivity to detect very low concentrations of sample near the crystal. In this study, ATR-FTIR is used to study the spectra of fabricated films.

The way measurements are performed is fairly simple: a beam of IR light is passed through an ATR crystal, which is usually made from zinc selenide (ZnSe) or

germanium. This crystal has the property of being transparent to the IR beam and has a relatively high refractive index. The IR beam is aimed in such a way that it is internally reflected within the crystal at least once. This reflection should take place where the crystal is in contact with the sample of interest for the best results. If this does not occur, the spectroscopic signal of the sample will not be well defined or clean. In the setup used for this study, the beam was bounced about twelve times. This dramatically increases the likelihood that the sample will be in near the crystal in at least one of the places where the beam bounces. The beam reflected by the sample is then collected by a detector once it has exited the crystal. The reflection of the light beam off the internal surface of the crystal forms what is known as an evanescent wave, which penetrates into the sample to a depth of a few micrometers. This phenomenon is used in ATR-FTIR to examine the structure of the sample the wave comes into contact with. After the evanescent wave interacts with the sample – liquid or solid – it passes back into the crystal and eventually back to the detector, where it is compared with the reference beam. This effect is most efficient when the crystal is made of a material whose optical properties include a refractive index higher than that of the sample. A solid sample is simply pressed into contact with the crystal, and held in place using a clamp or a press to prevent trapped air from distorting the signal. In the case of a liquid sample, there must be a shallow layer over the crystal. This is achieved by injecting the liquid into a flow cell, which creates a thin layer of fluid on the crystal.

3.1.2. Transmission FTIR

Transmission FTIR is done primarily on solid samples, such as polymer films, since it requires the sample to be perpendicular to the beam of IR light, a feat that is difficult to accomplish with a liquid sample. In the case of liquid samples, it is customary to utilize a super-sealed liquid cell with plates made from ionic salts, such as calcium Fluoride (CaF_2), which are transparent to IR light. In this method, the IR light beam is passed directly through the sample and to the detector. The amount of light reaching the detector (I) through the sample is compared with the amount of light generated by the IR light source (I_0) to calculate the transmittance of the sample. Transmittance follows the relationship:

$$T = \frac{I}{I_o} \qquad \text{eq. 2}$$

The results can be plotted as percent transmittance, though absorbance is most commonly used. Absorbance is calculated using the following relationship:

$$A = -\log_{10} T = -\log_{10}(\frac{I}{I_0}) \qquad \text{eq. 3}$$

3.3. Transmission Electron Microscopy (TEM)

TEM has its roots in the years just preceding the Great Depression. The very first TEM was built by Max Knoll, and Ernst Ruska in Germany during 1931 [42]. The group

went on to develop the first TEM with a resolving power greater than light two years later, and refining it into a commercial device in 1939.

In TEM, a beam of electrons is directed at an ultra thin sample, where the electrons interact with the sample as they pass through it. The imaging is done by reconstructing an image of the sample based on the electrons transmitted through the specimen. This image is magnified and projected onto a device which can display and save the image, like, for example, a fluorescent screen, photographic film, or a CCD camera.

TEM yields images of far greater magnification than those that can be produced with an optical microscope, due to the difference in the de Broglie wavelengths of electrons and photons. That is, the de Broglie wavelength of the electron is much smaller than that of the photon [43]. This is what allows the instrument to examine extremely small objects and fine detail, right down to a single column of atoms.

The most common mode of operation for imaging with a TEM is what is known as bright field imaging mode. In bright field mode, the contrast formation can be said to be formed directly by the number and position of the electrons that penetrate the sample. This results in thicker regions of the sample, or areas with a higher atomic number, appearing dark, while regions with no sample in the beam path appear bright.

The technique of TEM does have some drawbacks, however. One such limitation lies in the fact that many materials require extensive preparation before a sample thin enough to be electron transparent can be produced. Then there is also the possibility that the structure of the sample may be changed during this processing or that the sample may be damaged by the electron beam, especially in the cases of biological or polymer

samples. In addition to all of these limitations, one must also keep in mind that the field of view is very small, and the region analyzed is not necessarily characteristic of the whole sample. Of course, there is a very simple solution to this last problem: to take images of several regions of the sample.

3.4. Atomic Force Microscopy (AFM)

In AFM, rather than using photons or electrons, one uses a nanoscale cantilever with a very sharp tip to raster scan the surface of the specimen being imaged (this works like the record players of the 1960s and 70s but at the nanoscale). This tiny cantilever is usually made from materials such as silicon or silicon nitride, and the tip has a radius of curvature on the order of ten nanometers. When the minuscule silicon tip is brought close to the sample surface to be imaged, the forces generated by the interactions between surface atoms and the tip cause the cantilever to bend. The deflection in the cantilever tip follows Hooke's law, due to the scale of the distances involved. The image of the surface is created by a computer hooked up to a detector, made up of an array of photodiodes, that tracks the movement of the cantilever using a laser that is reflected off the cantilever's surface near the tip. Any deflection of the cantilever results in a corresponding deflection in the position of the laser beam reaching the detector. A schematic diagram of how the cantilever interacts with the surface of a sample can be seen in Figure 4.

Depending on the situation and specimen, a variety of different forces can be measured using AFM. These include mechanical contact force, van der Waals forces,

electrostatic forces, and magnetic forces, among others. We have used this technique to determine the morphological characteristics of our conductive films.

There are other methods, such as optical interferometry and piezoresistivity, that have been developed to improve the sensitivity of the AFM measurements. A piezoelectric cantilever, acting as a mechano-electric transducer, adds a cross-check to the optical methods used to track the deflections of the laser beam, improving the surface image accuracy.

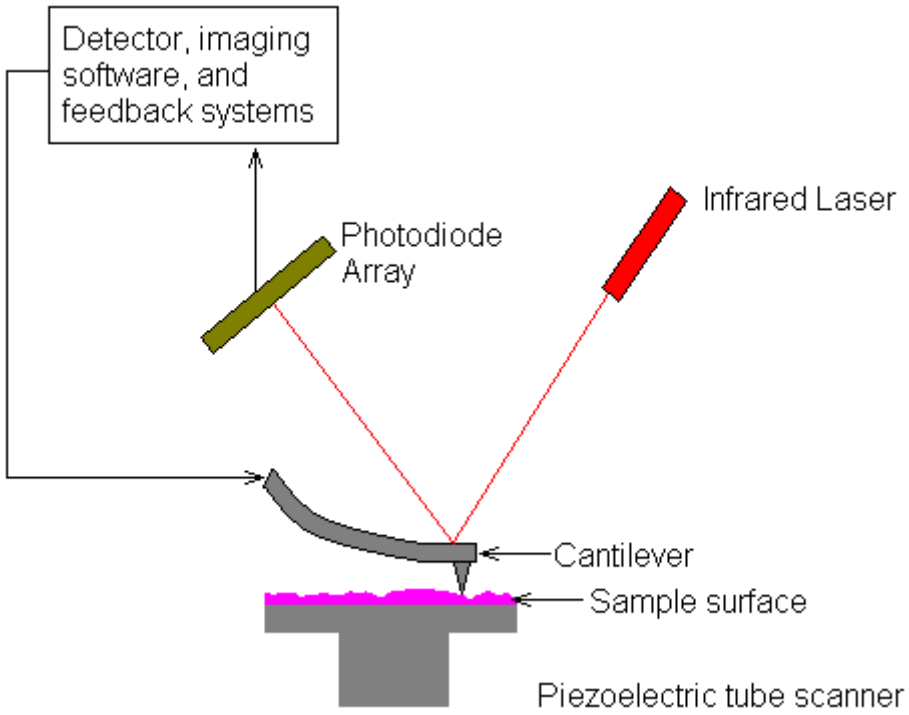

Figure 4: Schematic of the Principles Behind AFM Surface Imaging. The cantilever tip is brought into contact with the surface, and then is moved back and forth over the surface. In the process of performing this scan, the cantilever will deflect based on the height of the surface features it encounters, thereby causing the beam of the infrared laser to deflect. From these deflections a 3-D image is generated.

Using a Wheatstone bridge, the strain in the cantilever can be measured. This method is not as sensitive as laser deflection or interferometry. More information on how the Wheatstone Bridge works is referenced for the interested reader [44, 45].

Briefly, the Wheatstone Bridge is assembled out of two fixed resistors, one variable resistor, and the sample, as shown in Figure 5. When the current within the circuit is adjusted to zero by manipulating the variable resistor, the resistance of the unknown sample may be calculated using Ohm's Law[46] and the combination of Kirchoff's Current Law[46] and Kirchoff's Voltage Law[46]. In Figure 5, the known resistances are labeled R1, and R2. The name given to the variable resistor is R3. The source voltage is labeled Vs, and the unknown resistance is labeled X. The current sourced is denoted by Is. In a nutshell, when the current sourced is zero, the resistances R1+R2 = R3+X. Since R1 and R2 are known values, and the resistance of the variable resistor can easily be determined, the resistance of the sample can be calculated.

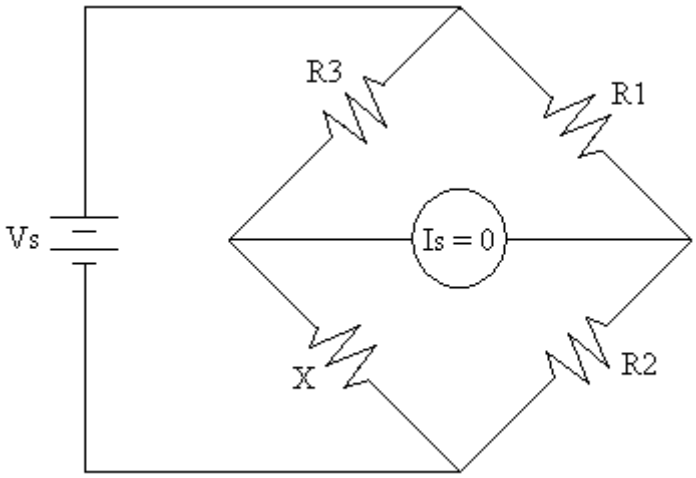

Figure 5: Circuit Diagram for a Standard Wheatstone Bridge. When Is is equal to zero, the resistances R1+R2 = R3 + X. From Ohm's Law and Kirchoff's Current Law, the unknown resistance X can be calculated.

Scanning a specimen with the cantilever kept at a fixed height can cause collisions between the cantilever and the surface, resulting in potentially severe damage

to the cantilever tip. In order to minimize the risk of breaking the tip of the cantilever, a feedback mechanism within the AFM machine is controlled with specialized software that is designed to automatically adjust and maintain the distance between the tip and the sample, as shown in Figure 4 [47].

Traditionally, the sample to be imaged is placed on a piezoelectric tube, as depicted in Figure 6, allowing the sample to move in the z-direction for the purpose of maintaining a constant force between the cantilever tip and the sample surface. In this case, the x and y directions are used for scanning the sample. Alternatively a configuration, known as a 'tripod' configuration, incorporating three piezoelectric crystals can be used. One piezoelectric crystal is responsible for scanning in each of the x, y and z directions, as depicted in Figure 6. This design eliminates some of the distortion inherent in the use of a tube scanner [48].

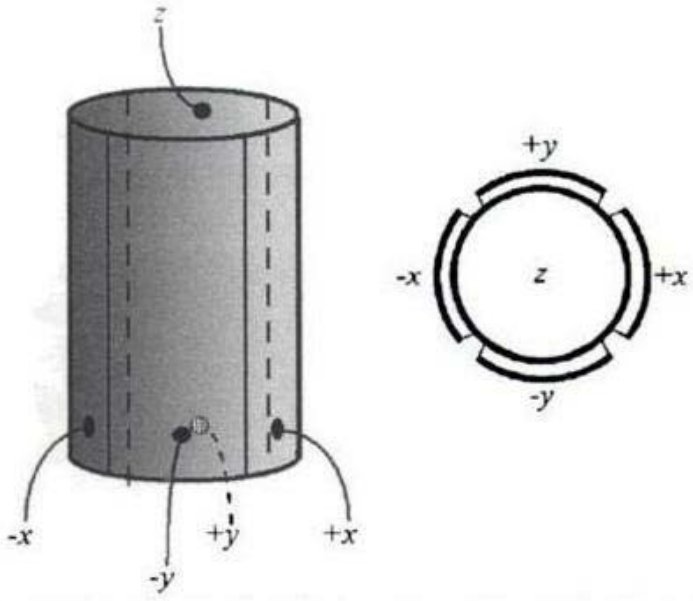

Figure 6: Schematic Representation of a Piezoelectric Tube Scanner. Shown are the five electrodes needed in +x, -x, +y, -y, and z. [48]

The AFM can also be operated in a number of different imaging modes, depending on the material and morphology of the specimen: “static” or contact modes that are generally used for “hard” samples such as silicon carbide, and a variety of “dynamic” non-contact modes, such as tapping mode, which are more useful for “soft” surfaces such as polymers and biological cells [49].

3.5. Four Point Probe

A four point probe is an instrument with four electrodes spaced evenly along a line. The design is based on a technique devised in the late 1950s by van der Pauw, an engineer working for Phillips [50, 51]. The four prongs of the four point probe are designated with a number as shown in Figure 7.

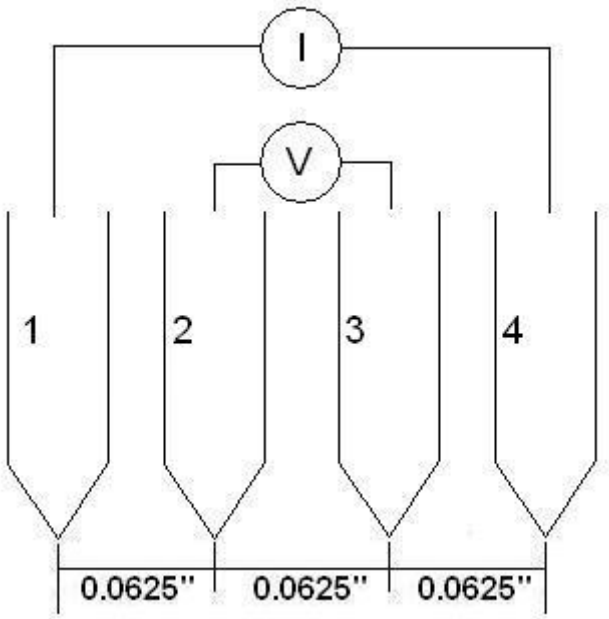

Figure 7: Probe Designations as Used in Four Point Probe Method.

The two outermost electrodes are used to supply a constant current, and the inner two are connected to a volt-meter. If we take the spacing between the electrodes to be *d*, *t* to be the film thickness, and the slab of material is assumed to be so much larger than the spacing as to appear infinite, the resistivity, ρ is given in micro-ohm-meters (μΩ-m) by the following equations [52]:

$$\rho = \frac{2\pi dV}{I}, \text{ for t>>s} \qquad \text{eq. 4.a}$$

$$\rho = \frac{\pi tV}{[\ln 2]I}, \text{ for s>>t} \qquad \text{eq. 4.b}$$

A quick dimensional analysis of equations (4.a) and (4.b) yields the following:

$$\rho = \frac{[\mu m][V]}{[A]}, \text{ for t>>s} \qquad \text{eq. 5.a}$$

$$\rho = \frac{[\mu m][V]}{[A]}, \text{ for s>>t} \qquad \text{eq. 5.b}$$

Both equations are given in units of volt-micrometers over amperes, which then can be readily converted into the conventional units of resistivity by recognizing that volts over amperes are actually ohms (Ω). This then leaves us with an equation that gives a result in units of μΩ-m.

This technique could be used to measure a film's thickness, as might be inferred by the thickness term in equation (4.b), but it is generally used to measure the electrical conductivity of a thin layer, or the bulk resistivity of bare wafers.

The drawback of this method is its tendency to cause minor surface damage and leave small deposits of metal on the sample, and, while this damage is not severe, it is sufficient to render it useless for tests on wafers or films meant for device fabrication [53].

3.6. Ellipsometry

Ellipsometry is an optical technique to measure the thickness and to probe the dielectric properties of thin films. It provides unsurpassed capabilities for the non-destructive and contact-free characterization of thin films. This technique is based on the analysis of changes in the polarization of light reflected by a sample. Thus, layers whose thickness is less than the wavelength of the light used to probe the sample can be analyzed, extending down to even monatomic layers [54, 55].

One caveat to keep in mind when using this technique, however, is that it assumes discrete well-defined layers that are optically homogeneous and isotropic. If these assumptions are not true, a more complex variation of the technique is required.

3.7. Optical Microscopy

In using an optical microscope which uses lenses, the theoretical resolving power is one half the wavelength of the light used to view the sample. This limit is never quite reached, however, as a result of the limitations imposed by the use of optical lenses. These include the finite dimensions of the lens act as an aperture restricting the acceptance of light rays from the sample, and loss of detail due to aberrations in the

focusing properties of the lens [56]. Optical microscopes come in a variety of different types including polarized light microscopes, inverted light microscopes and phase contrast microscopes [57].

Chapter Four: Experimental

4.1. Film Fabrication

The materials to be used in this study are polycarbonate (PC) resin provided by Acros Organics with molecular weight 45,000 (catalogue number: 178315000), Bis(ethy1enedioxy)tetrathiafulvalene (BEDO-TTF) made by Synchem OHG and having a purity of 99% (catalogue number: jg020), and the solvent, American Chemical Society grade dichloromethane (DCM), with a purity of 99.9%, made by Fisher Scientific (catalogue number: D37-4). Also used was elemental iodine of purity 99.8%, provided by Sigma Aldrich (catalogue number: 207772).

The films were fabricated by our collaborators in the Department of Chemistry, using a technique based on that of Jeszka *et al*. [8] The films were made by measuring out polycarbonate to approximately 1 wt% of the solvent, dissolving it in dichloromethane (DCM), and adding Bis(ethylenedioxy)-tetrathiafulvalene (BEDO-TTF) at a concentration of 1 wt% or 2 wt% of the polycarbonate. The solution was poured into molds and the solvent allowed to evaporate.

Two different methods were used in the process of vapor doping the films, as shown in Figure 8, so, at this point, the films were cut to 1.5 cm x 1.5 cm or 1 cm x 1 cm, for use in method 1 or method two, respectively, and then doped by the addition of iodine in a variety of different concentrations, using vapor exposure at room temperature. This was done so that the effects of a concentration gradient on the film properties could be

investigated. The use of method 1 caused the formation of a concentration gradient in the iodine, which lead to uneven doping of the film surface, with most of the iodine depositing on the areas of the film closest to the solution. This allows the relationship between the distance from the iodine solution and the resistivity of the film to be studied. Method 2 was designed to allow exposure of the films to iodine at equilibrium. Because the film is level relative to the surface of the iodine solution, there is only minimal concentration gradient induced when the films are doped and they are doped as homogeneously as possible over their surfaces. The properties of the film doped in the presence of a concentration gradient were compared to the propertied of the film doped using method 2.

There is an additional difference in the two methods of vapor doping, besides the position of the film, however: the polycarbonate was used as obtained in method 1, and purified before use in method 2. The polycarbonate, as obtained, was not totally pure. This could potentially have an impact on the performance of the films fabricated without purifying the polycarbonate. Therefore, the films prepared with method 1 were done on unpurified polycarbonate and those films doped with method 2 were prepared using purified polycarbonate.

The long term goal is to be able to combine the polycarbonate film with the gold nanoparticles, so that the conductivity of the film is increased.

Various PC and PC-dye films were prepared. To ensure reproducibility and a good sampling average, at least three films for each concentration need to be prepared and characterized.

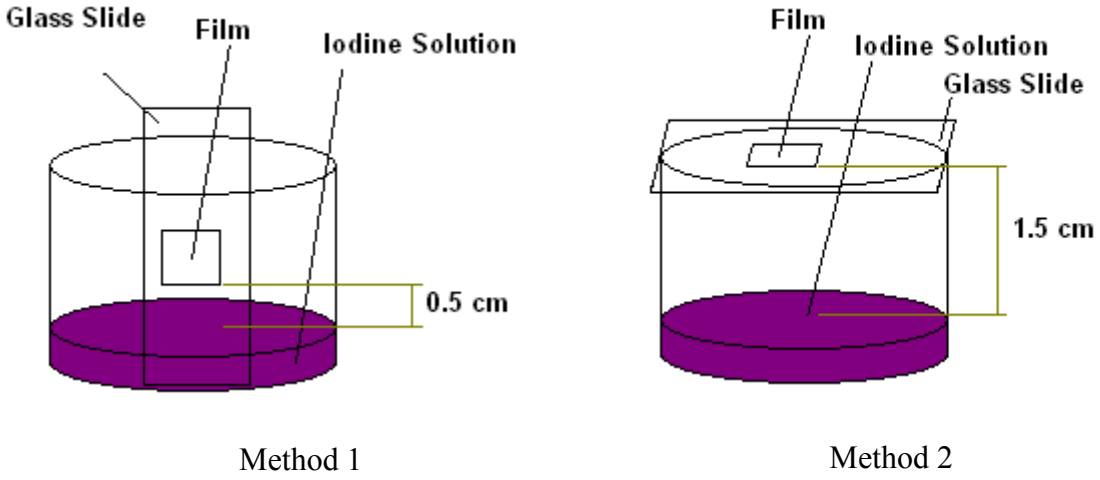

Figure 8: Methods of Vapor Doping Used in This Study. In method 1, the film is exposed vertically in a non-equilibrium system open to the air. In method 2, the film is exposed horizontally, at equilibrium.

4.2. Four Point Probe Experiments

Four point probe experiments were done using a Keithley 6221 sourcemeter, a Keithley 6514 electrometer, and a Signatone four point probe model S-301-4. The source meter was set to keep a compliance voltage of 105 V, while the current sourced was incrementally raised until the compliance voltage was reached. The voltages across the four point probe were noted down at each increment of the current, so that the resistance could be calculated for a given current sourced. A 300mm diameter p-doped silicon (100) wafer, obtained from MEMC electronic materials and donated by Dr. John Wolan, with a nominal resistivity of 14-22 Ω-cm was used as a reference.

The differences in the two methods used to dope the films necessitated the use of two different measurement methods. The resistivities of the films made with method 1 were measured at twelve locations on the film, starting at the bottom of the film (nearest to the doping solution), and moving up the film (away from the doping solution) in

increments of 1 mm. Films doped with method 2 were tested in a randomized fashion, and the locations of the tests were noted. The results for method 2 were averaged to calculate an average resistivity and conductivity of the films. These methods are shown schematically in Figure 9. The results are discussed in Section 5.1.

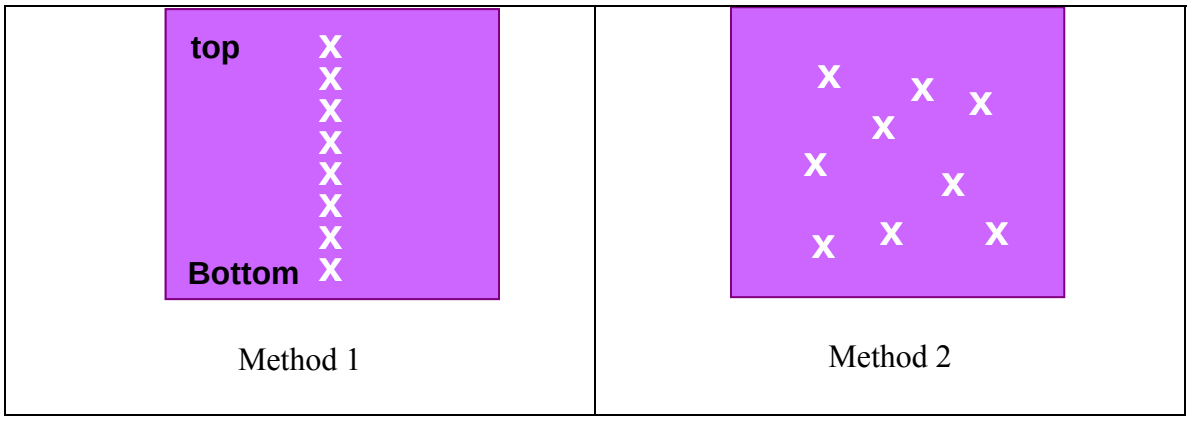

Figure 9: Measurement Methods used to quantify the Resistance of Films doped with Method 1 and Method 2. Because there is a concentration gradient present in the iodine when using method 1, the films were characterized using a series of measurements taken along the center of the film, from bottom to top. Because method 2 produces nearly homogeneous films, the films were tested in ramdom positions across their surfaces, as shown.

4.3. FTIR Settings and Information

The films were examined using a transmission accessory in a Nicolet 6700 spectrophotometer. This allowed for the collection of data across the full spectrum of wavelengths provided by the machine: 4000 to 400 cm^{-1}. This equates to a range of wavelengths from 2.5 μm to 25 μm. The films were also analyzed using ATR-FTIR. A zinc selenide (ZnSe) crystal was used, in conjunction with a flat plate accessory on a stand that incorporated potassium bromide (KBr) windows. The use of the ATR accessory limits the range of wavenumbers that can be collected and tested to the range

from 4000 cm^{-1} to 720 cm^{-1}. Data gathered was analyzed using the Omnic 7.2a software distributed by Thermoscientific.

4.4. TEM Images

TEM images were taken on a Morgagni 268D electron microscope, using settings of 100 kV, and 60 kV at a variety of magnifications.

4.5. AFM Surface Scans

AFM images were taken on an XE-100 Advanced Scanning Probe Microscope. Images were taken in tapping mode using a classic silicon (Si) or silicon nitride (SiN_4) cantilever. The scan sizes of the images were 10x10 μm, 5x5 μm, 2x2 μm, and 0.5x0.5 μm.

4.6. Optical Microscopy

Optical microscope images of the films were taken using 25x, 100x, and 400x magnification.

Chapter Five: Results and Analysis

5.1. Four Point Probe Studies

The four point probe tests conducted were done to determine whether the films followed Ohm's law, and, if so, what the surface resistivity was before and after the polycarbonate/BEDO-TTF films had been doped. An overview of the results is as follows:

Before going into any detail, there are some general observations worth noting. First, and foremost, before doping, the films are clear with an orange or pink tinge where the dye is concentrated. After doping, areas with higher dye concentrations turn into darker shades of purple, whereas areas with lower dye concentrations remained purplish. Secondly, during doping some films will acquire a metallic sheen. These films show higher conductivity values than the films that do not have a metallic sheen. Thirdly, if the films are doped for too long, meaning that they have been overexposed to iodine, they will turn from purple to green, and are then no longer conductive. As a result, longer doping times do not necessarily mean better that the films will show better conductivity. Fourth, it was noted after several tests done on films containing 1 wt% of BEDO-TTF dye that the 12 mg/mL doped films were consistently not conductive. As a result the concentration of the BEDO-TTF was raised to 2 wt% for all subsequent experiments.

Lastly, if the films are shown to follow Ohm's Law, it should be noted that the inverse of the slope of the plotted current and voltage data will be equal to the resistance of the film.

The method used to test the films containing1 wt% BEDO-TTF was simply to place the four point probe in contact with the surface, and to source a current. The amount of that current that was transmitted was then observed. This experiment design is shown schematically in Figure 10.

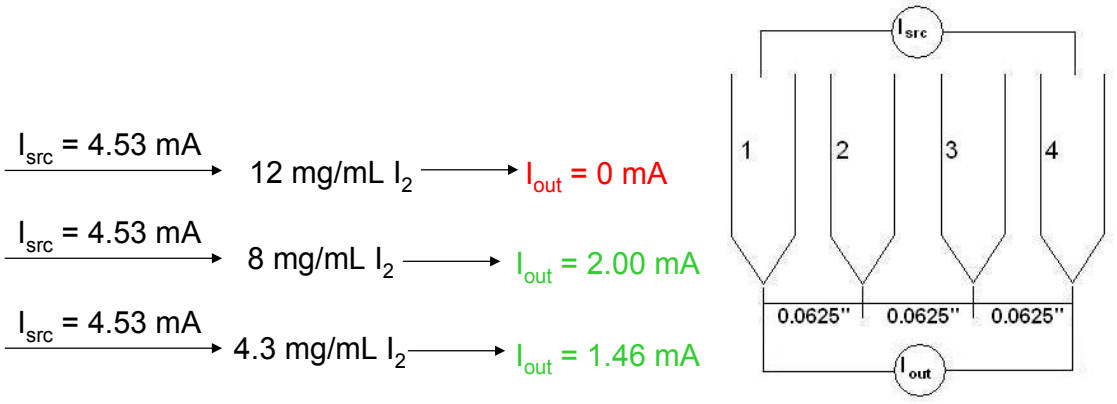

Figure 10: Method Used to Test Films Containing 1 wt% BEDO-TTF for Conductivity. Films were doped and then tested once with the FPP to determine whether they were conductive, and, if so, how much of the current sourced was transmitted.

Testing of the four point probe, electrometer, and current source, using the p-Silicon wafer as a reference showed that the setup was functioning properly. The nominal resistivity of the p-Silicon wafer was given by the manufacturer to be 14-22 Ω-cm. The current-voltage data collected for the reference wafer is shown in Figure 11.

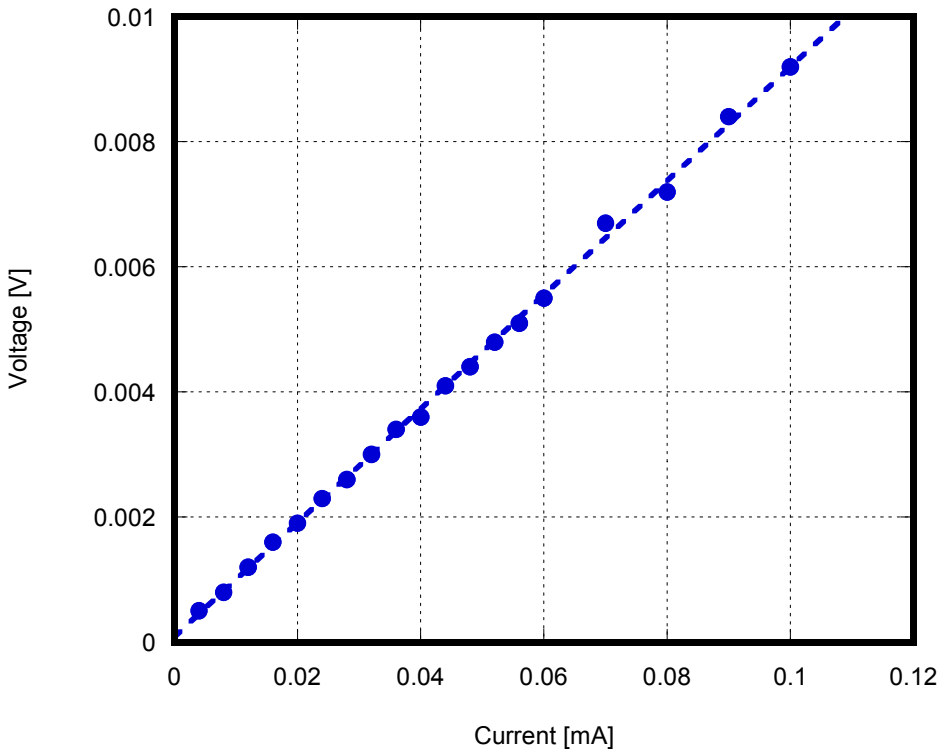

Figure 11: Current-Voltage Data for P-doped Silicon Wafer. In order to ensure that our setup was working properly, a p-doped silicon wafer with a known resistance of 14-22 Ω-cm was tested, and the resistivity was caculated. A result of ρ = 14.5 ± 0.2 Ω-cm was obtained.

From the current-voltage data collected for the p-doped Silicon wafer, the resistance of the wafer can be calculated to be 91.091 Ω. This resistance is then multiplied by the interprobe distance of the four point probe instrument, 0.0625 inches, and converted into the correct units as follows, and the error was calculated based on the repeat measurements which were taken in other randomly chosen locations on the wafer.

$$\rho = R * d \qquad \text{eq. 6}$$

$$\rho = (91.091\ \Omega)*(0.0625\ \text{in})*(2.54\ \text{cm/in})$$
$$\rho = 14.5 \pm 0.2\ \Omega\text{-cm}$$

The next step taken was to optimize the iodine exposure time for each of the following concentrations: 12 mg/mL, 8 mg/mL, and 4.3 mg/mL. A film containing 2 wt%

BEDO-TTF dye was doped for 30 seconds using method 1, then conductivity data was taken in one place on the film. The same film was then doped with method 1 for another 30 seconds, and tested again. This cycle was repeated until the resistance of the film no longer showed large changes after each exposure. The results for the 12 mg/mL solution are plotted in Figure 12. Results for the other two concentrations look similar, and can be found in Appendix A.

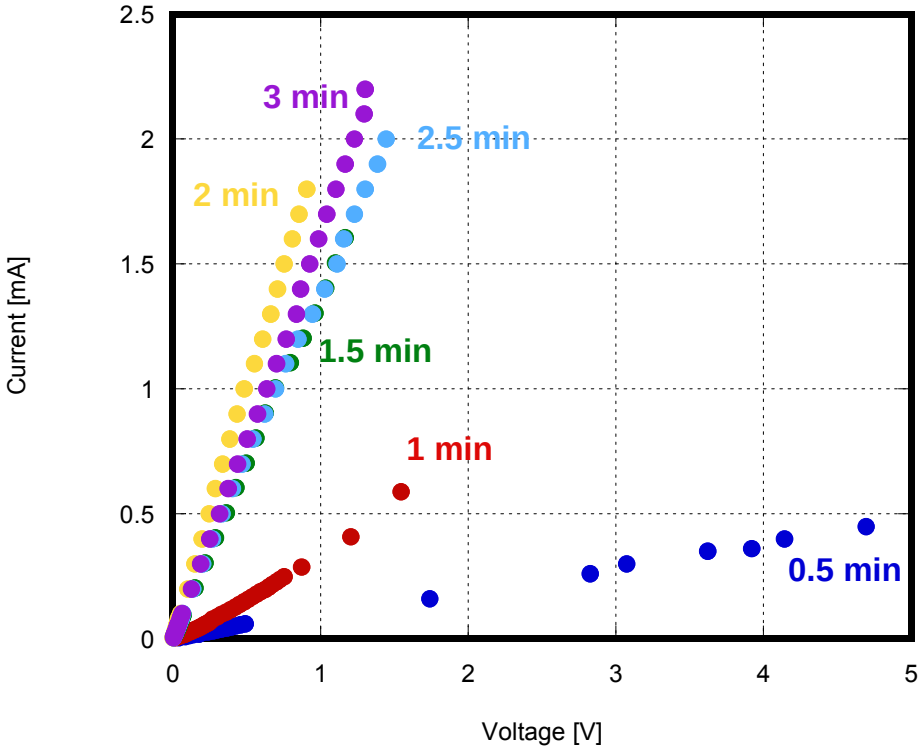

Figure 12: Current-Voltage Data for Optimization of Iodine Exposure for 12 mg/mL solution. Plotted here is the current-voltage data for a film doped using method 1 for a variety of exposure times. The films were exposed to the iodine solution in increments of 30 seconds until the resistance (the inverse of the slope) no longer changed dramatically.

One can easily see at a glance, keeping in mind that the slope is equal to the inverse of the resistance of the film, that as the films are doped for longer times, the resistance decreases until a time of two minutes is reached. Doping the films longer than

two minutes, no longer decreases the resistance. This can be seen illustrated in Figure 13, in which the resistivities for the 12 mg/mL film are plotted against the length of time for which they were exposed to the iodine solution. The values have been fitted with a power fit, to better illustrate the relationship between the resistivity and the exposure time.

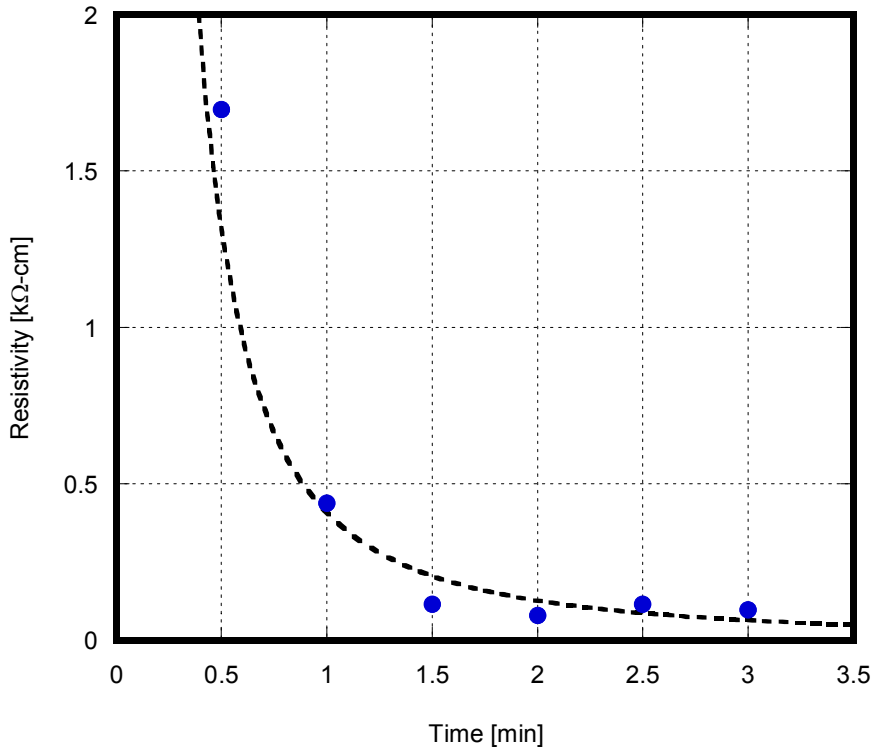

Figure 13: Resistivity versus Exposure Time for 12 mg/mL solution. This plot presents the data from Figure 12 in a slightly different way, for clarity. Seen here is a plot of the calculated resistivities of the films against the length of time for which they were exposed.

Because the sets of films doped with method 1 exhibit a large concentration gradient, as shown in Figure 13, to obtain an average value for the resistivity is meaningless. Figure 13 presents the data obtained for the 12 mg/mL iodine solution at an exposure time of two minutes. Shown in Figure 14 is the measurement data for the film

doped in the 12 mg/mL solution using method 2. Similar data for the two remaining concentrations can be found in Appendix A.

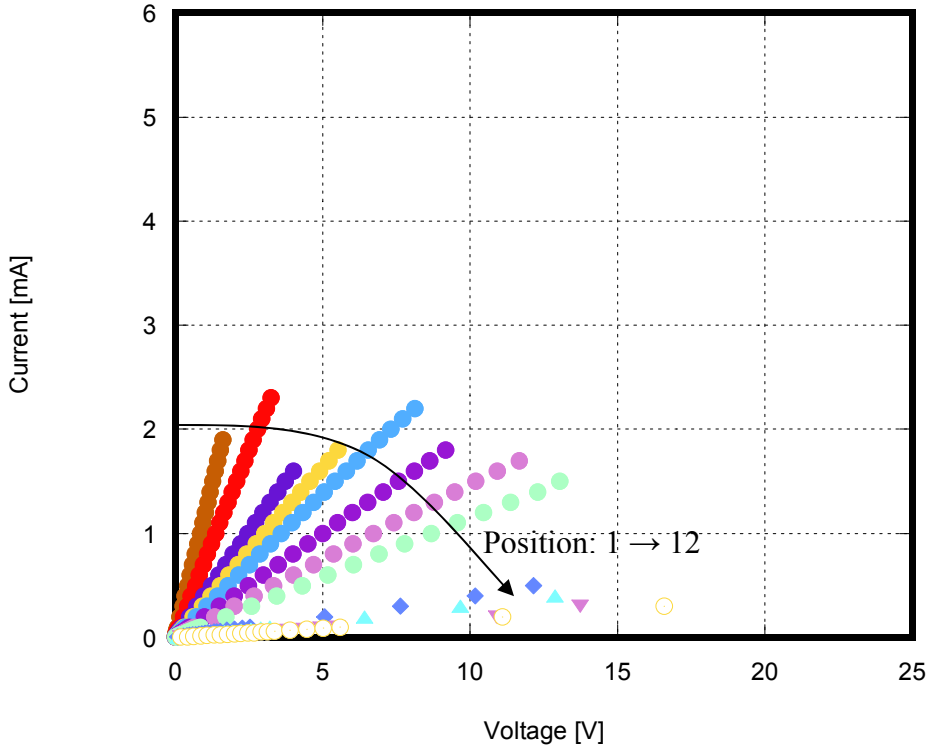

Figure 14: Current-Voltage Data for 12 mg/mL Iodine Solution Concentration Exposed for Two Minutes using Method 1. Numbering of 1 to 12 represents distance along the film, where 1 is at the bottom, nearest the doping solution, and 12 is at the top, farthest away from the solution.

The measurement data presented in Figure 14 shows the increase in the resistivity as the distance from the doping solution increases. This seems to indicate that the resistance of the film increases as the amount of iodine deposited decreases. In the case of those films doped using method 2, a much more even deposition of iodine was seen, as was predicted. The effects of this homogeneity could be seen in the resistance, and, by extension, the resistivity and conductivity of the films. Where the resistance had a very wide range after doping with method 1, in films doped with method 2, the resistances found at each position on the film surface were clustered closely around one central

value. The resistivity of the films doped with methods 1 and 2 are plotted in Figures 15 and 16 against the position on the film where the measurement was taken.

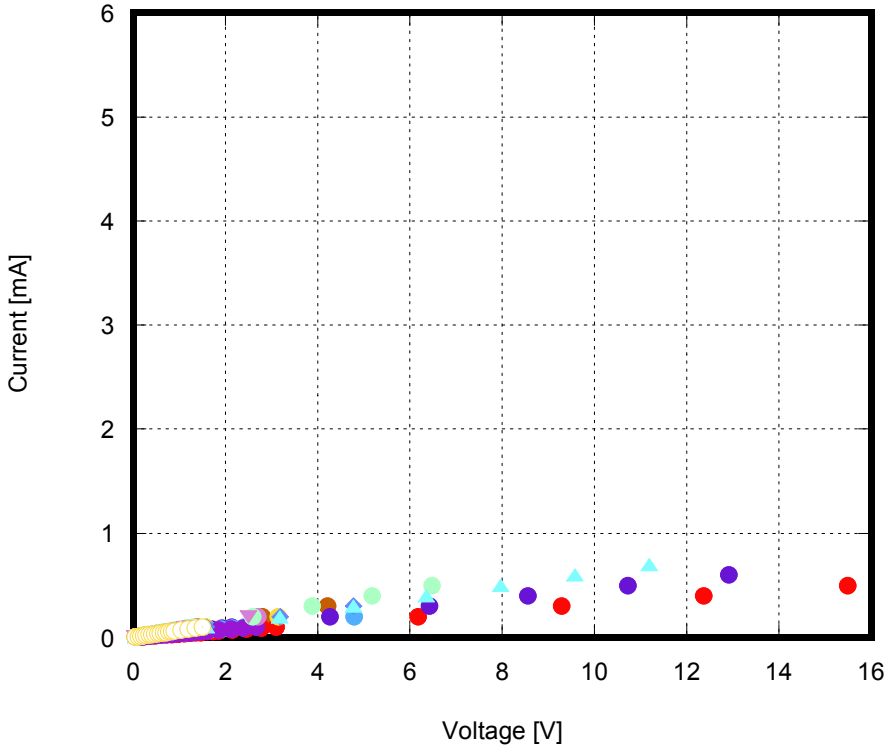

Figure 15: Current-Voltage Data for 12 mg/mL Iodine Solution Concentration Exposed for Three Minutes using Method 2. It is immediately apparent from this plot that instead of a range of resistances, as was seen in method 1, the resistances are tightly clustered around one average value.

As can be seen by comparing Figures 15 and 16, the range of the resistances of the films in method one is not in evidence when method 2 is employed. Films doped with method 2 show a comparatively low resistance compared to films doped with method 1, as well as a much narrower range of values. Applying a linear curve fit to the data yields a set of three horizontal lines. This shows that any error in the measurements is random and due to random processes, rather than being caused by the effects of a variable that has not been accounted for in taking the measurements.

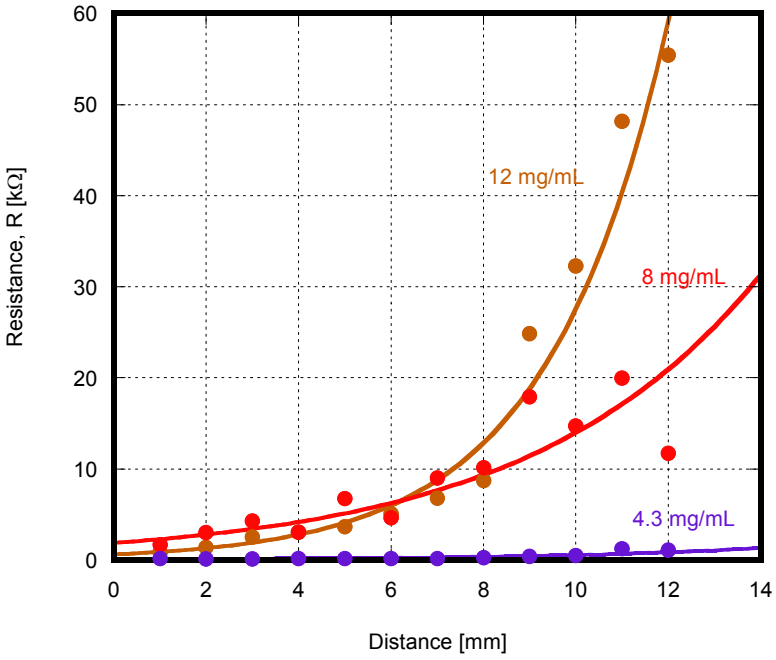

Figure 16: Resistance versus Distance for Films Doped Using Method 1. Shown in this plot is the relationship between the resistivity and the distance away from the iodine solution. The resistance rises dramatically as distance from the solution increases for two of the three concentrations.

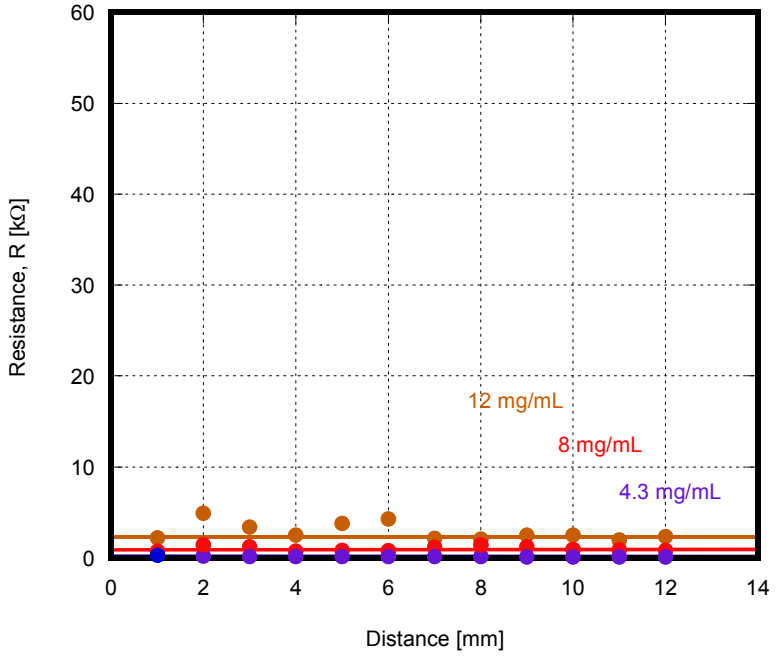

Figure 17: Resistance versus Distance for Films Doped Using Method 2. Shown in this plot is the relationship between the resistivity and the position on the film where each measurement was taken. The resistance stays within a very narrow range, compared to that of method 1, with only very small variations.

Because the resistance of the films doped using method 2 is almost homogeneous over the film surface, as shown by the measurements presented in Figure 17, and because any error in the measurements can be attributed to the inherent randomness in the deposition of iodine using the process of vapor doping, it is possible to take an average of the calculated resistivities without biasing the calculation.

The calculated average resistivities of these films ranged from 148 Ω-cm, in the case of the film doped in the 4.3 mg/mL solution for 10 minutes, to 1060 Ω-cm for the film doped in the 8 mg/mL solution for 4 minutes, to 2822 Ω-cm for the film doped in the 12 mg/mL solution for 2 minutes. Calculating the conductivities for the three doped films, values of 35.4, 94.3, and 67.2 $mS\text{-}cm^{-1}$ are found for the 12, 8, and 4.3 mg/mL solutions, respectively. The conductivities of the three doped films, two types of conducting polymer, and two commonly used conductive metals are plotted in Figure 17, for ease of interpretation. Compared to the resistivities of copper or gold, which are 1.68×10^{-9} Ω-cm and 2.214×10^{-9} Ω-cm, respectively, the resistivity of our polymer films is very high, but when compared to the two conducting polymers, the difference in conductivity is not as great., There is potential that the doped polycarbonate films will match the conductivities of polyaniline or polypyrrole after doping optimization and the addition of the gold nanoparticles.

The attentive reader will note that the film which was doped with the most concentrated iodine solution shows the lowest conductivity, while the film doped with the least concentrated iodine solution shows the highest conductivity. This is believed to be a result of the length of time the film was exposed to the doping solution. The film doped

with the 4.3 mg/mL iodine solution was doped for a period of 10 minutes, whereas the film doped with the 12 mg/mL solution was only doped for a period of 2 minutes.

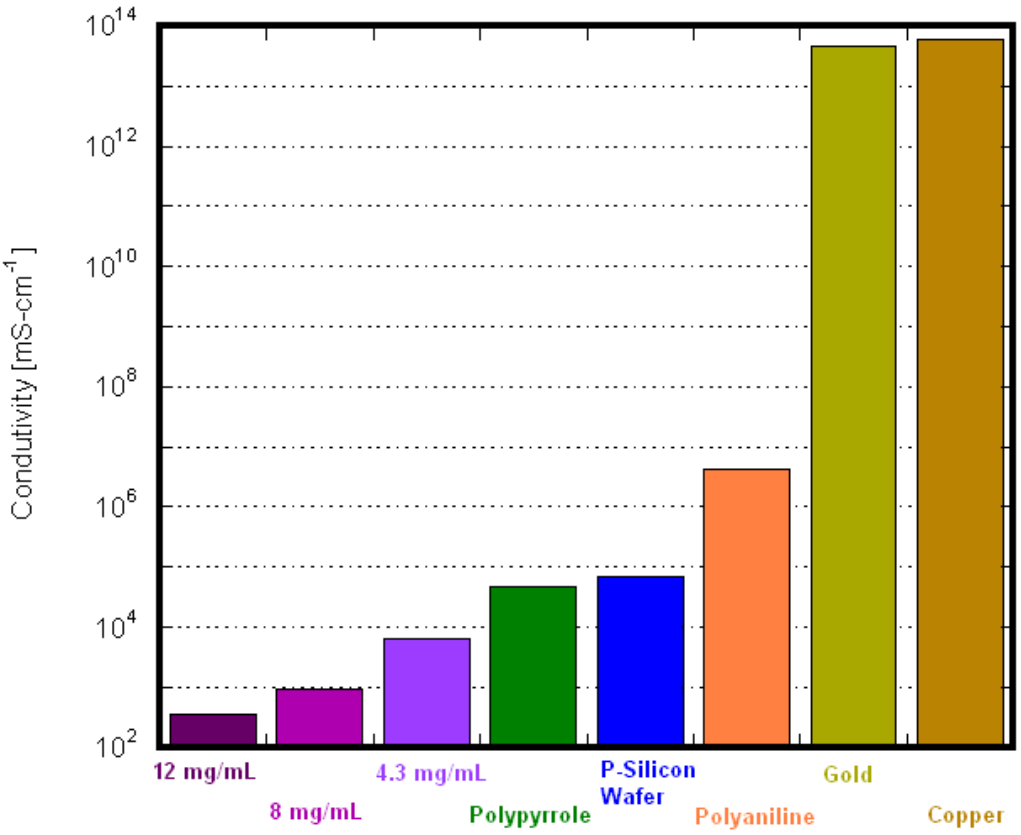

Figure 18: Average Resistivities of Films and Reference Materials: p-Si (100) Wafer, Polyaniline, Polypyrrole, Gold, and Copper. When compared to polyaniline or polypyrrole, the films fabricated in this study do not quite reach the same levels of conductivity. There is good potential that they might do so after optimization of all components has been done.

There is an additional optimization that must take place besides the optimization of the film conductivity, if these films are to be used in conjunction with dichromatic materials as sensors in the future: that of the film transparency.

Before doping, the polycarbonate films are transparent in the visible range, and acquire a pink/orange tinge after the addition of the BEDO-TTF dye. After doping, the

films darken, picking up brilliant colors. Where the iodine is deposited on the film surface, the dye goes from little pink/orange to purple, as seen in the film doped for two minutes in the 12 mg/mL solution, depicted in Figure 19 (bottom right image), and then, as more iodine is deposited, the films develop a dark green metallic sheen, as seen in the film doped in the 4.3 mg/mL solution for 10 minutes, also shown in Figure 18 (bottom left image). In the boxes below the images of the films in Figure 19 are given the average conductivity values found for each doping concentration and time, as well as the ratio of the conductivity to the highest value found in terms of percentage. Meaning that the conductivity value for the film doped in the 4.3 mg/mL solution for 10 minutes was taken as 100%, and the values for the other two films were then calculated from this value.

It can be readily seen that, if a film is to be developed that will be both transparent and conducting, some work needs to be done to determine what the highest conductivity is that can be achieved while maintaining the transparency of the film. This would lead us to speculate that, since its transparency is the highest of the three conductive films, the 12 mg/mL doped film should be the one chosen for optimization.

5.2. Imaging Analyses

Images of the polycarbonate films, before and after doping, taken by three different imaging techniques will be discussed in this section. Images of the films were taken using AFM, TEM, and optical microscopy, hereafter referred to as OM.

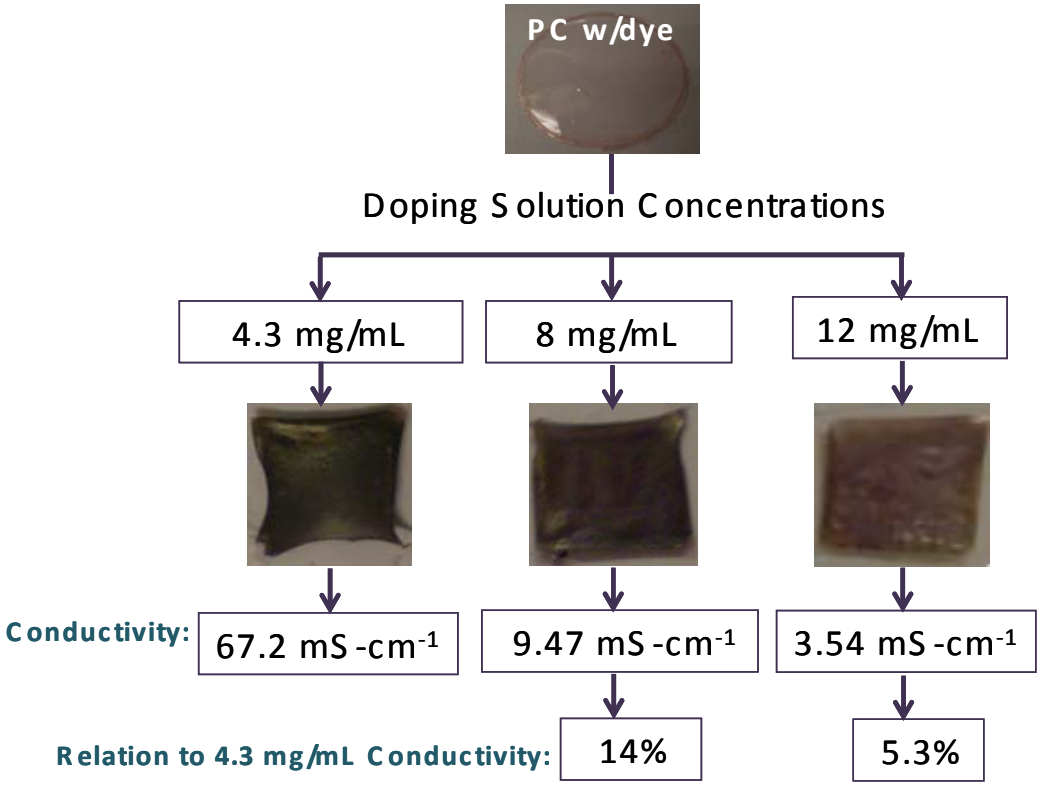

Figure 19: Flowchart Showing the Changes in Transparency Before and After Doping. Also shown are the conductivities measured for each film and the percentages relative to the 4.3 mg/mL conductivity.

In Figure 20, images of the film topographies and phase analyses are presented for the undoped polycarbonate and polycarbonate/BEDO-TTF films. The topography of the polycarbonate film shows a very smooth surface with what appear to be some uneven areas in the bottom left corner. The phase analysis of the polycarbonate film reveals that there are no inclusions of other foreign materials on the polycarbonate surface.

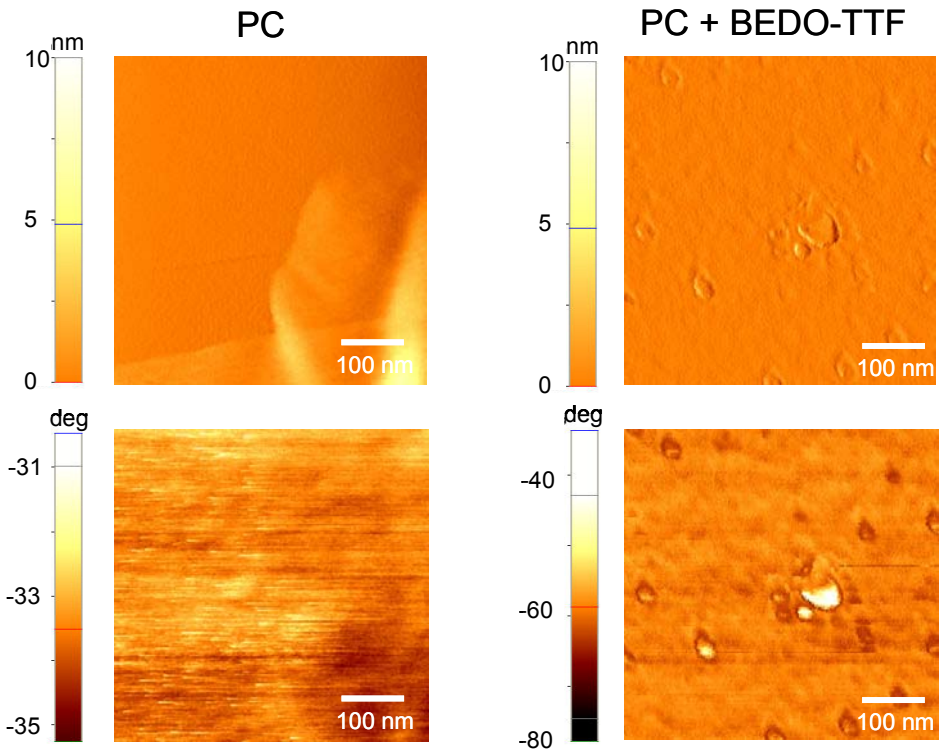

Figure 20: AFM Images of the Polycarbonate Films With (right) and Without (left) BEDO-TTF Dye. Top right and left images are of the film topography, and the two bottom images are of the phase analysis. The PC presents a very smooth surface, while the PC/BEDO-TTF composite shows the appearance of pore-like structures.

Once the BEDO-TTF dye has been added, the composite film shows structures appearing on its surface that resemble pores. The phase scan of the same film shows the appearance of a different material within the largest of the pore-like structures, which suggests that the BEDO-TTF dye could be aggregating there.

In OM images taken of the same two films, similar structures were observed, as shown in Figure 20. The polycarbonate film presents a very smooth surface and shows some features similar to the pores seen in the polycarbonate/BEDO-TTF film, though they are less in number. The polycarbonate/BEDO-TTF film displays the same features,

but in higher density. More features appear in the same area, and the surface appears rougher, as a result.

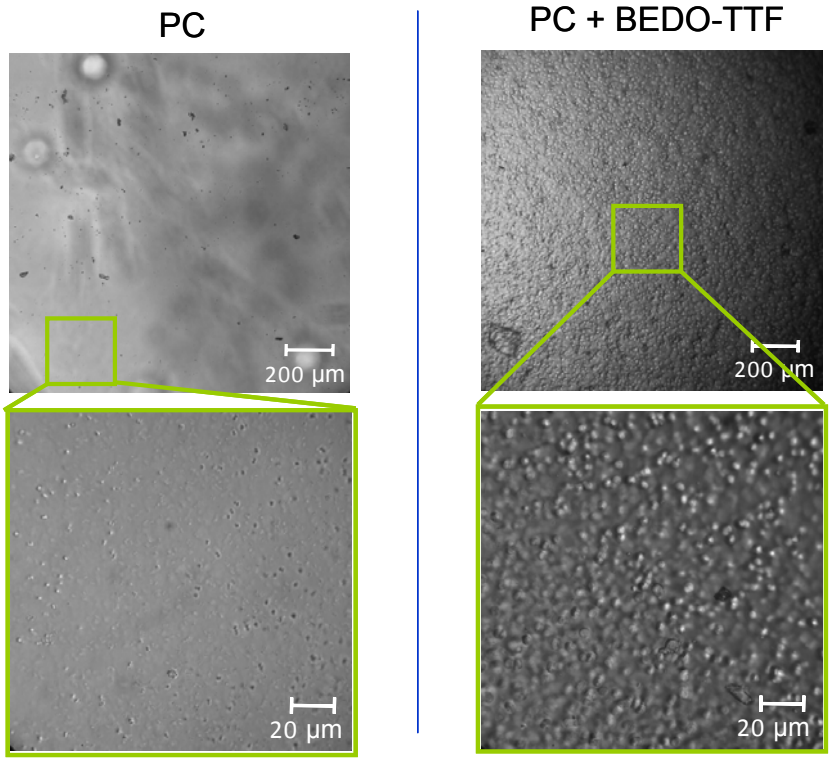

Figure 21: Optical Microscope Images of PC and PC/BEDO-TTF Films Under 100x and 400x Magnification. Features similar to the pore-like structures seen in the AFM images are present in both films.

OM images of the films doped with method 1 show a very clearly defined interface between the area on the film where the iodine has been deposited on the surface, and the area where it has not. An example is shown in Figure 22, which presents the images taken of the film doped with the 8 mg/mL solution for four minutes. Images of the films doped using the other two solution concentrations can be found in Appendix B.

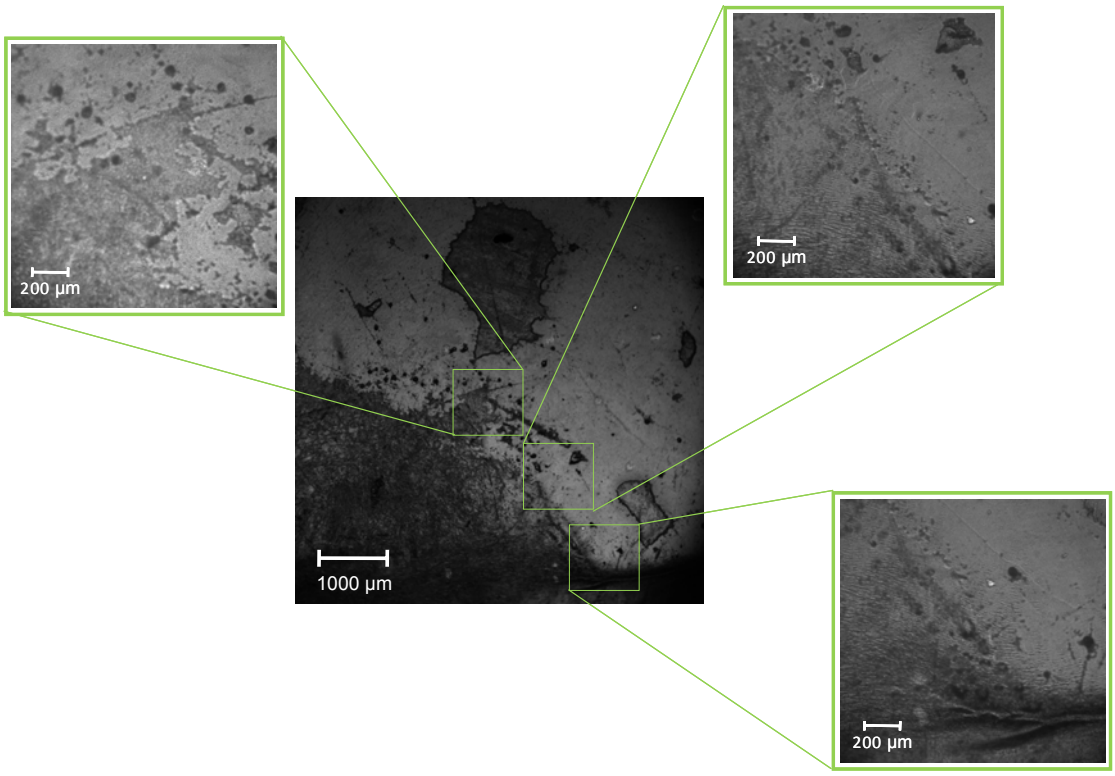

Figure 22: Optical Microscopy Images of the 8 mg/mL Doped Film Taken at 25x and 100x. The transition between the heavily and lightly doped regions of the film is shown. The very dark area contains more iodine than the lighter one.

AFM surface scans of films doped with method two reveal that as the exposure time increases and the iodine solution concentration decreases, the crystal sizes observed in the deposits on the film surface increase. Figure 22 presents the topography and phase scans of the films exposed to the three different iodine solutions. From the images, it can be readily seen that the increase in the surface roughness seen as the doping time increases corresponds to a dramatic increase in the crystallinity of the iodine deposited on the film surface. In the case of the film doped for two minutes in the 12 mg/mL solution, nucleation sites can be seen that appear to be the precursors of iodine crystals, but there are no crystals, as of yet, and the features seem to be lacking a long range order. When the film doped in the 8 mg/mL solution for four minutes is considered, more defined

crystal-like structures can be seen, but the features remain indistinct. The jump to an exposure time of ten minutes at a concentration of 4.3 mg/mL brings with it the formation of large well-defined crystals, and a large increase in the conductivity of the film. This seems to suggest that the formation of the iodine crystals results in higher film surface conductivity.

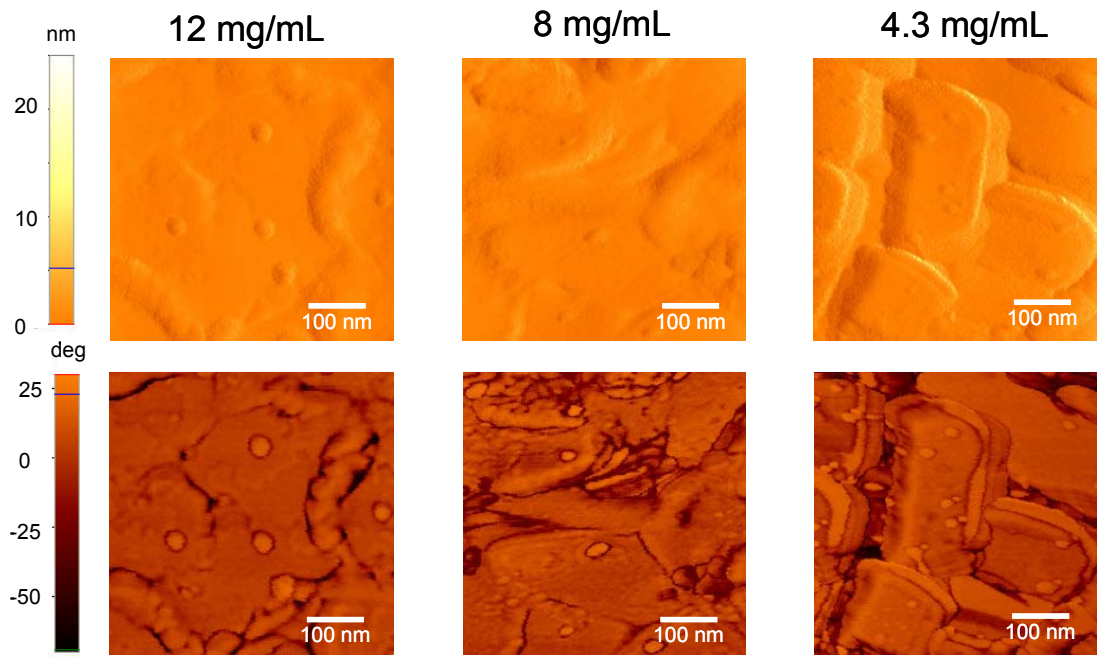

Figure 23: AFM Surface Topography and Phase Scans of Films Doped With Method 2. Images were taken in 0.5 µm x 0.5 µm size. Images in the top row are topographical scans, and images in the bottom row are the phase scans of the same areas. An increase in the crystallinity of the iodine depositions as well as in the surface roughness can be seen with increasing exposure time and iodine loading. The phase scans show that the only material being scanned is iodine and the entire film surface has been covered by the iodine.

The phase scans show that there are no changes in the material that the AFM cantilever tip encounters as it scans the surface: all it sees is iodine. This indicates that there is a homogeneous layer of iodine forming, confirming the validity of the FPP conductivity measurements.

OM images of the films doped with method 2 show a trend as well. Presented in Figure 23 are images taken using the OM of the films doped in the three different concentrations of iodine solution. Instead of displaying surface characteristics that have to do with the crystallinity of the iodine deposited on the film surface, the films show an increase in the surface roughness that parallels the increase in surface roughness that is predicted by calculations done using the AFM imaging software. The surface roughness values for the films doped with methods 1 and 2 are shown in Figure 24. Also shown in the upper right corner of the plot for method 1 is an image of the film doped using method 1 in the 4.3 mg/mL iodine solution for ten minutes.

In the images of the three doped films, there is an increase in the surface roughness and conductivity as the iodine concentration in the solution decreases and the time the film is exposed to the solution increases. This suggests that longer exposure times and lower iodine concentrations allow the iodine atoms more time to self-assemble into crystalline structures on the film. When method 1 is employed, uneven random depositions of iodine that do not form crystals are seen. Interestingly, there appears to be a threshold exposure time or iodine crystal size between four minutes and ten minutes at which the polycarbonate film buckles and forms maze-like wrinkles.

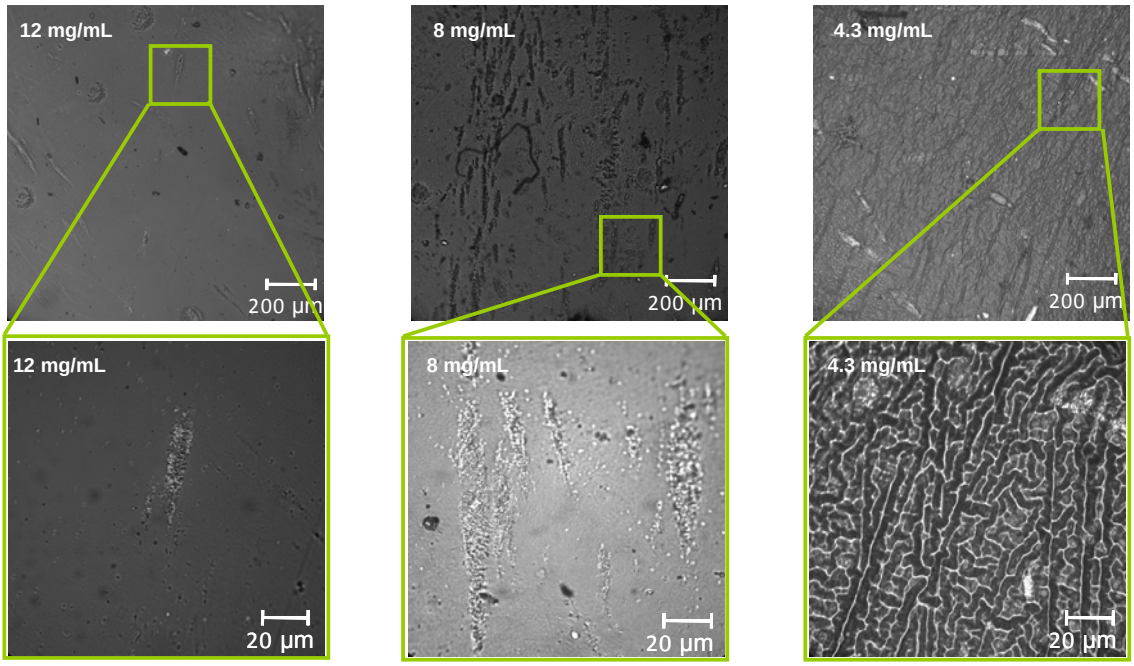

Figure 24: Optical Microscopy Images of the Films Doped in the Three Different Iodine Solution Concentrations Taken at 100x and 400x. There is a dramatic increase in the surface roughness of the films as the exposure time and iodine loading increase. This increase also correlates to an increase in the surface roughness and the film conductivity.

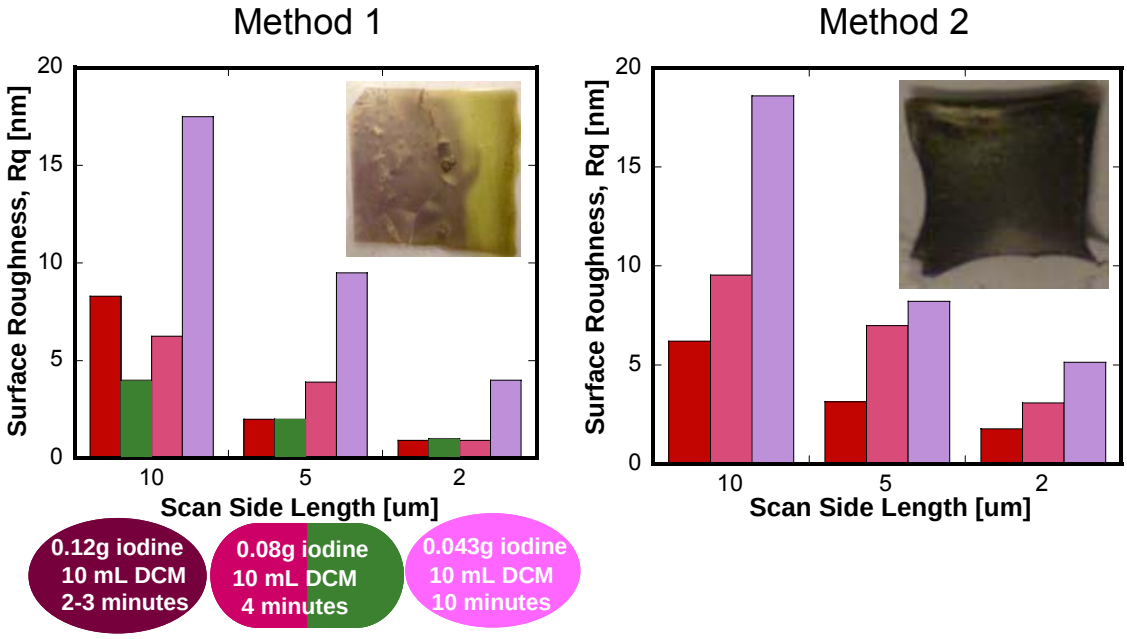

Figure 25: Surface Roughness Calculated From the AFM Images of Films Doped with Methods 1 and 2. Shown in the inserts are images of the films fabricated with each method. In these plots, the surface roughnesses calculated from the AFM scans are presented in graphical form. The tendency toward increasing surface roughness as the iodine loading is clearly shown for both methods.

It can be seen that all three of the imaging techniques used show a general trend of increasing surface roughness with increasing iodine loading of the films. This increase of the surface roughness also correlates with increasing conductivity. This correlation implies strongly that the surface roughness may be directly related to the conductivity of the films fabricated. This could potentially follow the same principles as the phenomenon seen in other conducting materials, such as thin metal films and semiconductors [58, 59].

In comparing the OM and TEM images, we again see that the features appearing in the OM images also appear in the TEM images. However, the use of TEM allows for closer study of the pore-like structures appearing on the surface of the undoped films, as shown in Figure 25. Now it can be seen that what appeared to be pore-like structures in the AFM and OM images are, in actuality, possible phase separation domains.

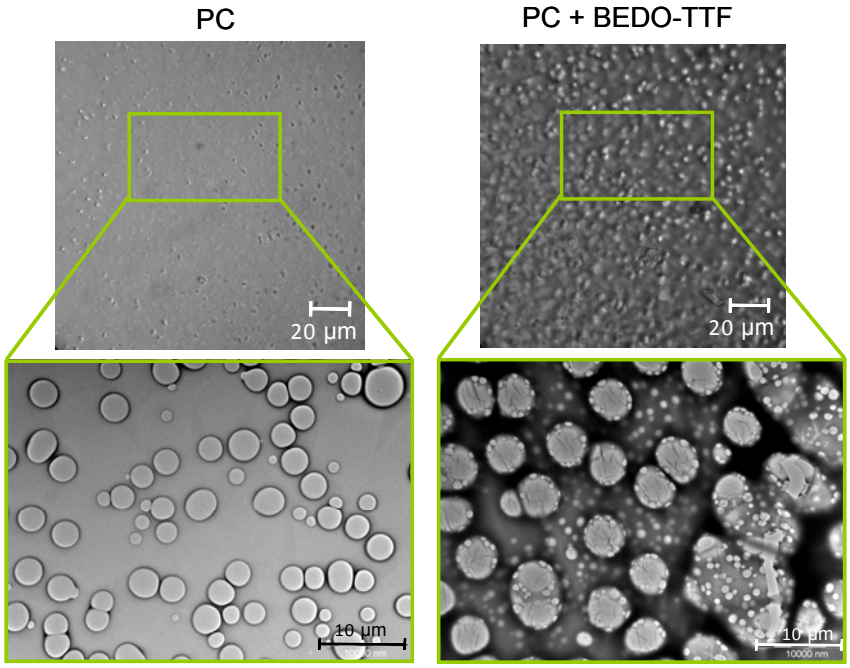

Figure 26: OM and TEM Images of the Polycarbonate and Polycarbonate/BEDO-TTF Films. The upper row of images are taken using the OM at 400x, and the lower two images were taken on the TEM at a magnification of 2.2kx and 100 kV. Shown here are higher magnification images of the phase separation phenomena taking place in the undoped films. In the composite film, small subdomains are observed.

In the case of the polycarbonate film, show a wide range of sizes from about 1 µm to roughly 4 µm. These phase separation domains remain in evidence in the polycarbonate/ BEDO-TTF film, and their size increases slightly to an average of about 5 µm.

The domains in the film containing the BEDO-TTF dye also exhibit the formation of small subdomains within the larger ones, as well as the formation of larger domains due to the fusion of several smaller domains.

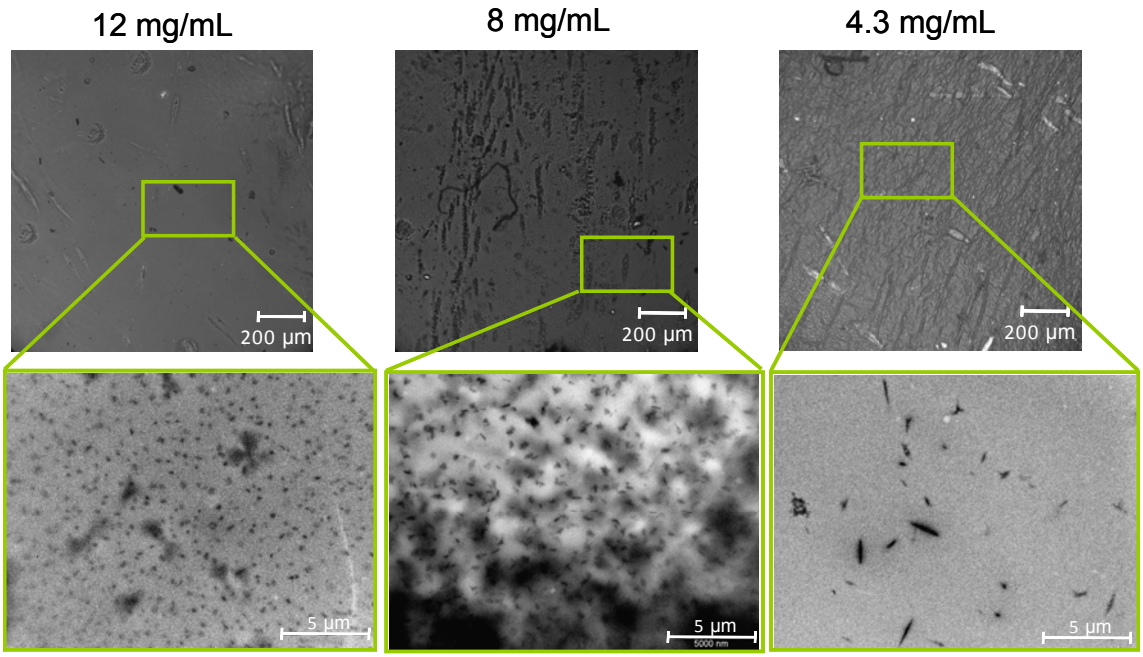

Figure 27: OM and TEM Images of the Films Doped in the Three Different Iodine Solutions. The upper row of images was taken using the OM at 100x, and the lower two images were taken on the TEM at a magnification of 4.4kx and 60 kV. Presented here are images that depict the change that takes place on exposure to iodine: the phase separation effects disappear and dark iodine deposits appear in the TEM images, and the OM images show increasing surface roughness, as in the data calculated from the AFM scans and presented in Figure 25.

These phase separation domains disappear once the iodine is added. This is demonstrated by the images prepared in Figure 27. In the upper row of images in the figure, OM images of the films are shown, and in the lower row, TEM images of the same films are displayed. These images demonstrate that as the iodine loading on the film surface increases, the number of iodine deposits on the film decreases, and the size of the

deposits increases, going from about 0.5 um in the case of the 12 mg/mL doped film to as large as 1.5 um in the 4.3 mg/mL doped film.

5.3. FTIR Analyses and Their Correlation with Imaging Results

FTIR analyses were conducted on the purified and unpurified neat polycarbonate films, the polycarbonate/BEDO-TTF films, and the doped films in transmission. The results were compared and will be discussed as follows: The peak finder algorithm included in the Thermo software (Omnic) was used to guide the placement of the peaks in the spectra that are referred to in this section. Let us begin with the neat polycarbonate spectrum that was taken as a control. The absorbance peaks exhibited by this film are given in Figure 28. It should be noted that the spectrum presented in Figure 28 is of the unpurified polycarbonate used for the experiments done with method 1.

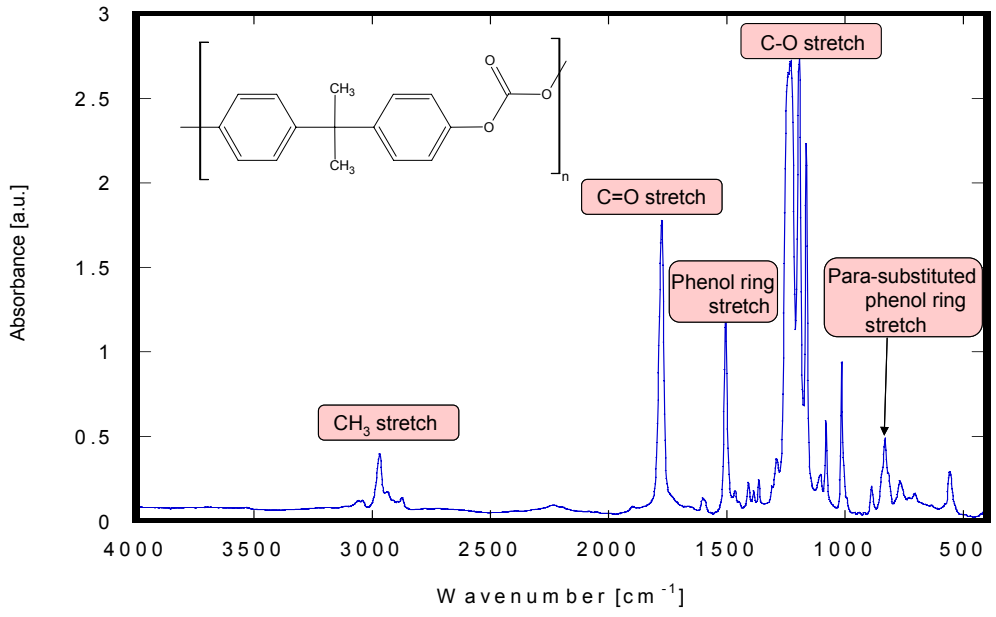

Figure 28: FTIR Spectrum of Unpurified Neat Polycarbonate. The peaks corresponding to the monomeric functional groups are labeled. The structure of the polycarbonate monomer is given in the upper left corner for reference.

All of the functional groups that make up the molecule are represented. The peaks in the spectrum correspond to those expected from a polymer with the structure shown in the upper left hand corner of Figure 28.

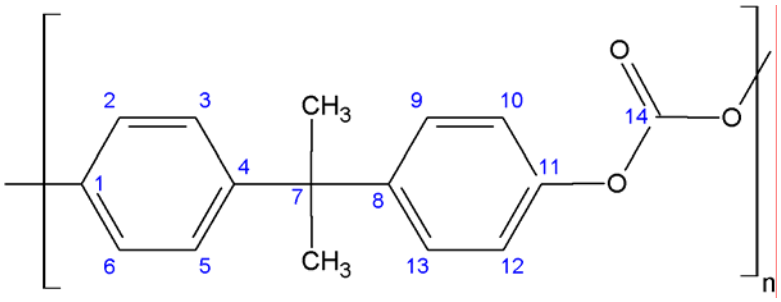

Figure 29: Numbered Structure of Bisphenol-A Polycarbonate. The carbons of the polymer backbone are numbered for easier identification in the discussion.

The two methyl groups bonded to carbon atom seven and the hydrogen atoms bonded to the carbons in the two phenol rings generate the first peak in the spectrum, which appears at 2969 cm^{-1}. Similarly, the oxygen atom double bonded to carbon atom number 14 resonates at about 1776 cm^{-1}, generating the signature carbonyl peak in the spectrum. At 1506 cm^{-1}, the resonance frequency of the two phenol rings is reached. Several very strong peaks appear between 1290 and 1015 cm^{-1}. These are a result of the different vibrational modes of the oxygen atoms bonded to carbon atom fourteen. The carbon-oxygen stretch typically appears in two or more bands in the 1300 to 1000 cm^{-1} range. The last peak of interest that appears in this spectrum appears at 831 cm^{-1}. This peak is attributed to the presence of para-substituted phenol rings in the backbone of the polycarbonate polymer.

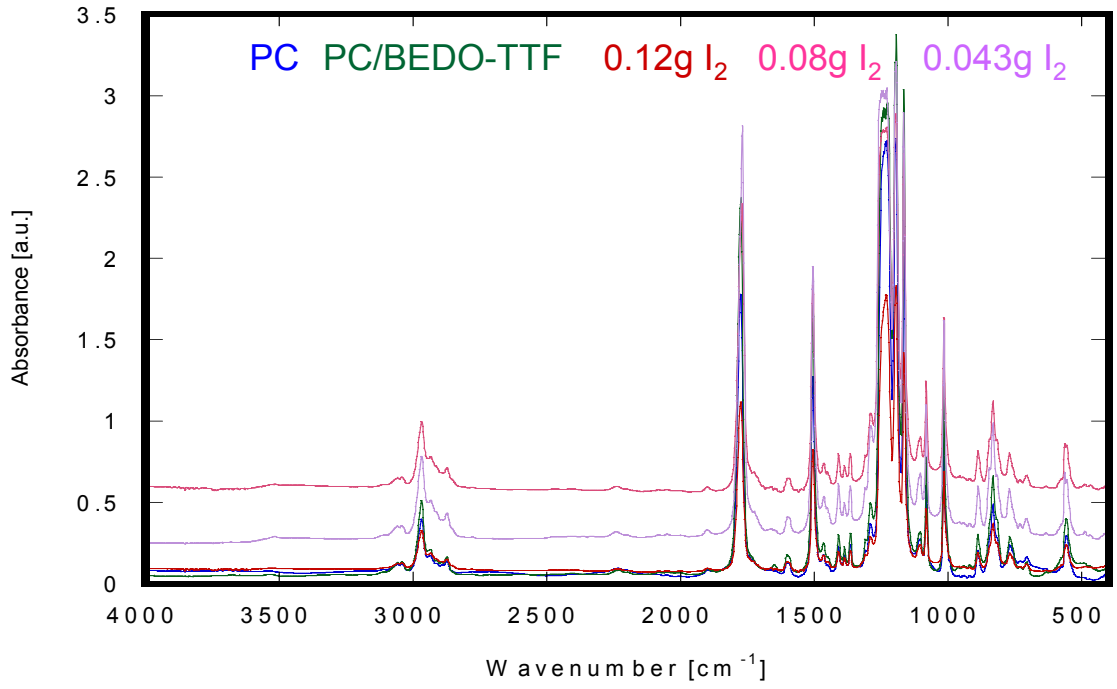

Figure 30: FTIR Spectra of the Control Films and Doped Films for Method 1. No easily observable peaks are seen appearing or disappearing. There is a peak shift occurring in the carbonyl peak and a shoulder is appearing in the para-substitution peak.

In Figure 30, the spectra for all of the doped and undoped films are plotted. It can be easily seen that there are no obvious changes. No easily observable peaks are seen to be appearing or disappearing. The two regions of the spectra shown in Figure 30 that will be further analyzed are those encompassing the carbonyl and para-substitution regions, as labeled in Figure 28. These two regions correspond to fundamental vibrations associated with the bonds of the carbons numbered 1, 4, 8, 11, and 14.

The carbonyl region of the spectra is plotted in Figure 31. At a glance it is apparent that the addition of the BEDO-TTF dye has not caused any changes to take place other than an increase in the intensity of the peak. This simply tells us that there are more carbonyl bonds available in the sample to absorb IR light. Since no carbonyl bonds exist in the BEDO-TTF dye, reason dictates that there must be more carbonyl bonds

present due to the presence of more polycarbonate molecules. This, in turn, leads to the conclusion that this increase in intensity is most probably due to a slight increase in the film thickness from the neat polycarbonate film to the polycarbonate/BEDO-TTF composite film. Doping for two minutes in the 12 mg/mL solution results in a peak shift of three reciprocal centimeters. As the iodine loading increases, however, the carbonyl peak does undergo a slight shift. The peak after doping for four minutes in the 8 mg/mL solution reveals a shift to the right of about 6 reciprocal centimeters. This shift increases again in the case of the 4.3 mg/mL doped film, to 9 reciprocal centimeters.

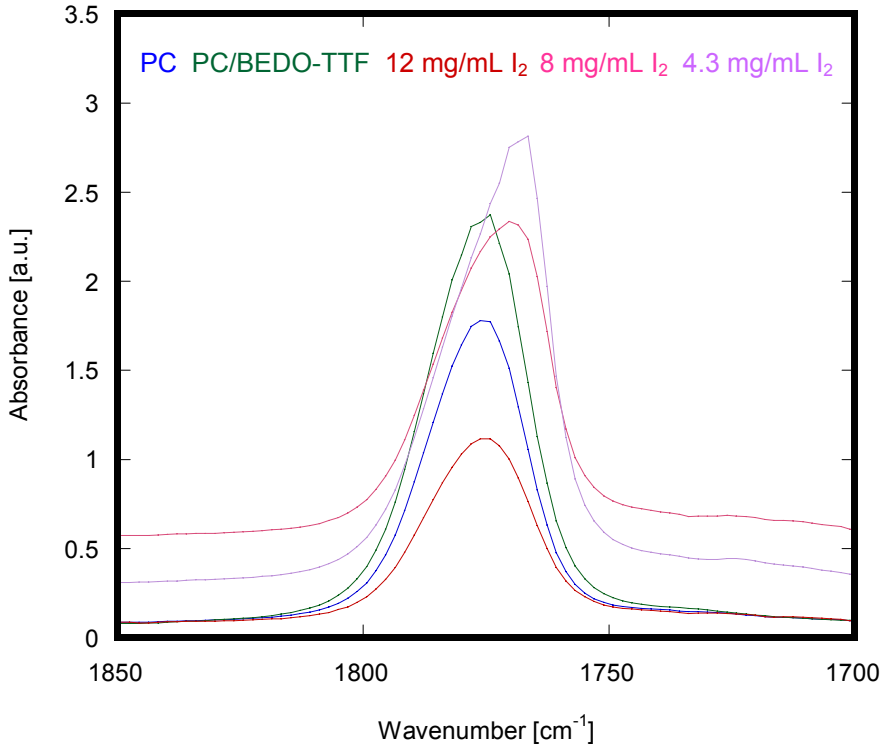

Figure 31: Expanded View of the Carbonyl Region of the Spectra Shown in Figure 30. There is a negligible peak shift on the addition of the BEDO-TTF dye to the neat polycarbonate film. As the iodine loading of the film increases, the peak shift also increases, showing that the addition of the iodine causes an interaction to take place between the carbonyl bond of the monomer and the iodine complexes formed.

This increase with the iodine loading on the film surface seems to indicate that the formation of the BEDO-TTF/iodine complex results in a weak interaction between the complex and the carbonyl groups present in the polycarbonate matrix. The increases in the peak shifts observed correspond to the increases in film conductivity, as well, which implies that the interaction between the polycarbonate and the BEDO-TTF/iodine complex could potentially have an impact on how well the films conduct electricity.

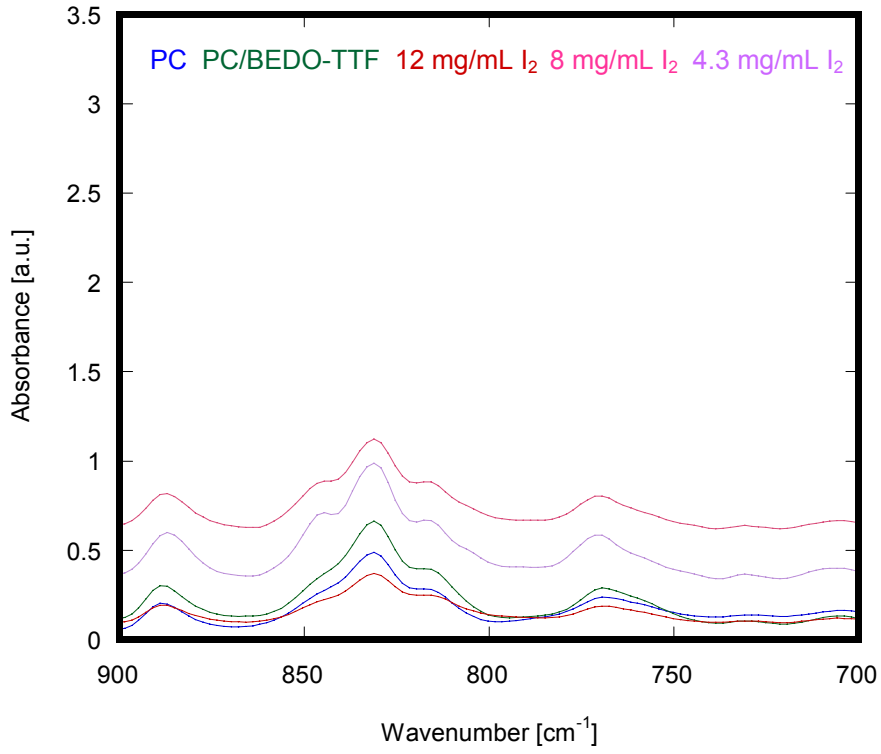

Figure 32: Expanded View of the Spectral Peak From Figure 30 Which is Attributed to the Resonance Frequency of the Para-Substituted Phenol Rings. The peak in question appears between 800 and 865 cm^{-1}. As in the case of the carbonyl peak, there is a negligible peak shift on the addition of the BEDO-TTF dye to the neat polycarbonate film, and as the iodine loading of the film increases, the peak shift also increases, showing that the addition of the iodine causes an interaction to take place between the carbonyl bond of the monomer and the iodine complexes formed.

The expanded view of the para-substitution region of the spectra presented in Figure 30, shown here in Figure 32, shows a progression just as the carbonyl region does. The difference between the two regions is that in the carbonyl region, there was a peak

shift, whereas in the para-substituted region there is a new peak appearing. The shoulder appearing on the left side of the para-substitution peak grows more pronounced as the iodine loading on the film surface increases. This peak is not present in the spectra of the polycarbonate or the polycarbonate/BEDO-TTF films, but appears after the films have been exposed to the iodine solutions used to vapor dope the film surfaces. The appearance of this peak is believed to be due to the formation of the BEDO-TTF-iodine complex after exposure of the film to the iodine solution [60, 61].

A variety of differences are visible when the spectra taken of the films fabricated using method 1 are compared with those of the films made using method 2. The superimposed spectra of the polycarbonate and polycarbonate/BEDO-TTF films are shown in Figure 33 for comparison. Some differences are apparent that were not seen when making films with he unpurified polycarbonate.

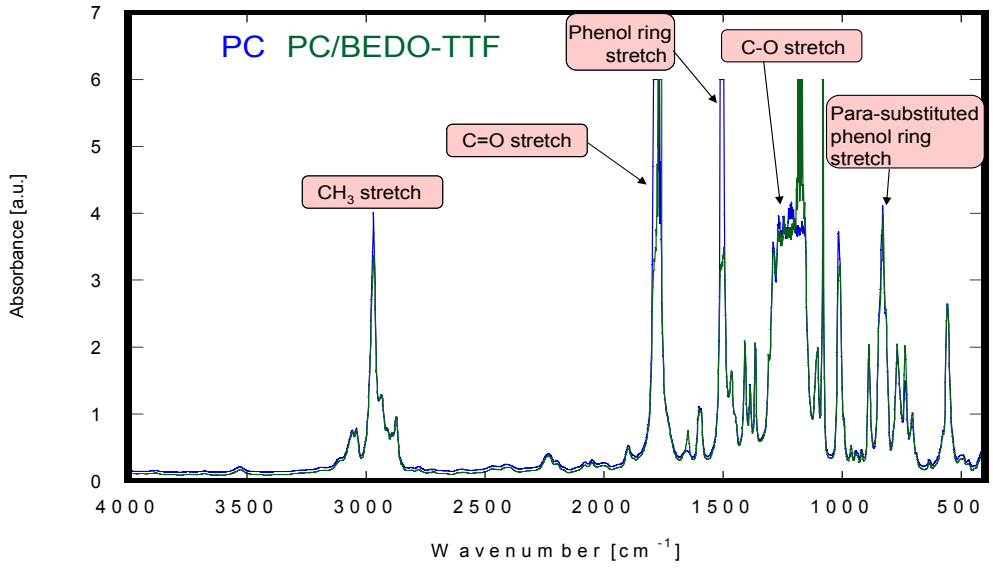

Figure 33: FTIR Spectra of the Polycarbonate and Polycarbonate/BEDO-TTF Films. Shown here are the spectra of the control films prepared using method 2. In method 2, purified polycarbonate resin is used as the matrix for all films. As previously, the peaks corresponding to the functional groups of the molecules present are labeled. Several clear differences are evident between this spectrum and that of the films made using method 1. The carbonyl peak now shows a clear shift on the addition of the dye, as does the para-substitution peak. There is also a new peak appearing between 1200 and 1150 cm^{-1} as a result of the C-S bonds within the dye.

When the spectra of the doped films are superimposed on the two spectra just presented, as seen in Figure 34, several regions show difference worthy of further discussion. These include the carbonyl and para-substitution regions, as were noted when method 1 was used, as well as those regions impacted by the addition of the dye, where peaks are visible now that the polycarbonate has been purified.

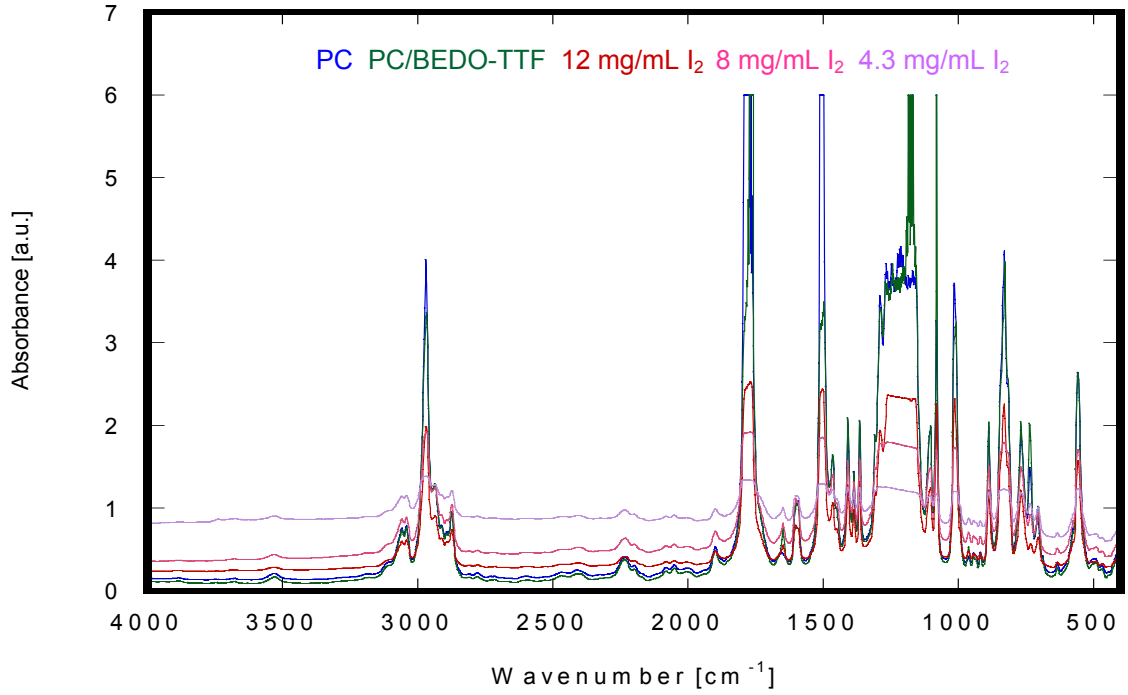

Figure 34: FTIR Spectra of the Films Fabricated Using Method 2. Shown here are the spectra of all the films prepared using method 2. For clarity, the labels of the functional groups are replaced with a legend, since the peaks corresponding to the functional groups have not changed from the previous figure.

The carbonyl region of the films made with method 2 shows a dramatic shift in the spectral peak before and after the addition of the BEDO-TTF dye. An expanded view of this region is plotted in Figure 35. This shift disappears again after the films have been doped, broadening and becoming attenuated. This would seem to indicate that on the

addition of the BEDO-TTF there is a strong interaction between the dye and the carbonyl region of the polycarbonate monomer. The disappearance of the peak shift when the iodine is deposited on the film surface implies that, not only is the interaction between the BEDO-TTF and the carbonyl bond disappearing, but the carbonyl bond itself is being attacked by the iodine. The attenuation of the carbonyl peak as the iodine loading increases suggests that the intensity of the carbonyl peak is dropping due to the disappearance of carbonyl bonds present in the molecule due to the electrophilic nature of the iodine atoms.

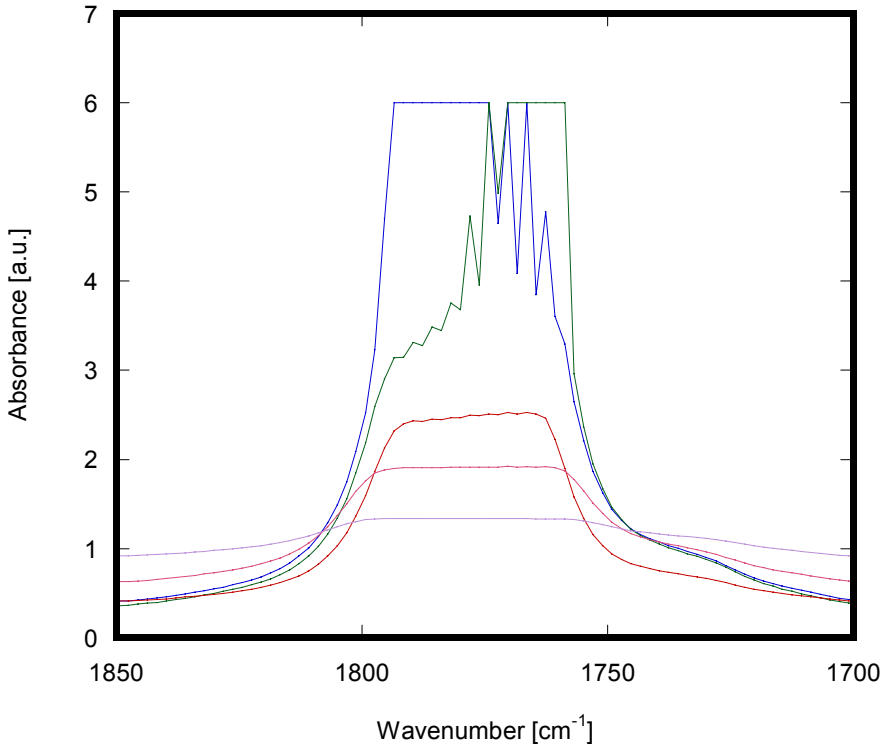

Figure 35: Expanded View of the Carbonyl Region For Spectra of Films Made Using Method 2. This peak corresponds to the stretch associated with carbon 14 of the monomer, as labeled in Figure 29. There is a clear shift on the addition of the BEDO-TTF dye, which is replaced by a sharp attenuation of the peak after exposure to iodine. This indicates an interaction between the carbonyl group of the polycarbonate monomer and the BEDO-TTF dye forms and is then broken after doping. The attenuation of the peak suggests that the iodine is breaking the carbonyl bonds present in the polymer matrix.

The para-substitution region of the films doped with method 2 shows a similar trend to that seen in the carbonyl region. There is a peak shift after the addition of the dye, which subsequently disappears again after the films are exposed to iodine. The para-substitution peak also shows attenuation, like the carbonyl peak, suggesting that the resonating double bonds in the phenol rings of the polycarbonate are being broken by the iodine that is deposited on the film surface. This seems to indicate that, before the purification of the polycarbonate, the iodine was forming complexes with the dye and the impurities in the film. After the purification, the sharp attenuation of the peaks indicates that the iodine is breaking bonds within the polycarbonate monomers due to a decrease in the number of bonds to attack in the impurities.

It is possible that these interactions between the iodine and the polycarbonate could have some impact on the physical characteristics of the polycarbonate film. Further study is needed to determine what effect, if any, the deposition of the iodine has on the structural properties of the polycarbonate.

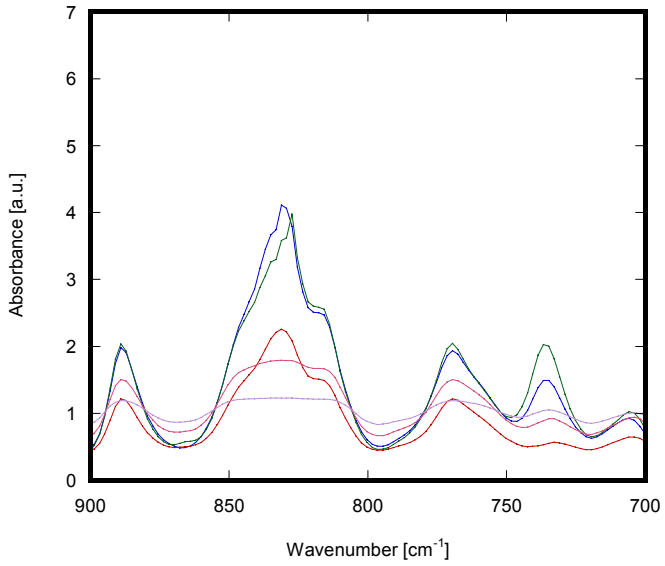

Figure 36: Expanded View of the Para-Substitution Peak Seen in the Spectra of Films Prepared Using Method 2. The peak in question appears between 800 and 865 cm-1. This peak corresponds to the stretch associated with carbon 1, 4, 8, and 11 of the monomer, as labeled in Figure 29.

There are several other regions of the spectra generated by the films made using method 2, however: those containing peaks generated by the BEDO-TTF dye. For example, the first peak that appears as a result of the addition of the dye, and the subtlest, shows up at 1648 cm^{-1}. This peak can be attributed to a stretch that takes place in the five-membered rings within the dye. An expanded view of the region surrounding this peak is shown in Figure 37.

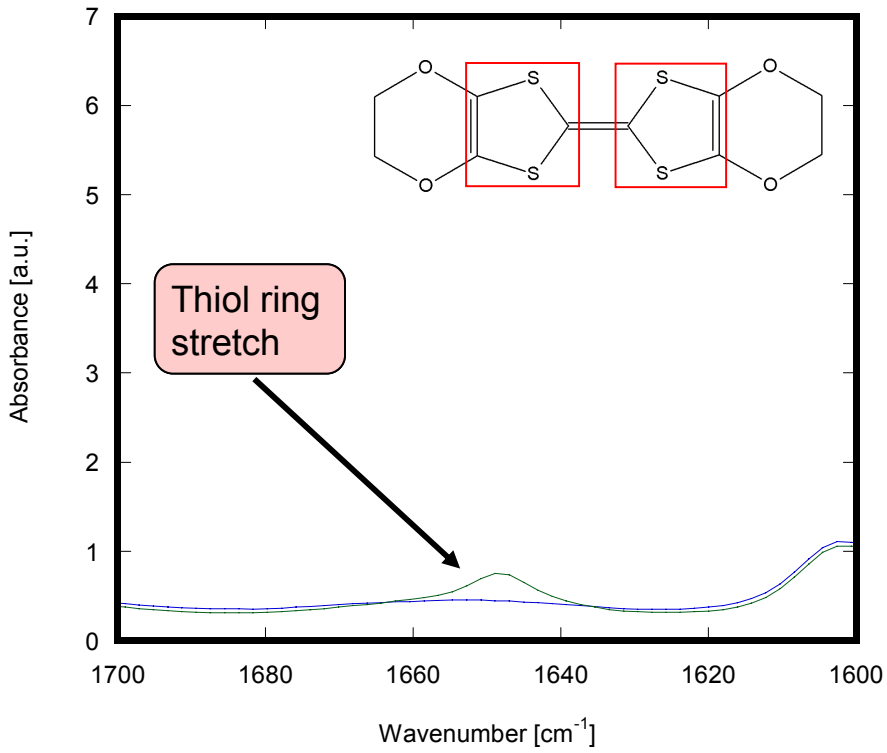

Figure 37: Expanded View of the Region of the Spectrum Surrounding the Thiol Ring Stretch Due to the BEDO-TTF Dye. The structure of the dye is shown in the upper right corner, for reference, and the rings causing the spectral peak have been highlighted with a red box.

Another region of interest is that of the symmetric C-O stretch. This can be seen in Figure 38. The addition of the BEDO-TTF dye causes a series of peaks due to C-S

stretching to appear in the region previously only attributed to C-O stretching. The intensity of the peak due to the ether stretches present in the film jumps on the addition of the BEDO-TTF dye. This rise in the intensity of the peak is directly attributable to the presence of more ether bonds after the addition of the dye, because the di-substituted six-membered rings in the dye contribute to the intensity of this peak.

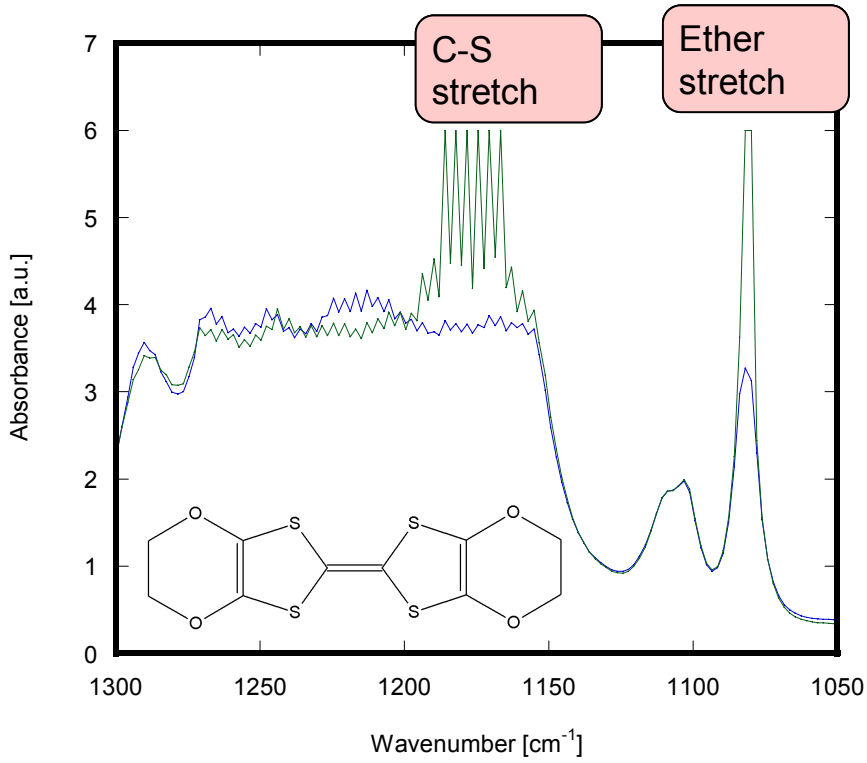

Figure 38: Expanded View of the Spectral Region Surrounding the Thiol (C-S) and Ether (O-C-O) Stretches Due to the BEDO-TTF Dye. The structure of the dye is shown in the lower left corner, for reference.

Chapter Six: Possible Future Trends

Though the future of the field of sensors, biological and otherwise, is very uncertain given the current precarious state of the worldwide economy, the conditions are currently looking relatively good. The number of publications has been consistently increasing in recent years, particularly in the last three to five years, and shows no signs of slowing.

Of course, the number of papers being published is not the only criterion on which an analysis should be based. The complimentary aspect to that of academic papers published in journals is naturally that of industry, and the actual production of the devices so painstakingly developed by researchers. So any prediction made must account for the fact that after the research and development are over, and production begins, it is the combination of simplicity of operation, speed, accuracy, and price that will be the keys to a successful production run. It is, after all, usually the sensor that can strike the best balance between these characteristics that will gain a larger market share than the others in the end.

Chapter Seven: Summary

The selection of materials for modern gas sensors is based upon their physical and chemical characteristics. Two qualities in particularly high demand are transparency and conductivity. This is due to the fact that, while polymer gas sensors, in which the polymer acts as a solid electrolyte, have been developed, these types of sensors are opaque. As a direct consequence of their opacity, the potential for their use in sensors combining conductive polymers with dichromatic materials is limited. To provide a resolution to this dilemma, the development of a method for the production of a transparent conductive polymer film is necessary.

Past research has shown that it is possible to create polymer films containing conductive networks using iodine-doped bisphenol-A polycarbonate films containing bis(ethylenedioxy)-tetrathiafulvalene (BEDO-TTF) dye. The feasibility of the use of these types of films for sensor applications was tested. It is the goal of this researcher to help create a sensor which will identify molecules of explosives in the air, sensitively enough and robustly enough to make the sensor useful in public settings, such as shopping centers and mass transit stations, as a warning of an improvised explosive device (IED).

Polymer sensors can be difficult to fabricate if they are being used in complex applications. However, the sensor whose beginning stages of development are

characterized in this work promises to be easily fabricated once the process has been optimized and all of the components have been added to the system.

Based on the results presented in Chapter Five, given optimization of the conductivity and the transparency, the films fabricated could be used for the design and development of a sensor for the detection of chemical vapors. It was found in this study that:

- FTIR spectra show an interaction between the polycarbonate matrix and the dye-iodine complex when method 1 is used in the fabrication, based on the shifts seen in the carbonyl and para-substitution peaks
- The use of method 2 shows a different interaction, with a peak shift appearing when the dye is added to the neat polycarbonate films, which disappears again after the addition of the iodine, to be replaced with a sharp attenuation of the peaks.
- From FPP measurements, the resistivities of the doped films have been shown to range from 148 Ω-cm in the case of the film with the longest exposure time to 2.82 kΩ-cm in the case of the film with the shortest exposure time.
- The imaging techniques used show a general trend of increasing surface roughness with increasing iodine loading of the films which correlates with increasing conductivity.

Future work to be done on these films would be to optimize the transparency and conductivity of the films to fine tune the fabrication process to produce the best film for application in a vapor sensor sensitive to explosives. The next steps would be to add gold

nanoparticles to the surface of the doped film, and to then optimize the concentration of the gold particles and the conductivity of the films.

References

1. Thorslund S, Larsson, R., Bergquist, J., Nikolajeff, F., Sanchez, J. Biomed Microdevices 2008(10):851-857.

2. Farrar D, West, J. E., Busch-Vishniac, I. J., Yu, S. M. . Scripta Materialia 2008;59(10):1051-1054.

3. Almeida MG, Silveira, C. M., Moura, J. J. G. . Biosensors and Bioelectronics 2007;22(11):2485-2492.

4. Wei Q-B, Luo, Y-L., Zhang, C-H., Fan, L-H., Chen, Y-S. . B-Chemical Sensors and Actuators 2008;134(1):49-56.

5. Adhikari B, Majumdar, S. . Prog. Polym. Sci. 2004;29(7):699-766.

6. Elsenbaumer RL, Pomerantz, M., Marynick, D.S., Sharma, S.C. . 1996.

7. Adhikari B, Majumdar, S. . Prog. Polym. Sci. 2004;29(7):708.

8. Jeszka JK, Tracz, A., Sroczyn´ska, A., Kryszewski, M., Yamochi, H., Horiuchi, S., Saito, G., Ulan´ski. J. Synthetic Metals 1999;106(2):75-83.

9. Chiang CK, Park, Y.W., Heeger, A.J., Shirakawa, H., Louis, E.J., MacDiarmid, A.G. J Chem Phys 1978;69:5098-5104.

10. Shirakawa H, Louis, E.J., MacDiarmid, A.G., Chiang, C.K., Heeger, A.J. . J Chem Soc Chem Comms 1977:578-580.

11. Suzuki T, Yamochi, H., Srdanov, G., K. Hinkelmann, G., Wudl F. J. Am. Chem. Soc. 1989;111 (8):3108-3109.

12. Horiuchi S, Yamochi, H., Saito, G., Sakaguchi, K.-I., Kusunoki, M. . J. Am. Chem. Soc. 1996;118(36):8604.

13. D.L. Lichtenberger RLJ, K. Hinkelmann, T. Suzuki, F. Wudl J. Am. Chem. Soc. 1990;112(9):3302.

14. Golub M, Graja, A., Jó´zwiak K. . Synthetic Metals 2004;144 201-206.

15. Arshak K, Moore, E., Cunniffe, C., Nicholson, M., Arshak A. . Superlattices and Microstructures 2007;42(1-6):479-488.

16. Epifani M, Giannini, C., Tapfer, L., Vasanelli, L. . J. Am. Ceram. Soc. 2000;83(10):2385-2393.

17. Torsi L, Pezzuto, M., Siciliano, P., Rella, R., Sabbatini, L., Valli, L., Zambonin, P.G. . Sensors and Actuators B 1998;48:362-367.

18. Beecroft L. L. O, C. K. Chem. Mater. 1997;9(6):1302.

19. Foss CA, Hornyak, G. L., Stockert, J . A., Martin, C. R. Adv. Mater. 1993;5(2):135.

20. Biswas A, Marton, Z., Kanzow, J., Kruse, J., Zaporojtchenko, V., Faupel, F., Strunskus, T. Nano Letters 2003;3(1):69.

21. Monk DJ, Walt, D. R. . Anal Bioanal Chem. 2004;379:931-945.

22. Pereira FC, et al. Quím. Nova [online] 2006;29(5):1054-1060.

23. Carion Oea. ChemBioChem 2007;8:315 - 322.

24. Cusmà A, et al. Materials Science and Engineering C 2007;27(5-8):1158 - 1161.

25. Lu Y, et al. Bioelectrochemistry 2007;71(2):211 - 216.

26. Tripathi Aea. Anal. Chem. 2007;79(3):1266-1270.

27. Dorozhkin LM, Nefedov, V.A., Sabelnikov, A.G., Sevastjanov, V.G. Sensors and Actuators B 2004;99:568-570.

28. Nefedov VA, Marina V. Polyakova, M.V., Rorer, J., Sabelnikov, A. G., and Kochetkov, K. A. Mendeleev Communications 2007;17:167-169.

29. De G, and Kundu, D. . Chem. Mater. 2001;13(11):4239-4246.

30. Kawaguchi T, Shankaran, D. R., Kim, S. J., Matsumoto, K., Toko, K., Miura, N. Sensors and Actuators B 2008;133:467-472.

31. Martinu L, Biedermann, H., Zemek J. Vacuum 1985;35(4-5):171.

32. Pipino ACR, Silin, V. Chemical Physics Letters 2005;404:361-364.

33. Vörös NM, Patakfalvi, R., Dékány, I. Colloids and Surfaces A 2008;329:205-210.

34. Urbiztondo MA, Pellejero, I., Villarroya, M., Sesé, J, Pina, M.P., Dufour, I., Santamaría, J. . Sensors and Actuators B 2009;137:608-616.

35. Vorotyntsev MA, Vasilyeva, S. V. Advances in Colloid and Interface Science 2008;139:97-149.

36. Sutarlie L, Yang, K.-L. Sensors and Actuators B 2008;134:1000-1004.

37. Nanto H, Yokoi, Y., Mukai, T., Fujioka, J., Kusano, E., Kinbara, A., Douguchi, Y. Materials Science and Engineering C 2000;12(1-2):43-48.

38. Zribi K, Feller, J. F., Elleuch, K., Bourmaud, A., Elleuch, B. Polym. Adv. Technol. 2006 17:727-731.

39. Valmikanathan OP, Ostroverkhova, O., Mulla, I.S., Vijayamohanan K., Atre, S.V. Polymer 2008;49(16):3413-3418.

40. Pavia DL, Lampman, G. M., Kriz, G. S. Introduction to Spectroscopy: A Guide For Students of Organic Chamistry, 3rd Ed. ed. Australia: Thomson Learning, Inc., 2001.

41. Skoog DA, West, D. M. Principles of Instrumental Analysis. New York: Holt, Rinehart and Winston, Inc., 1971.

42. Mongillo J. Nanotechnology 101: Greenwood Press, 2007.

43. Thornton ST, Rex, A. Modern Physics for Scientists and Engineers. Australia: Thomson Learning, Inc., 2002.

44. Laboratory NHMF. Wheatstone Bridge. Magnet Lab, 2008.

45. Nilsson JW, Riedel, S. A. Electric Circuits: Prentice Hall, 2008

46. Hayt Jr. WH, Kemmerly, J. E., Durbin, S. M. Engineering Circuit Analysis, Sixth Edition ed.: Tata McGraw Hill, 2002.

47. Fatikow S. Automated Nanohandling by Microrobots: Springer, 2007.

48. Morris V. J. KAR, Gunning A. P. Atomic Force Microscopy for Biologists: Imperial College Press, 1999.

49. Morita S, Wiesendanger, R., Meyer, E., Eds. Noncontact atomic force microscopy: Springer, 2002.

50. Korenivski V. The van der Pauw Technique. vol. 2009, 2003.

51. van der Pauw LJ. Philips Technical Review 1958/59;20(8):220-224.

52. Bautista K. Thin Film Deposition. The University of Texas at Dallas, 2004.

53. Schroder DK. Semiconductor Material and Device Characterization, 3rd Ed.: Wiley-IEEE, 2006.

54. Tompkins HG, Irene, E. A. Handbook of ellipsometry: Springer Science & Business, 2005.

55. Tompkins HG. A User's Guide to Ellipsometry: Dover Publications, 2006.

56. Cherry RJ. New techniques of optical microscopy and microspectroscopy: CRC Press, 1991.

57. Nickell J, Fischer, J. F. Crime science: methods of forensic detection: University Press of Kentucky, 1998.

58. Ganesan S, Pecht, M. Lead-free Electronics: John Wiley and Sons, 2006.

59. Wissmann P, Finzel, H.-U. Electrical resistivity of thin metal films: Springer, 2007.

60. Graja A, Swietlik, R., Polomska, M., Brau, A., Farges, J.-P. Synthetic Metals 2002;125:319-324.

61. Sommer W, Moldenhauer, J., Schweitzer, D., Heinen, I., Keller, H.J. Synthetic Metals 1995;68:133-139.

Appendices

Appendix A: Conductivity Data

A1. Method 2 Optimizations:

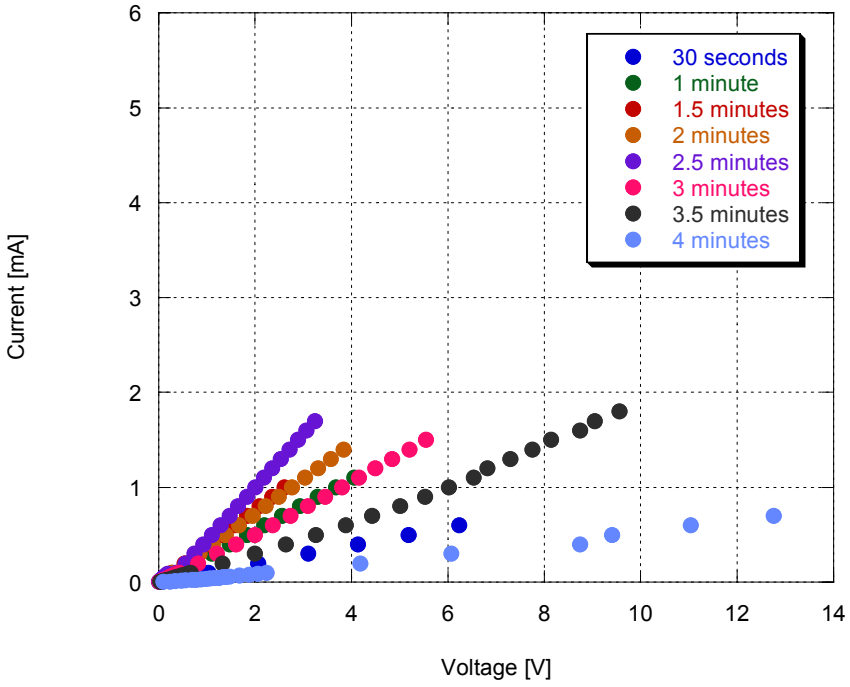

Figure 39: Current-Voltage Data for 12 mg/mL Solution Optimization. Each plotted data set (each line) corresponds to a different exposure time that was tested.

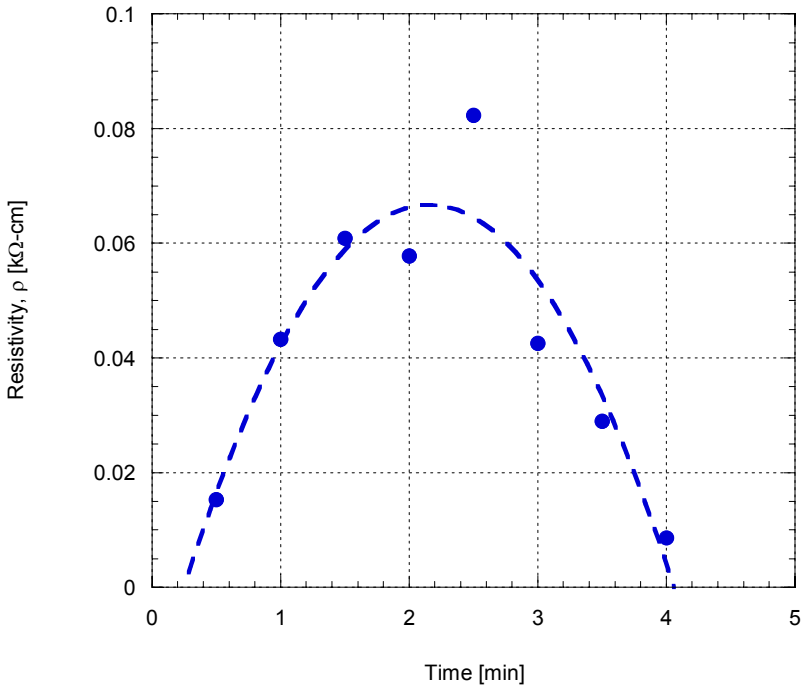

Figure 40: Resistivity versus Exposure Time for 12 mg/mL Solution Optimization. Here the calculated resistivity is plotted against the exposure time.

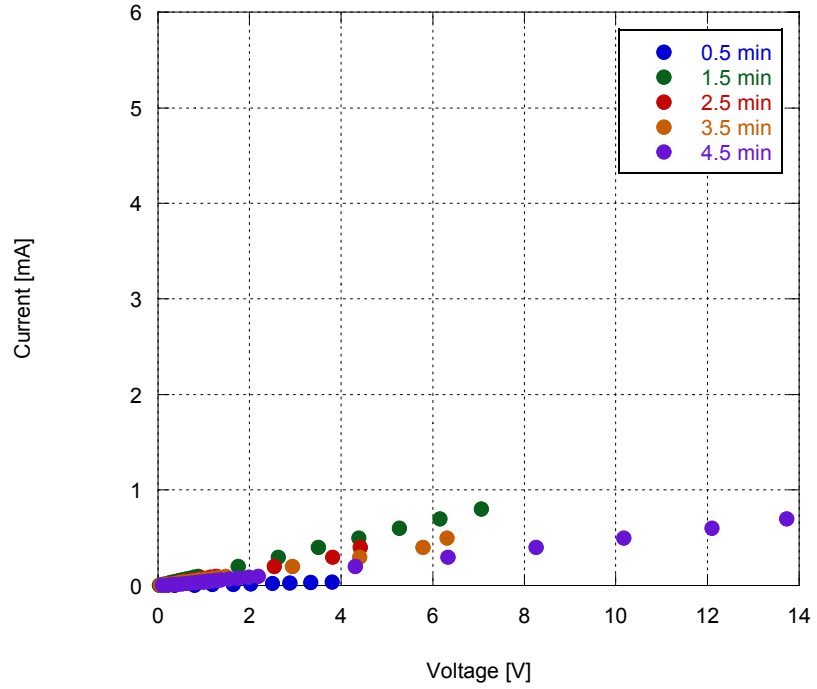

Figure 41: Current-Voltage Data for 8 mg/mL Solution Optimization. Each plotted data set (each line) corresponds to a different exposure time that was tested.

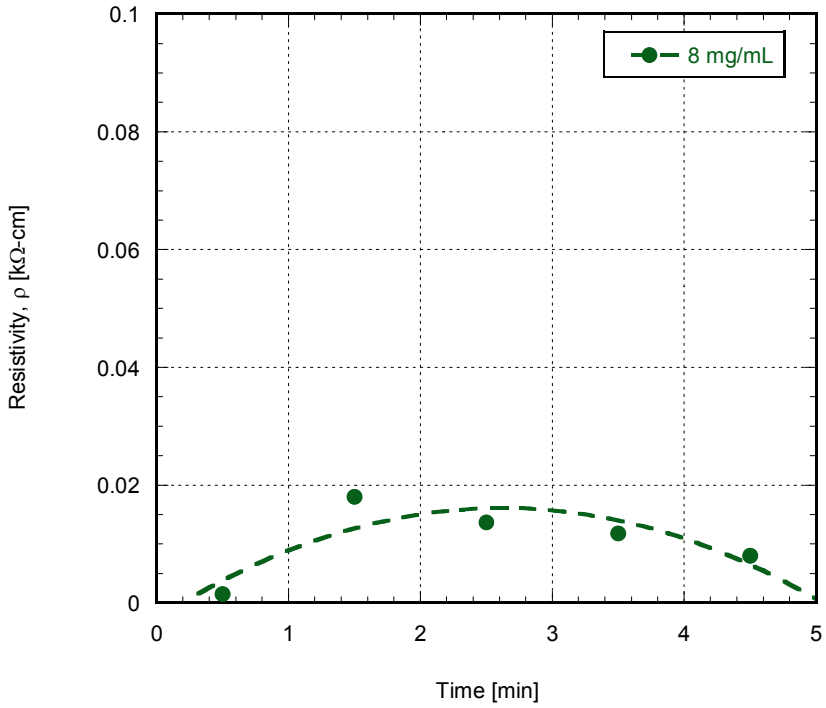

Figure 42: Resistivity versus Exposure Time for 8 mg/mL Solution Optimization. As for the 12 mg/mL optimization, here the calculated resistivity is plotted against the exposure time.

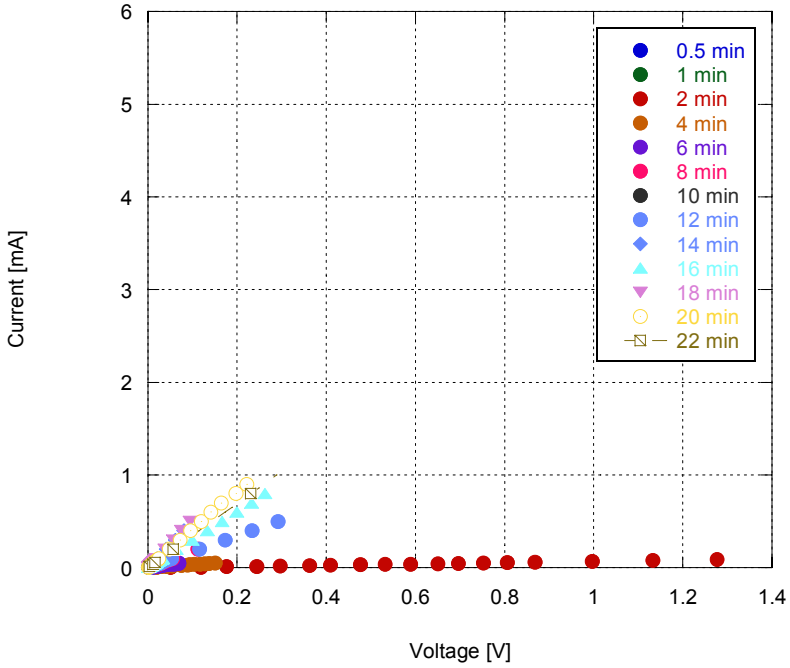

Figure 43: Current-Voltage Data for 4.3 mg/mL Solution Optimization. Each plotted data set (each line) corresponds to a different exposure time that was tested.

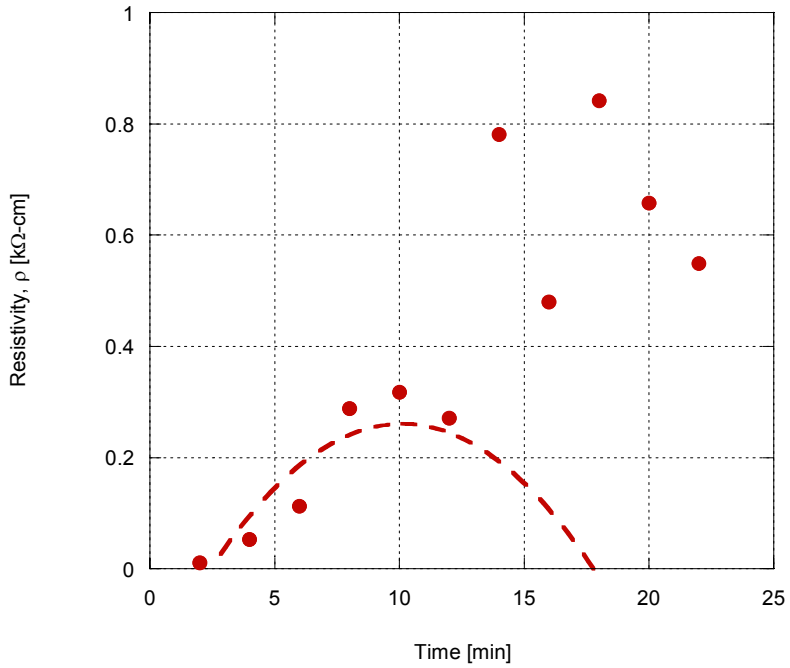

Figure 44: Resistivity versus Exposure Time for 4.3 mg/mL Solution Optimization. As was done for the other concentrations, here the calculated resistivity is plotted against the exposure time. A different profile is seen because, after the film has been exposed for 12 minutes, the effects of the iodine deposition cause the resistivity to increase. The dotted line is fitted to the data points from 0.5 to 12 minutes to demonstrate the trend expected based on the other concentrations.

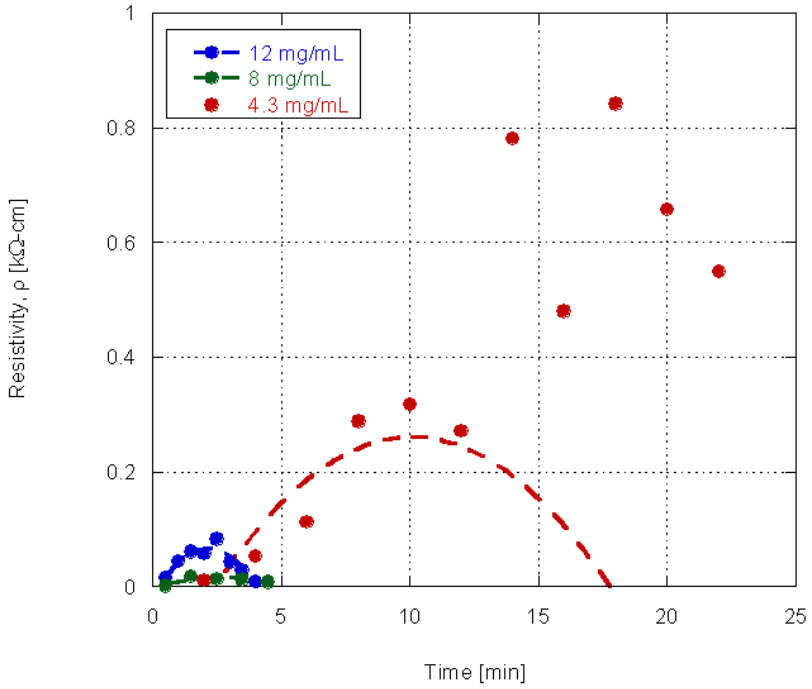

Figure 45: Resistivity versus Exposure Time Optimization For All Three Solutions. Here the calculated resistivity is plotted against the exposure time for all three films for ease of comparison.

A2. Comparing Methods Post-Optimization:

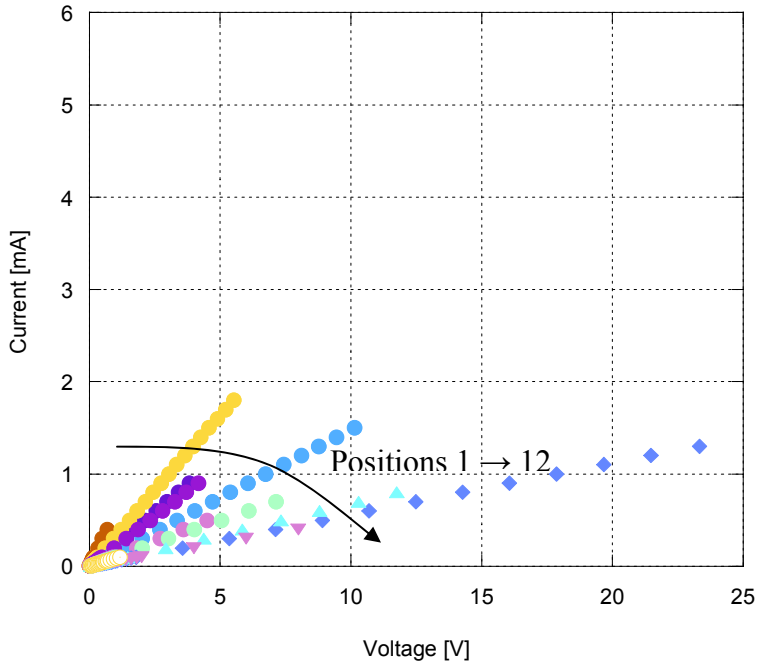

Figure 46: Current-Voltage Data for 8 mg/mL Iodine Solution Concentration Exposed for Four Minutes using Method 1. The current-voltage data for all 12 positions on the film tested is shown.

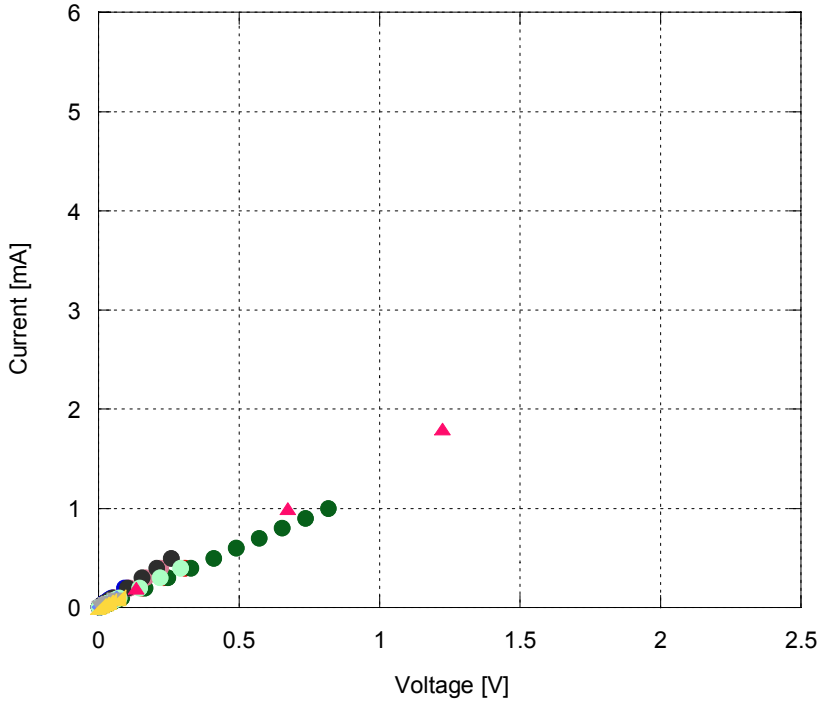

Figure 47: Current-Voltage Data for 8 mg/mL Iodine Solution Concentration Exposed for Four Minutes using Method 2. The current-voltage data for all 12 randomized positions tested is shown.

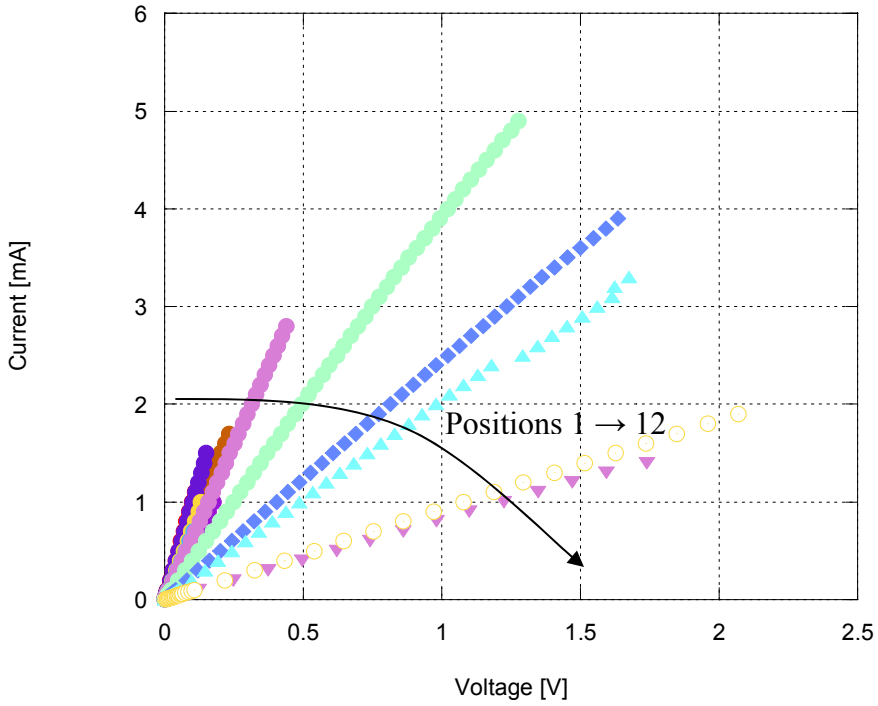

Figure 48: Current-Voltage Data for 4.3 mg/mL Iodine Solution Concentration Exposed for Ten Minutes using Method 1. The current-voltage data for all 12 positions on the film tested is shown.

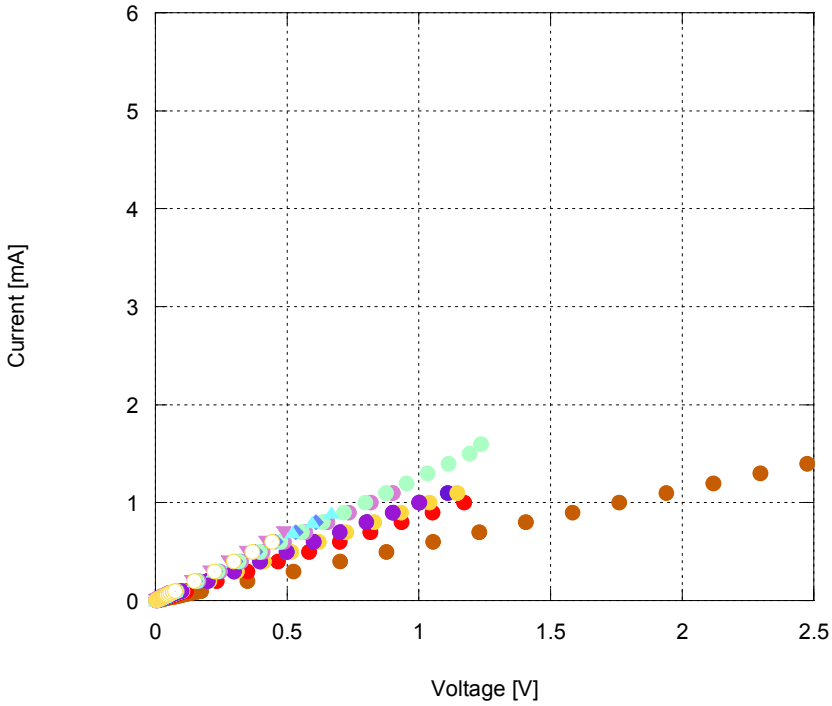

Figure 49: Current-Voltage Data for 4.3 mg/mL Iodine Solution Concentration Exposed for Ten Minutes using Method 2. The current-voltage data for all 12 randomized positions tested is shown.

Appendix B: Optical Microscopy Data

B1. Images of Films Prepared Using Method 1

The images contained herein depict characteristic areas of a given sample which was fabricated using method 1. The surface features seen in the images of the polycarbonate before and after the addition of the BEDO-TTF dye are the postulated phase separation domains. Images of the doped films are taken at the area where the transition from heavily doped to less doped occurs. This is visible as a much darker area of the film where the iodine is more heavily deposited, and a lighter area where less iodine has deposited. The features seen in the 4.3 mg/mL doped film are defects that are caused by the FPP testing. Each of those lighter areas represents the point of contact of one of the four probes.

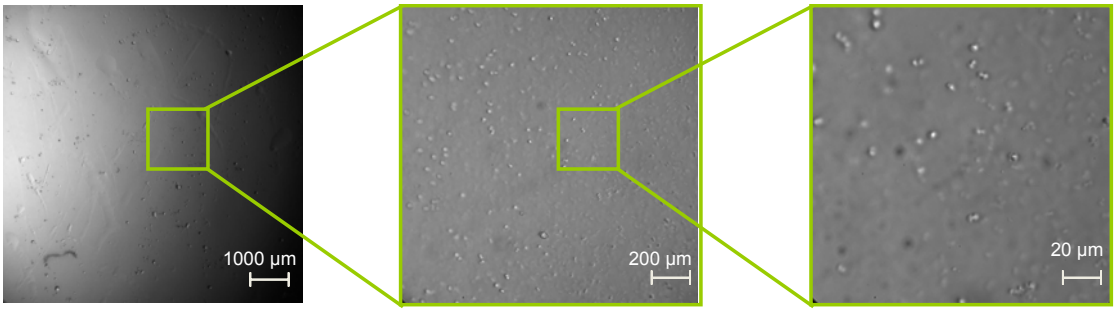

Figure 50: OM Images of Polycarbonate Film at 25x, 100x, and 400x.

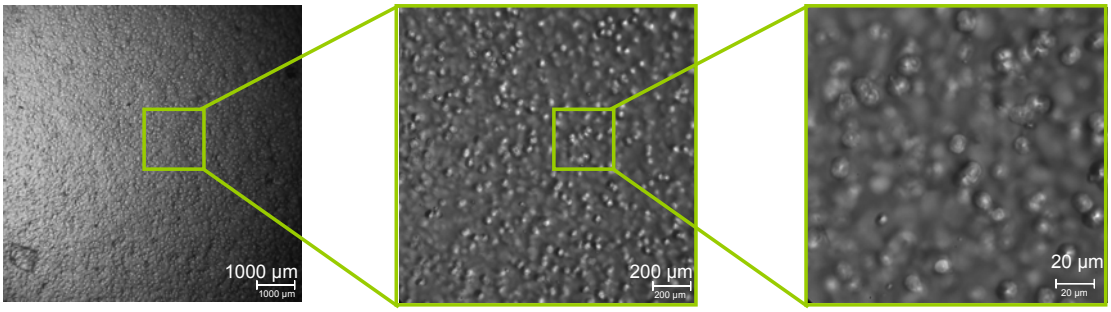

Figure 51: OM Images of Polycarbonate/BEDO-TTF Film at 25x, 100x, and 400x.

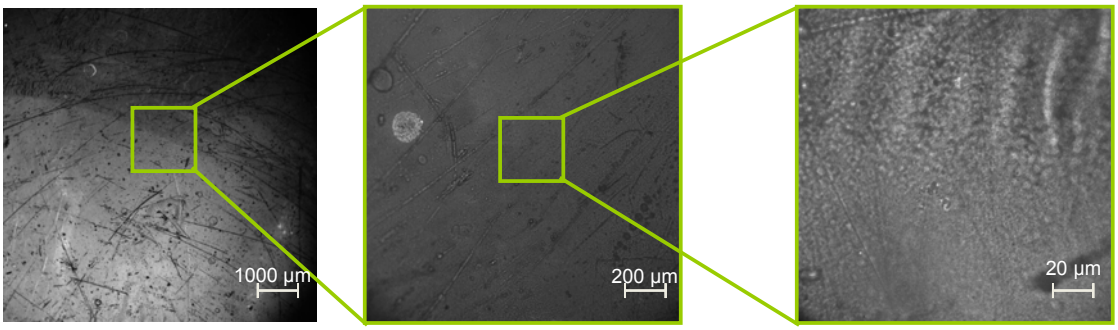

Figure 52: OM Images of 12 mg/mL Doped Film at 25x, 100x, and 400x.

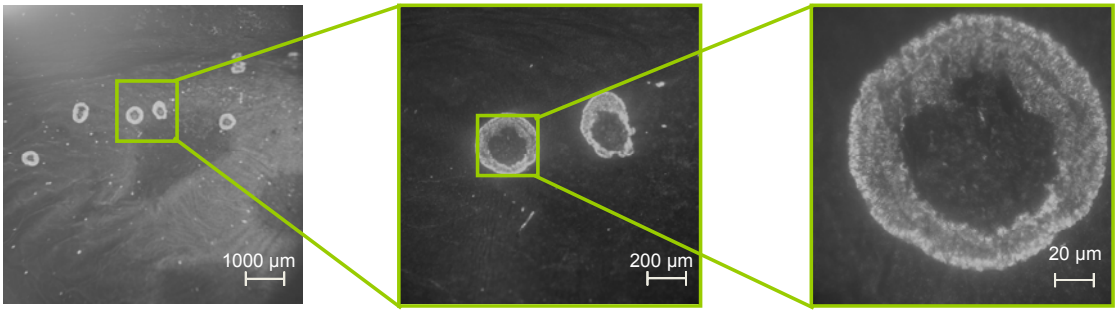

Figure 53: OM Images of 4.3 mg/mL Doped Film at 25x, 100x, and 400x.

B2. Images of Films Prepared Using Method 2

The images contained herein depict characteristic areas of a given sample prepared using method 2. What is emphasized in the images of these films is the homogeneity of the iodine deposition. There was no clear interface between heavily doped and less doped regions as was seen when method 1 was used.

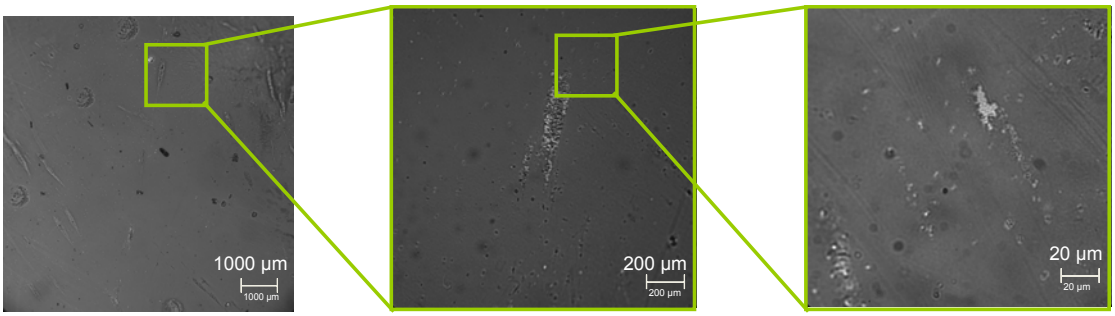

Figure 54: OM Images of 12 mg/mL Doped Film at 25x, 100x, and 400x.

Appendix B, continued

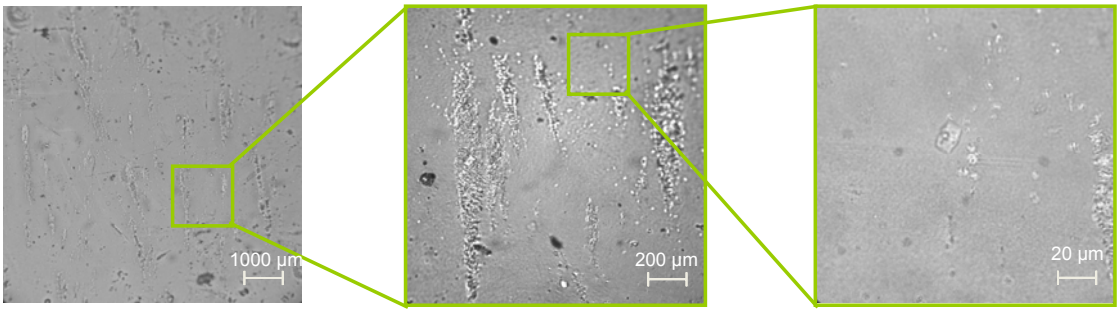

Figure 55: OM Images of 8 mg/mL Doped Film at 25x, 100x, and 400x.

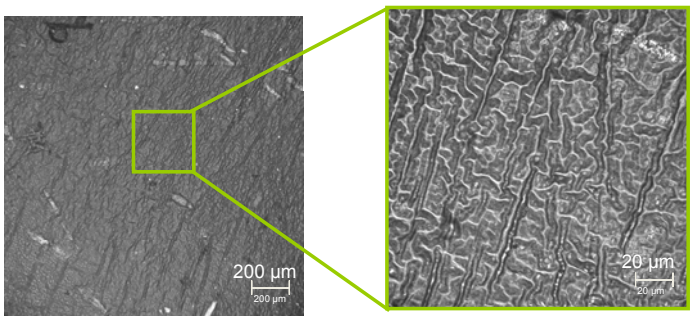

Figure 56: OM Images of 4.3 mg/mL Doped Film at 100x, and 400x.

Appendix C: AFM Imaging

C1. Surface Scans of Films Prepared Using Method 1

10x10 µm surface scans:

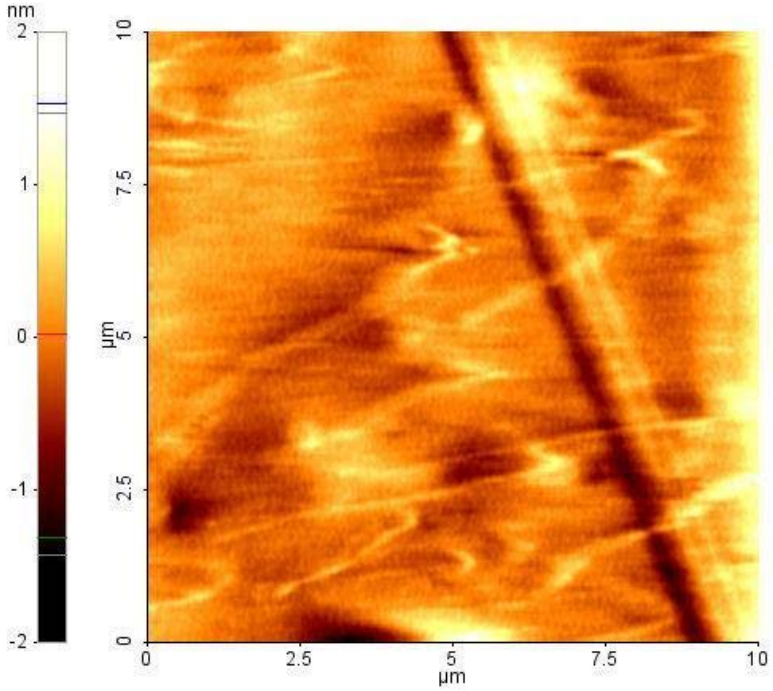

Figure 57: 10 µm Square AFM Scan of Undoped Bis-phenol-a Polycarbonate Film. The slight scratching of the surface is due to the use of FPP testing.

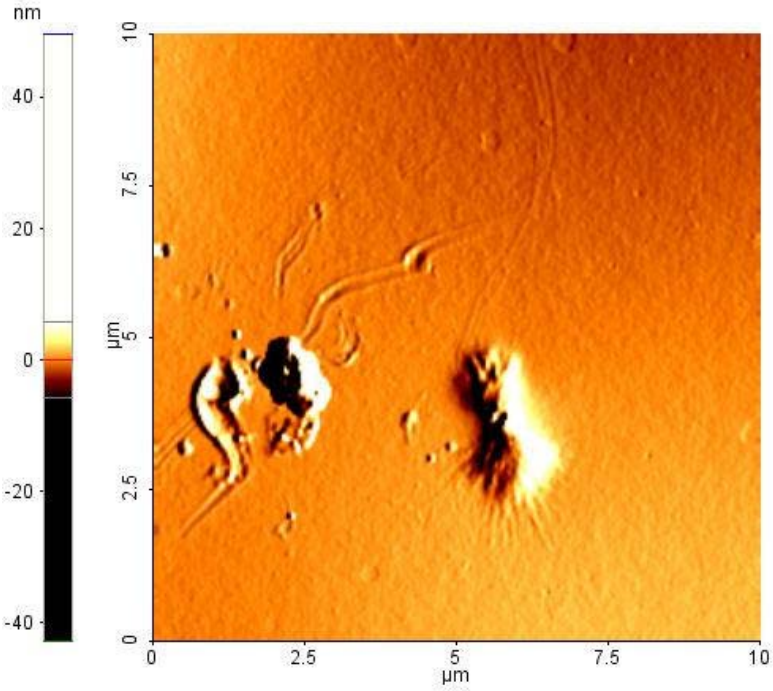

Figure 58: 10 µm Square AFM Scan of Polycarbonate/BEDO-TTF Composite Film. The surface features seen are damage to the film surface due to the use of FPP testing. FPP has been known to leave behind deposits of metal and other foreign materials.

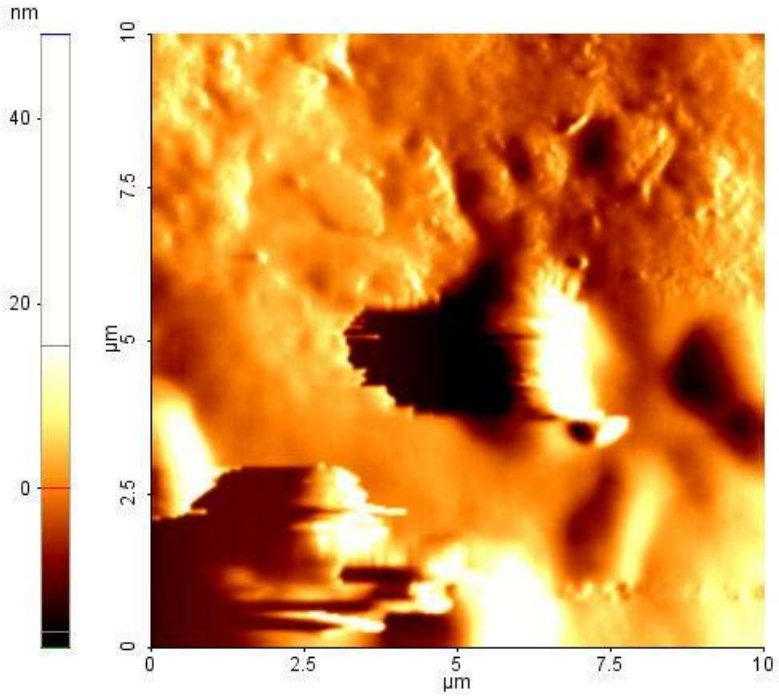

Figure 59: 10 µm Square AFM Scan of 12 mg/mL Doped Film. From this image it can be deduced that the iodine deposited at this exposure time and concentration using method 1 does not tend to form crystallites.

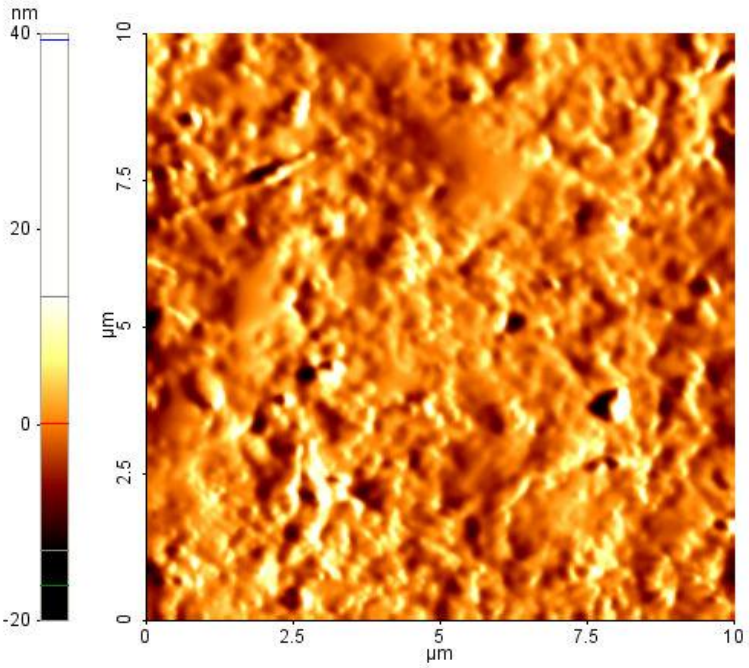

Figure 60: 10 µm Square AFM Scan of Nonconductive Area of 8 mg/mL Doped Film. As in the 12 mg/mL film shown in Figure 59, the iodine deposited at this exposure time and concentration using method 1 does not tend to form crystallites in the nonconducting region. (The nonconducting region forms as a result of the concentration gradient in the iodine in method 1.)

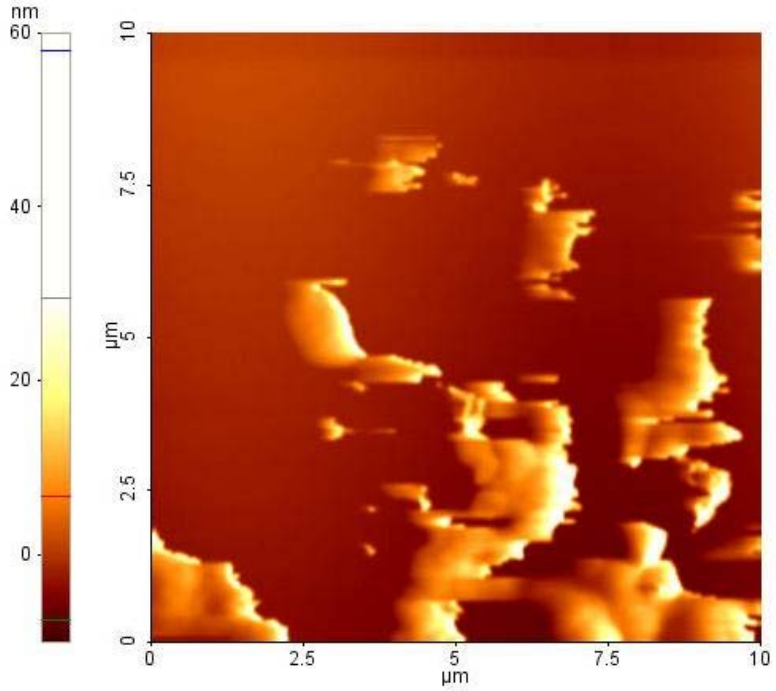

Figure 61: 10 µm Square AFM Scan of Conductive Area of 8 mg/mL Doped Film. Unlike the 12 mg/mL film shown in Figure 59, and the nonconducting area of the same film, the iodine deposited does not tend to form a continuous layer. There is no formation of crystallites, either, due to the effects of the concentration gradient on the deposition of the iodine.

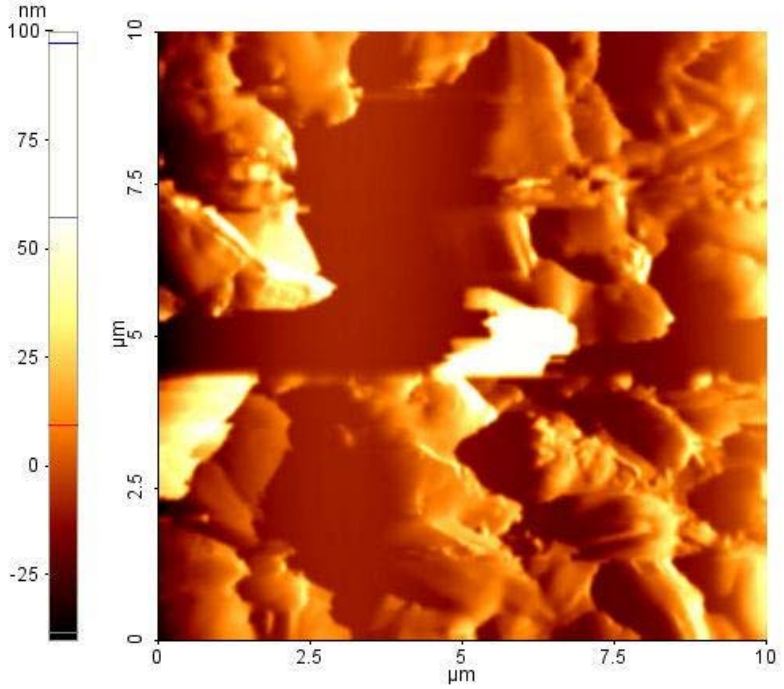

Figure 62: 10 µm Square AFM Scan of the conductive area of the 4.3 mg/mL Doped Film. In the image some crystal-like structures are observed, but no long range order. This is most likely also due to the non-equilibrium effects of doping using method 1.

Appendix C, continued
5x5 µm surface scans:

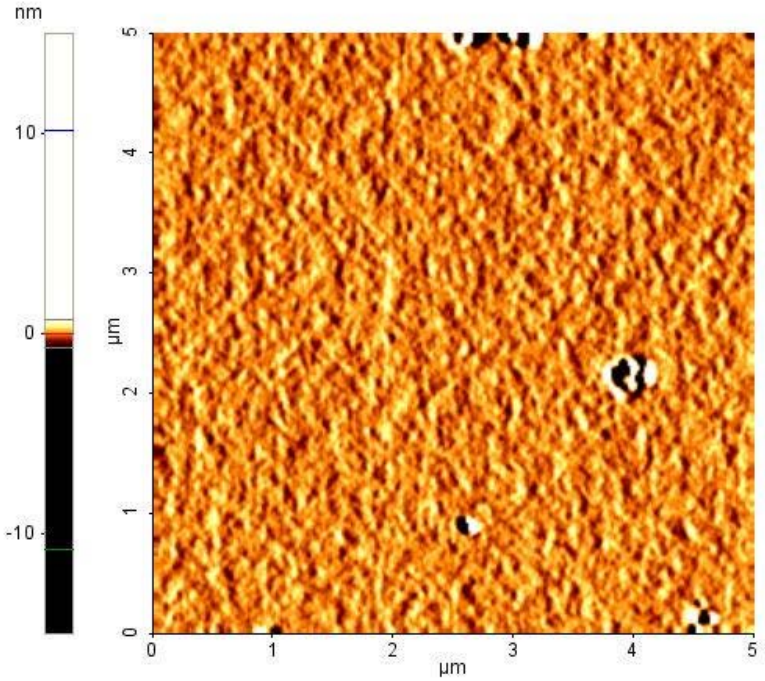

Figure 63: 5 µm Square AFM Scan of the Polycarbonate Control Film. In the image some pore-like structures are observed, similar to what is seen in the OM and TEM images presented in the text.

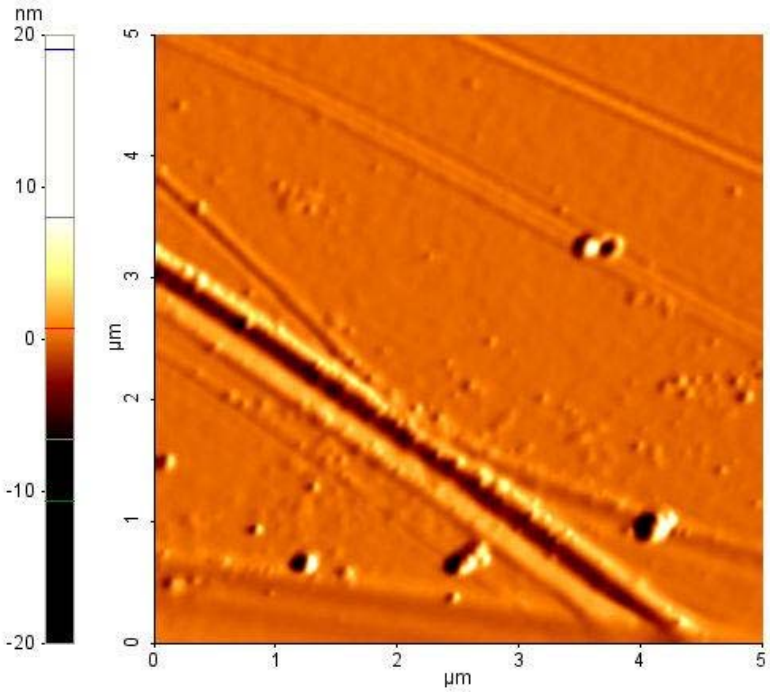

Figure 64: 5 µm Square AFM Scan of the Polycarbonate/BEDO-TTF Control Film. In the image some pore-like structures are observed, similar to what is seen in the OM and TEM images presented in the text. There are also some scratches, due to the use of FPP testing on the control films.

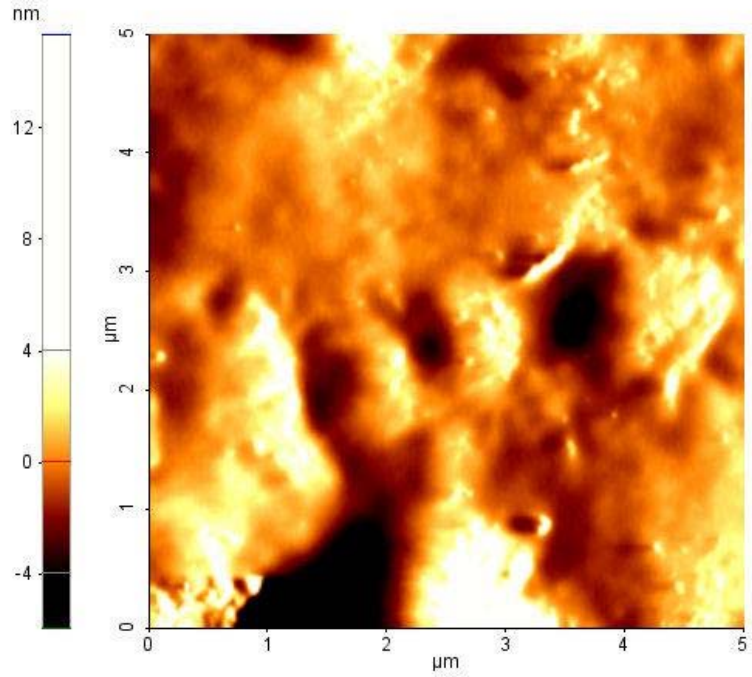

Figure 65: 5 µm Square AFM Scan of 12 mg/mL Doped Film. This image is a more magnified region of that shown in Figure 59.

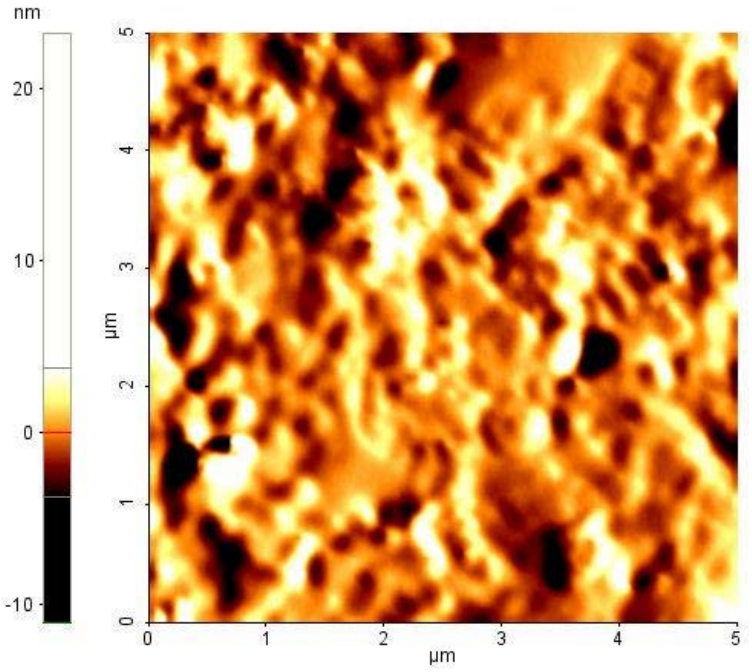

Figure 66: 5 µm Square AFM Scan of the Nonconductive region of the 8 mg/mL Doped Film. This image is a more magnified region of that shown in Figure 60.

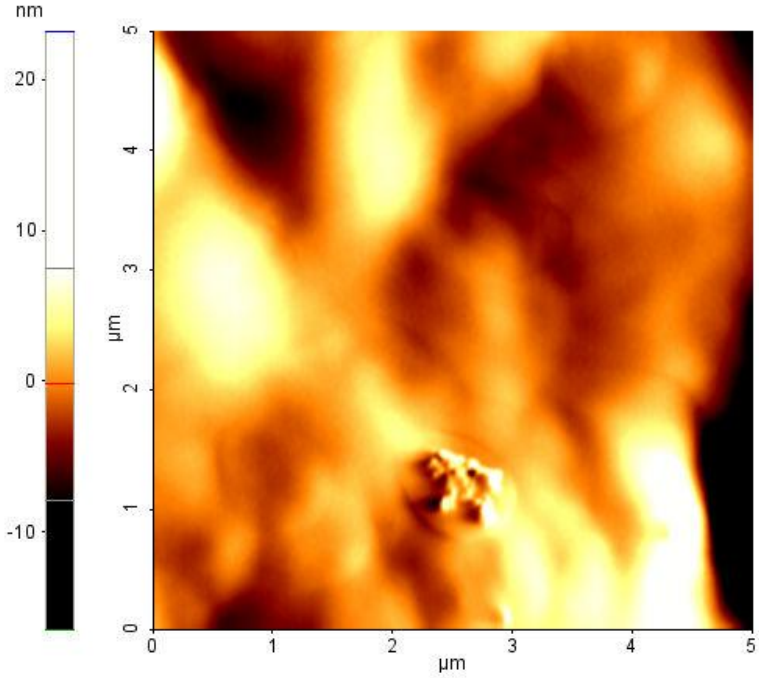

Figure 67: 5 µm Square AFM Scan of the Conductive region of the 8 mg/mL Doped Film. This image is a more magnified region of that shown in Figure 61. The deposit in the lower center of the image is believed to be another instance of damage caused by FPP testing.

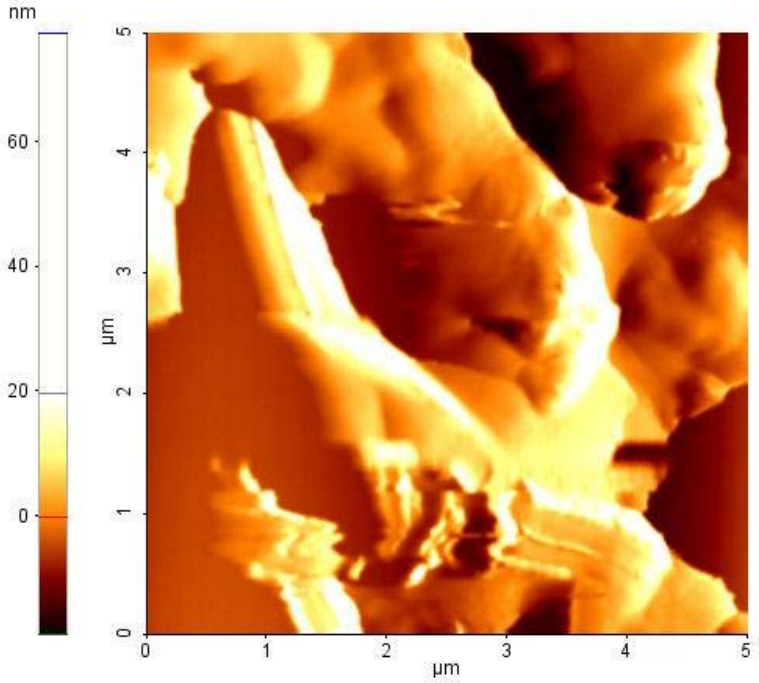

Figure 68: 5 µm Square AFM Scan of the Conductive region of the 4.3 mg/mL Doped Film. This image is a more magnified region of that shown in Figure 62.

Appendix C, continued
2x2 µm surface scans:

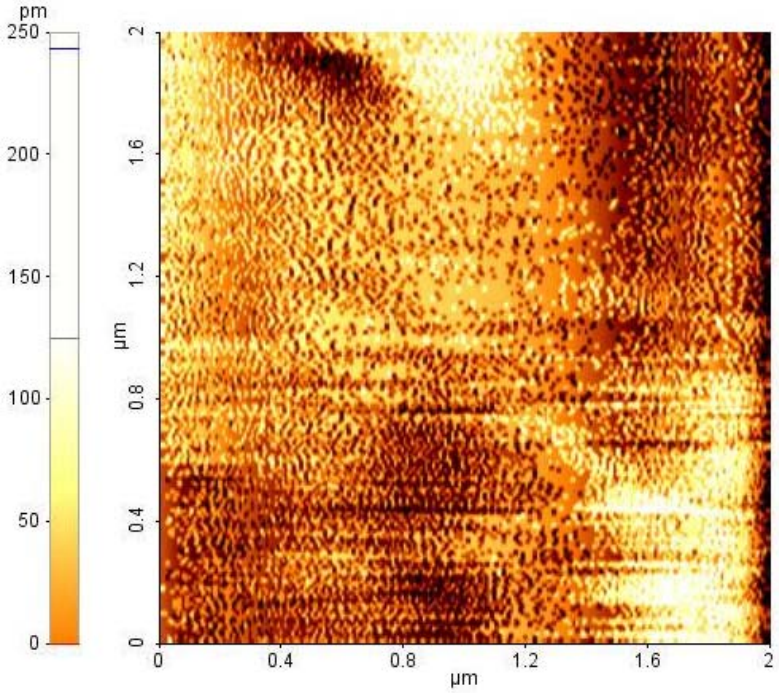

Figure 69: 2 µm Square AFM Scan of the Polycarbonate Control Film. At this scale most of the surface features are no longer easily visible, so no further magnification will be done.

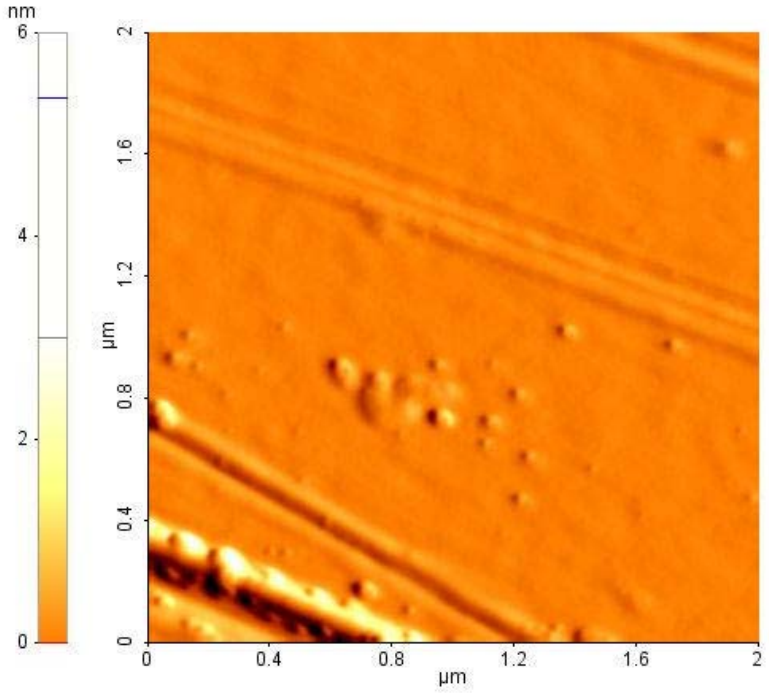

Figure 70: 2 µm Square AFM Scan of the Polycarbonate/BEDO-TTF Control Film. This image is a more magnified region of that shown in Figure 64. The small bumps seen are suspected to be small aggregated of BEDO-TTF dye molecules.

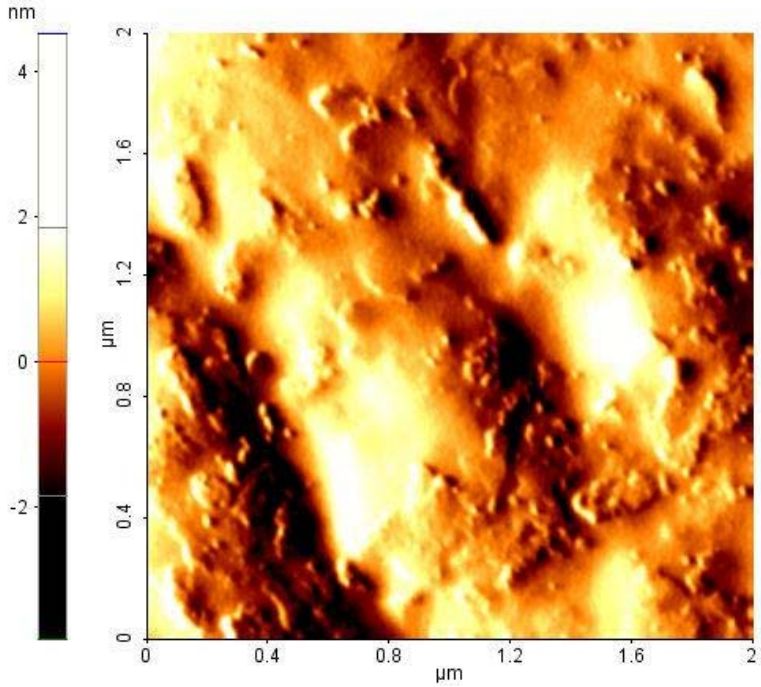

Figure 71: 2 µm Square AFM Scan of the 12 mg/mL Doped Film. This image is a more magnified region of that shown in Figure 65. It can be seen from this scan that the iodine is not forming crystallites, and that the surface is very uneven.

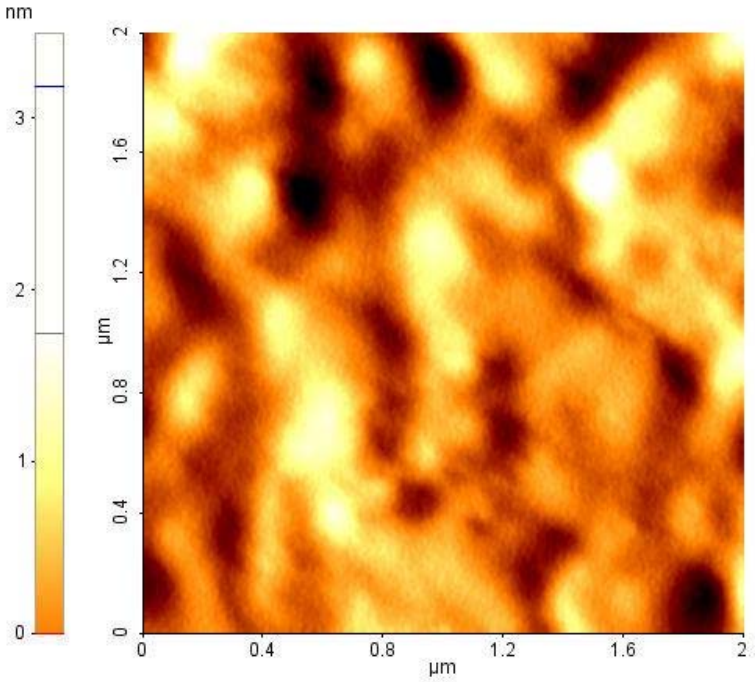

Figure 72: 2 µm Square AFM Scan of the Nonconductive Area of the 8 mg/mL Doped Film. This image is a more magnified region of that shown in Figure 66. This area of the film shows that the entire surface is coated with iodine, but also that it is uneven, and that no crystallites are formed.

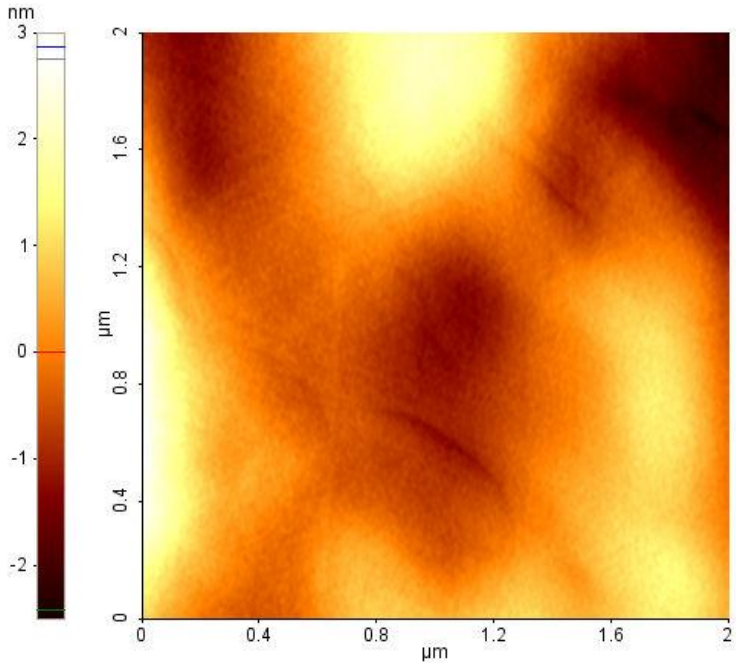

Figure 73: 2 µm Square AFM Scan of the Conductive Area of the 8 mg/mL Doped Film. This image is a more magnified region of that shown in Figure 67. This area of the film shows that, as in the case of the nonconductive area, the entire film surface is coated with iodine, and that the deposits are larger.

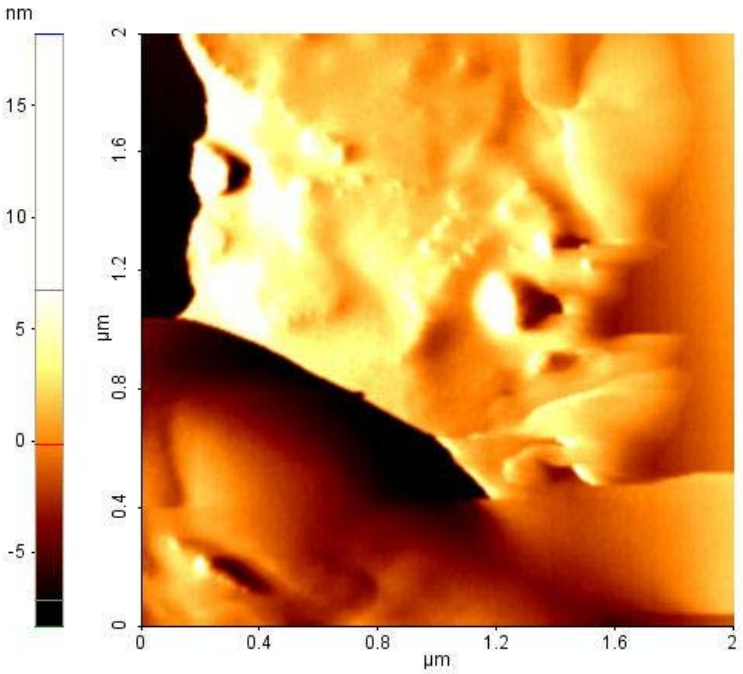

Figure 74: 2 µm Square AFM Scan of the Conductive Area of the 4.3 mg/mL Doped Film. This image is a more magnified region of that shown in Figure 68. This area of the film shows deposits of iodine with more order than in the case of the other two concentrations, but no crystallites.

Appendix C, continued
C2. Surface Scans of Films Prepared Using Method 2
10x10 µm surface scans:

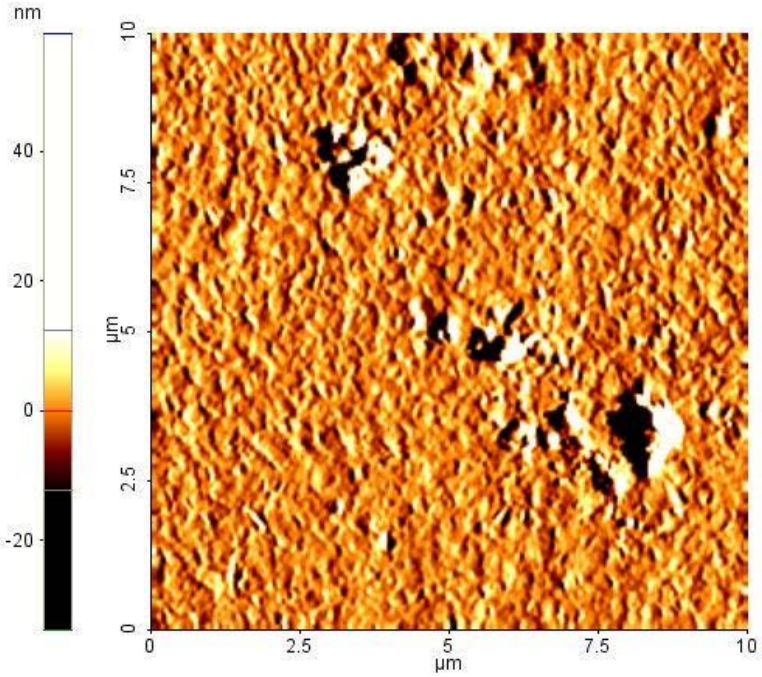

Figure 75: 10 µm Square AFM Scan of Film Doped Using 12 mg/mL solution and Method 2 for 3 minutes. Because the film was doped at equilibrium, the beginnings of crystallite formation can be seen. The texture of the surface is due to the formation of nucleation sites where the iodine deposits.

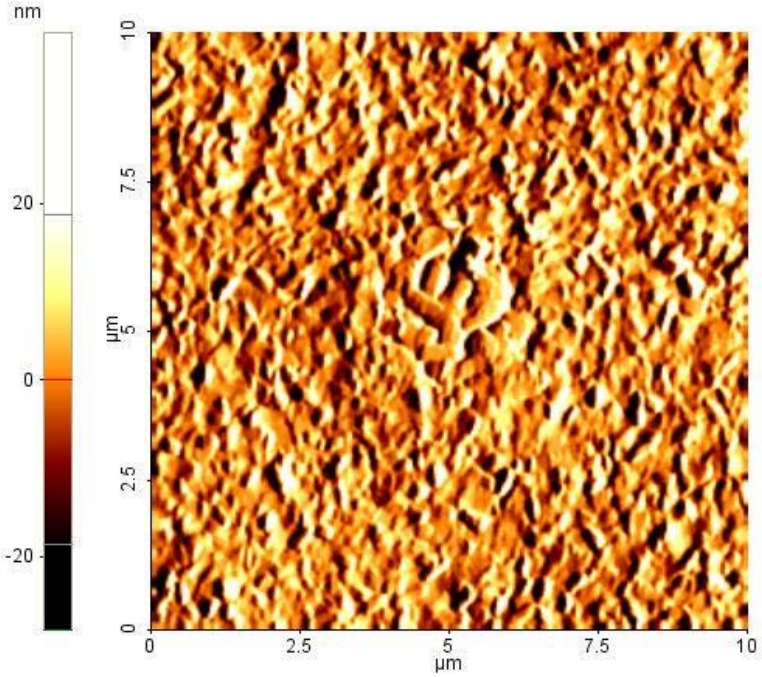

Figure 76: 10 µm Square AFM Scan of Film Doped Using 8 mg/mL solution and Method 2 for 4 minutes. Similar to Figure 75, the beginnings of crystallite formation are more defined than before.

Appendix C, continued

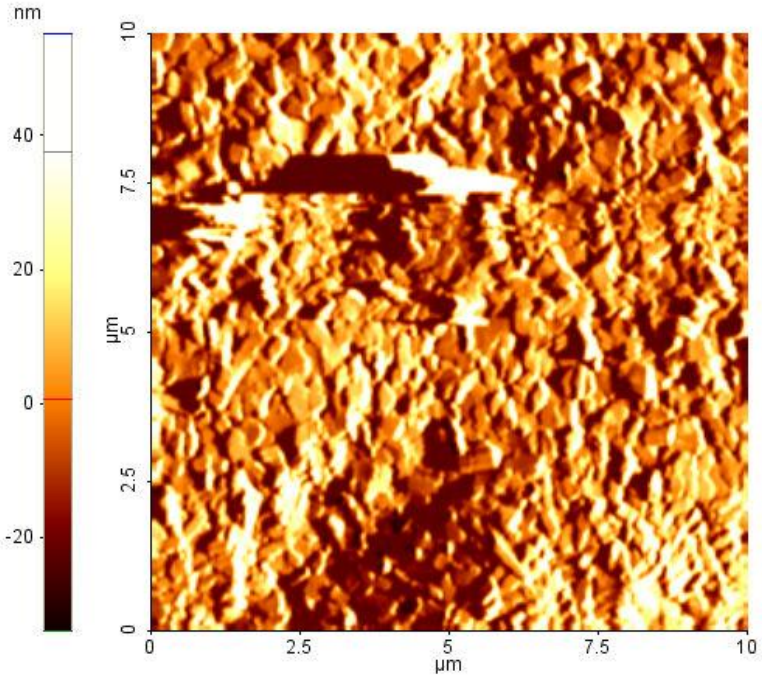

Figure 77: 10 µm Square AFM Scan of Film Doped Using 4.3 mg/mL solution and Method 2 for 10 minutes. Here, crystallite formation has occurred, and deposits with long range order are visible.

Appendix C, continued
5x5 µm surface scans:

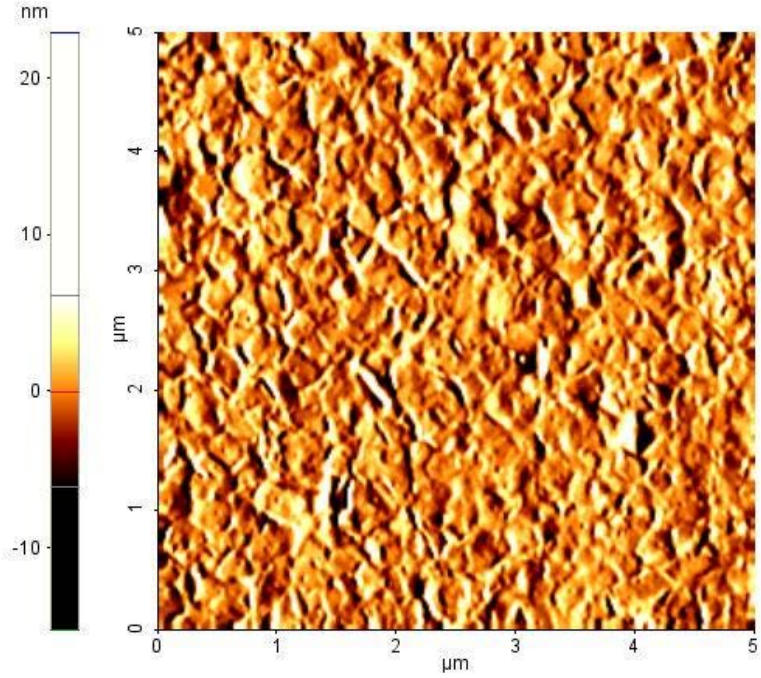

Figure 78: 5 µm Square AFM Scan of Film Doped Using 12 mg/mL solution and Method 2 for 3 minutes. This is a magnified area of the scan presented in Figure 75.

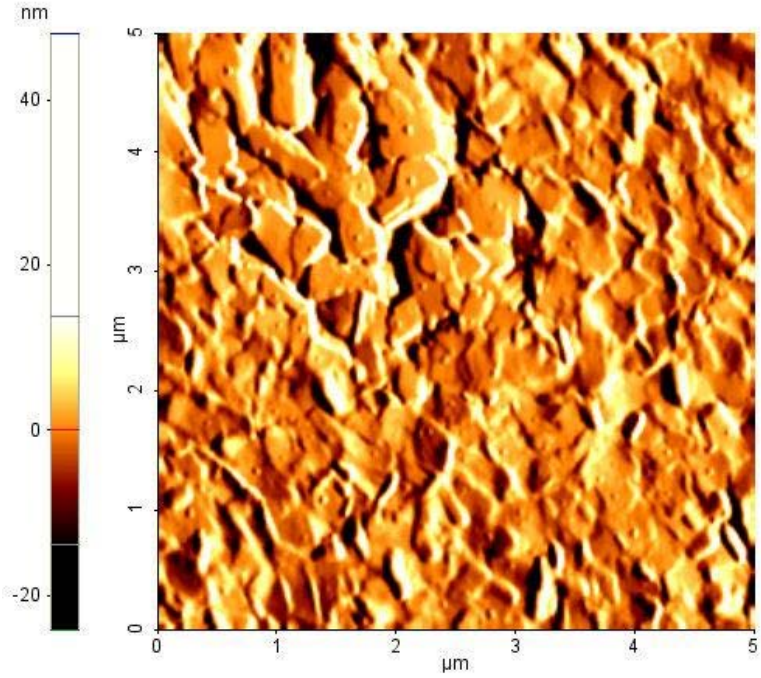

Figure 79: 5 µm Square AFM Scan of Film Doped Using 8 mg/mL solution and Method 2 for 4 minutes. This is a magnified area of the scan presented in Figure 76.

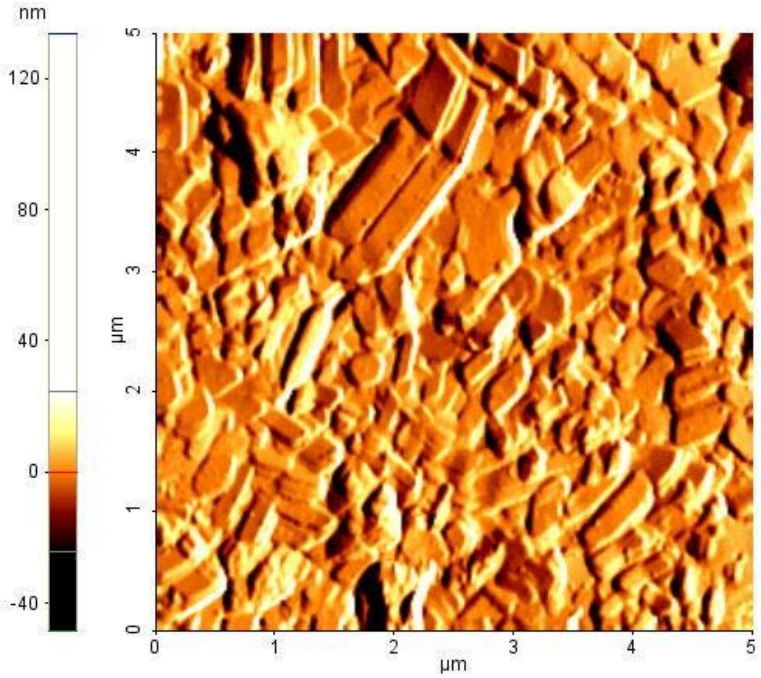

Figure 80: 5 µm Square AFM Scan of Film Doped Using 4.3 mg/mL solution and Method 2 for 10 minutes. This is a magnified area of the scan presented in Figure 77.

Appendix C, continued
2x2 µm surface scans:

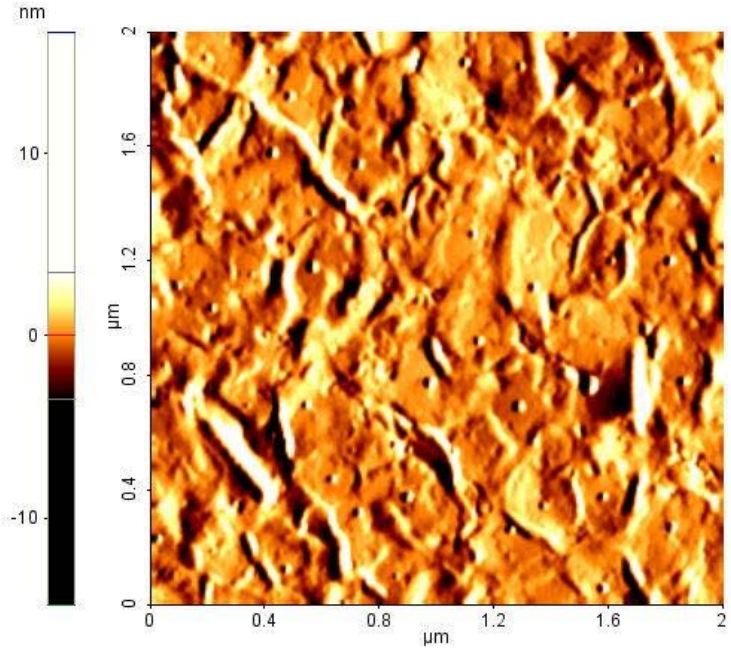

Figure 81: 2 µm Square AFM Scan of Film Doped Using 12 mg/mL solution and Method 2 for 3 minutes. This is a magnified area of the scan presented in Figure 78. At this magnification the details of the locations of the nucleation sites and the edges of the crystallites are more clearly defined.

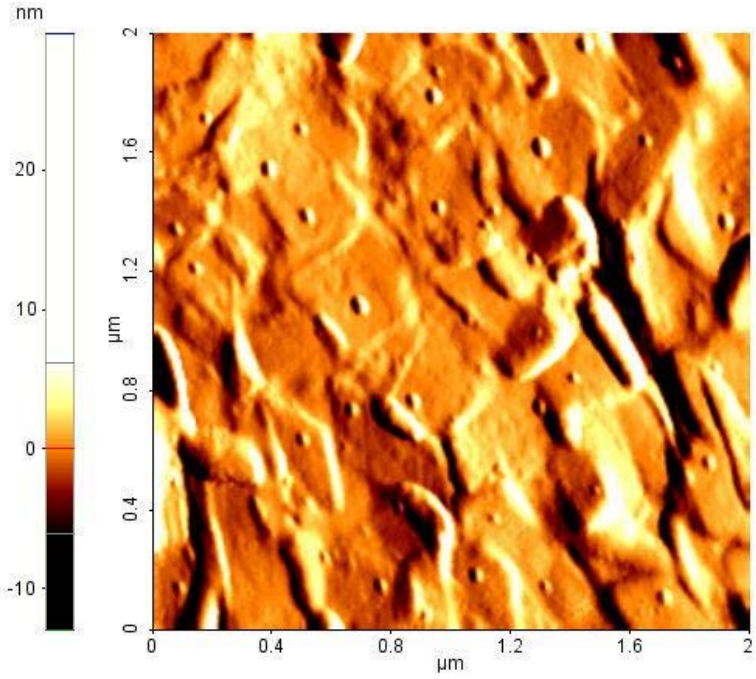

Figure 82: 2 µm Square AFM Scan of Film Doped Using 8 mg/mL solution and Method 2 for 4 minutes. This is a magnified area of the scan presented in Figure 79. The morphology of this concentration and exposure time can be seen to look very similar to that of the 12 mg/mL doped film seen in Figure 81, in such criteria as the size and density of the crystallites.

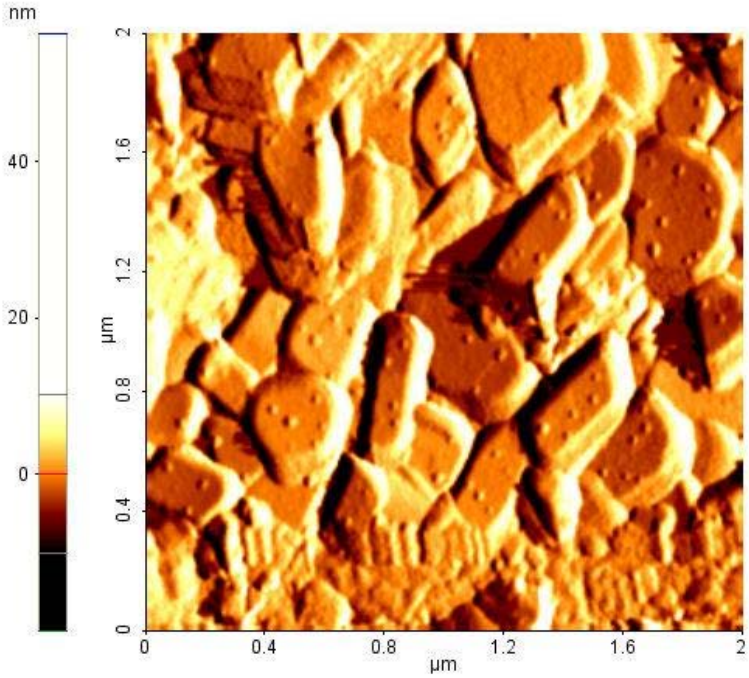

Figure 83: 2 µm Square AFM Scan of Film Doped Using 4.3 mg/mL solution and Method 2 for 10 minutes. This is a magnified area of the scan presented in Figure 80. In this scan it is clearly visible that the crystallites are now fully formed and that more nucleation sites are forming on their surface. The formation of these secondary nucleation sites seems to imply that the formation of a second layer of crystallites could potentially form on top of the first.

Appendix C, continued
0.5x0.5 µm surface scans:

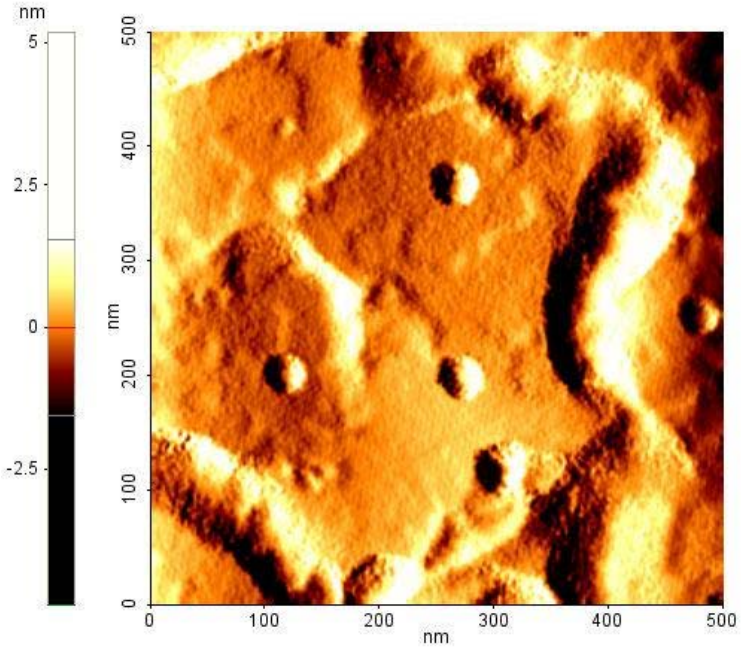

Figure 84: 0.5 µm Square AFM Scan of Film Doped Using 12 mg/mL solution and Method 2 for 3 minutes. This is a magnified area of the scan presented in Figure 81. This image is presented here for the purpose of emphasizing the formation of the iodine nucleation sites.

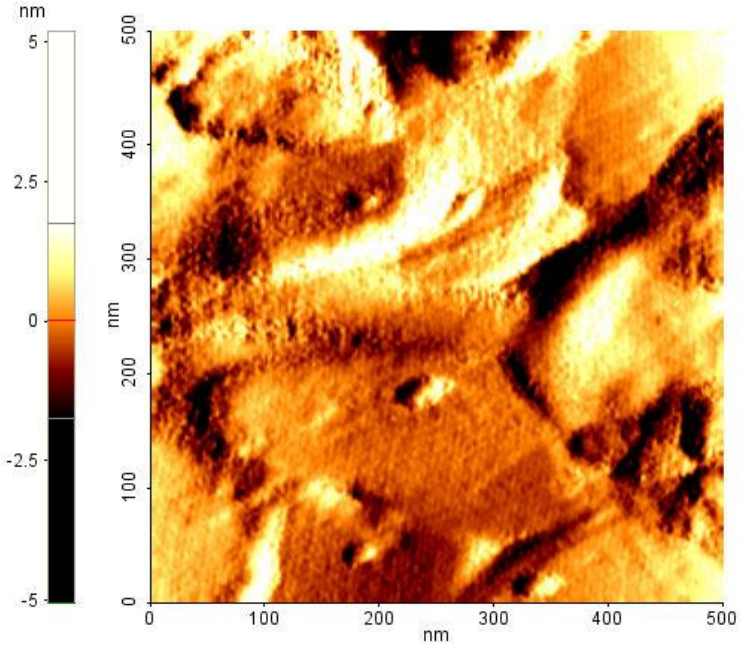

Figure 85: 0.5 µm Square AFM Scan of Film Doped Using 8 mg/mL solution and Method 2 for 4 minutes. This is a magnified area of the scan presented in Figure 82. The progression to more defined crystallites with iodine loading can be seen when comparing the image of this film to the 12 mg/mL doped film and the 4.3 mg/mL doped film.

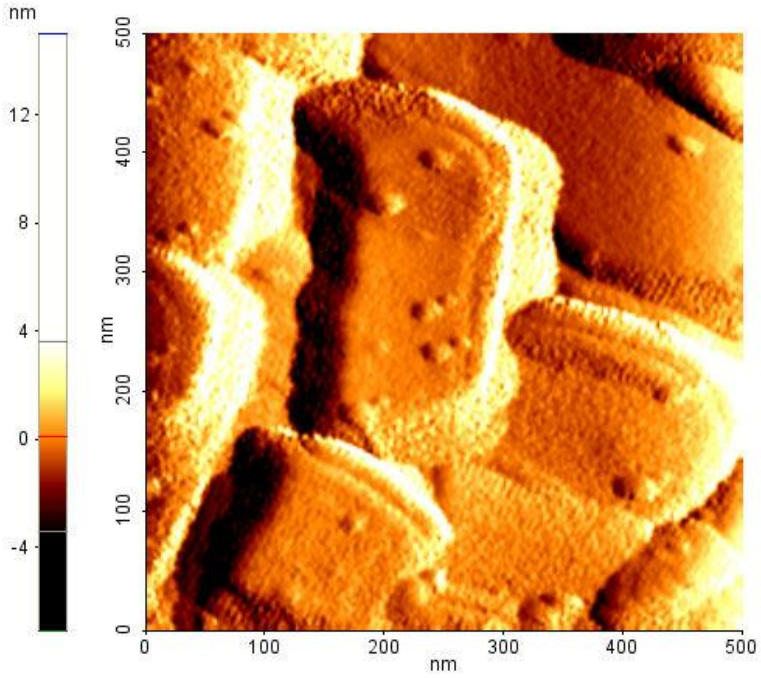

Figure 86: 0.5 µm Square AFM Scan of Film Doped Using 4.3 mg/mL solution and Method 2 for 10 minutes. This is a magnified area of the scan presented in Figure 83. Consistent with the other images taken of this film, the crystallites are more defined than in either of the other two films.

Appendix D: TEM Images

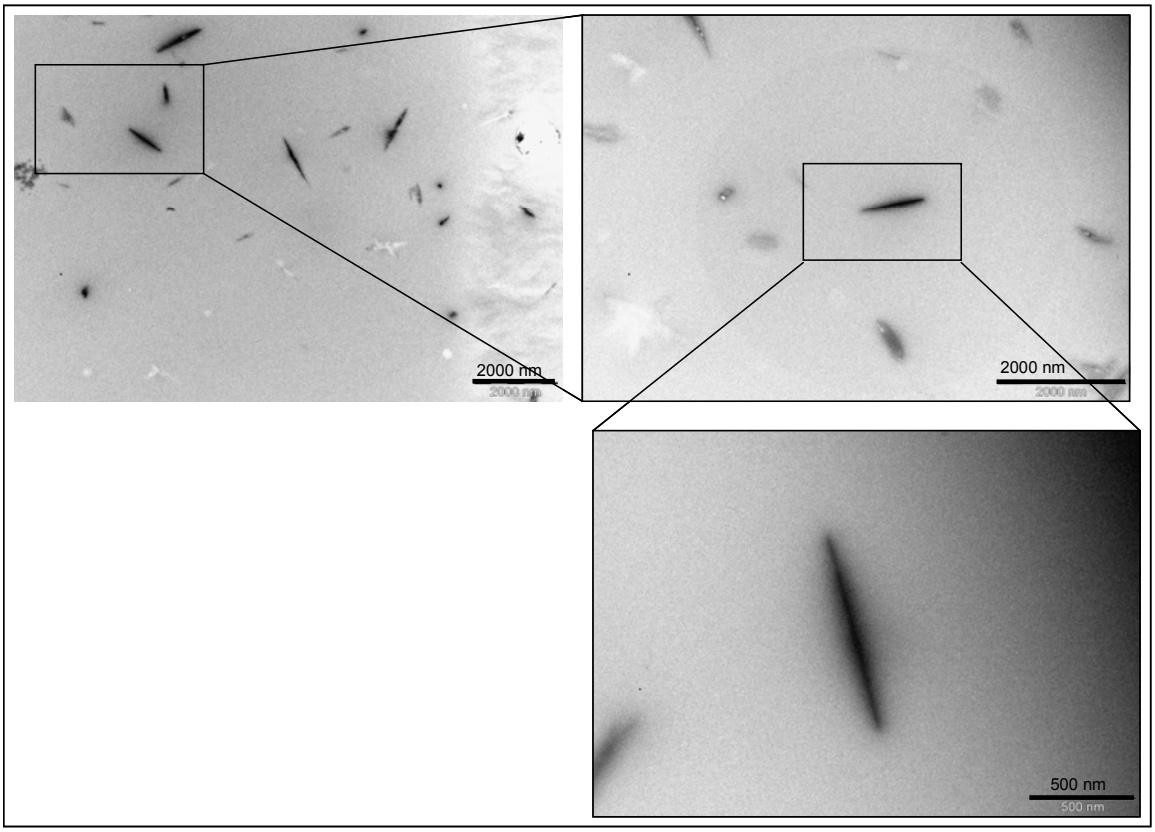

Figure 87: TEM – Iodine Deposit TEM Scans. Shown are three images - of successively higher magnification - of an iodine deposit on the 4.3 mg/mL film.